Title

Numerical Simulations in Support of a Long-Term Test of Gas Production from Hydrate Accumulations on the Alaska North Slope: Reservoir Response to Interruptions of Production (Shut-Ins)

Journal

Energy & Fuels, 36(7)

ISSN

0887-0624

Authors

Moridis, George J
Reagan, Matthew T
Liu, Yongzan

Publication Date

2022-04-07

DOI

10.1021/acs.energyfuels.1c04274

Peer reviewed

Numerical Simulations in Support of a Long-Term Test of Gas Production From Hydrate Accumulations on the Alaska North Slope: Reservoir Response to Interruptions of Production (Shut-Ins)

George J. Moridis*[1,2], Matthew T. Reagan[2], and Yongzan Liu[2]

1: Texas A&M University, Petroleum Engineering Dept., College Station, TX 77845
2: Lawrence Berkeley National Laboratory, Energy Geosciences Division, Berkeley, CA 94720
**Corresponding author: gjmoridis@lbl.gov*

Abstract

We investigate by means of numerical simulation a planned year-long field test of depressurization-induced production from a permafrost-associated hydrate reservoir on the Alaska North Slope at the site of the recently-drilled Hydrate-01 Stratigraphic Test Well. The main objective of this study is to assess quantitatively the impact of temporary interruptions (well shut-ins) on the expected fluid production performance from the B1 Sand of the stratigraphic Unit B during controlled depressurization over different time scales, as well as on other relevant aspects of the system response that have the potential to significantly affect the design of the field test.

We consider eight different cases of depressurization, including (a) rapid depressurization over a 60-day period to a terminal bottomhole pressure P_W of 2.8 MPa and (b) a slower depressurization rate to a final P_W of 0.6 MPa at the end of the year-long production test, in addition to (c) a multi-step depressurization regime and (d) a quasi-linear continuous depressurization strategy. The results of the study indicate that shut-ins obviously reduce gas release and production during and immediately after their occurrence, but their longer-term effects are strongly dependent on the depressurization regime and on the time of observation, covering the entire range of potential outcomes. Shut-ins (a) have a universally strong negative effect when quasi-linear depressurization is involved regardless of the length of the production period, (b) have a strong positive effect in multi-step depressurization schemes that becomes apparent earlier for large initial pressure drops, but (c) can also appear to have practically no effect for slow step-wise depressurization at the end of the year-long production test.

Shut-ins lead to a rapid reformation of hydrates, even to the point of disappearance of a free gas phase in the reservoir. Rapid depressurization regimes lead to early maximum rates of hydrate dissociation and gas production, while the maximum rates occur at the end of the production test for the cases of slower depressurization. Shut-ins do not appear to have a significant impact on water production, as the cessation of production is followed by higher rates production when depressurization resumes. Similarly, (a) the fraction of produced CH4 originating from exsolution from the water, (b) the water-to-gas ratio, and (c) the rate of replenishment of produced water by boundary inflows do not appear significantly affected by shut-ins, the effects of which seem to be temporary in the majority of the cases. The study confirmed the superiority of multi-step depressurization methods as the most effective strategies for hydrate dissociation and gas production, and showed that two observation wells (located at distances of 30 m and 50 m from the production well) are appropriately positioned and both able to capture the P, T and S_G behavior during the fluid production and shut-ins in any of the eight cases we investigated.

1. Introduction

1.1. Background information

Methane gas hydrate reservoirs occur in deposits beneath terrestrial permafrost and in sediments along the marine continental slope. These reservoirs may serve as a vast repository of

producible natural gas.[1] Gas hydrate is stable in the deep ocean and in permafrost environments, under the combination of high pressures and low temperatures. These hydrate reservoirs are producible as a resource if the solid hydrate phase can be destabilized, or dissociated, to generate free methane gas and liquid water. Production tests in permafrost reservoirs[2-4] and in oceanic reservoirs[5-6] have shown that producing gas from hydrates is feasible on short term scales, i.e. days or weeks. However, there is a pressing need for long-term tests to demonstrate that production from hydrates is commercially viable.

A review by Yamamoto et al.[7] summarizes the previous short-term field tests, and highlights the important lessons learned. The length of attempted production tests has increased over the past two decades, from a mere 5 days (the Mallik field tests of permafrost-associated reservoirs in 2002 and 2007)[8-9], to 37 days (the Ignik Sikumi test in 2012)[2], 42 days (the Nankai Trough offshore tests in 2017)[6], and then 60 days (the Shenhu test in 2017)[10], with produced volumes of gas increasing from less than 18,000 SCF to over 10 MM SCF. As the sophistication and scale of the field tests have evolved, so has our understanding of the techniques and technologies required for effective production. Hydrate dissociation by depressurization is understood to be the most effective method of production[11-12], and thus artificial lift systems tailored toward the thermodynamic conditions of a hydrate reservoir are necessary to maximize drawdown potential. However, the large pressure drop (several MPa) and the presence of unconsolidated or weakly consolidated sediments in hydrate reservoirs also necessitates devices to prevent sand intrusion. As only a limited number of short-term tests have yet been conducted, no specific sand control technology has been demonstrated as a best option for long-term, sustainable production from a hydrate reservoir. Finally, there are uncertainties surrounding the long-term response of hydrate reservoirs to production, and how ongoing changes in reservoir properties (geomechanical response, hydraulic containment of depressurization, evolution of reservoir permeability) will impact the performance of commercial-scale hydrate operations. This question has been explored extensively via numerical simulation[11, 13-15], but real-world experience is extremely limited.

The Yamamoto et al. review[7] demonstrates that long-term production testing—i.e., over a timescale comparable to a commercial operation—is essential to demonstrate the commercial feasibility and viability of production from gas hydrates. This is necessary not only to justify the investment in commercial scale development of hydrate resources, but also to refine the production techniques and technologies such that long-term operation of a hydrate reservoir results in stable, reliable, and economical gas production.

To address this issue, a long-term field test of hydrate production from a permafrost-associated reservoir on the Alaska North Slope has been pursued, with the recent drilling of the Hydrate-01 Stratigraphic Test Well confirming the occurrence of a suitable test site within the Prudhoe Bay Unit.[16] In preparation for this test, extensive geologic[17-19], engineering[20] and numerical simulation studies[21-22] are being undertaken in an effort to assess the system response under a wide range of circumstances, explore the technical challenges of long-term production from hydrate reservoirs and prepare an appropriate engineering design. This study is part a larger numerical simulation investigation seeking to provide answers and inputs to the design of the proposed production test in northern Alaska.

1.2. Objectives

The main objective of this numerical simulation study is to assess quantitatively the impact of temporary interruptions of production (well shut-ins) on the expected fluid production performance from a well-characterized gas hydrate reservoir during controlled depressurization

over different time scales, as well as on other relevant aspects of the system response that have the potential to significantly affect the design of the field test. Such interruptions in production are almost certain to occur, either because of required well-servicing operations or because of unintended disruptions caused by equipment failure, adverse weather conditions, or other issues. To that end, the effects of shut-ins are evaluated through comparisons to otherwise identical reference cases that involve no interruptions of production. We compare key performance metrics for various production scenarios and their evolution over the duration of the test: the rates of hydrate dissociation/formation in the reservoir, gas production from the gas and aqueous production streams, water production including inflows through the system boundaries, and the system response monitored at observation wells.

An additional objective of this study is to glean all possible additional information from the various cases that can be used to guide the decisions about production strategies and the associated operational parameters, and to improve the overall design not only of the long-term test, but also of possible future full-production of commercial-scale operations.

2. The Numerical Simulation and Problem Description

2.1. The hydrate simulator

In this study, we used the pT+H V1.5 code[23, 24], a recently-developed *parallel* implementation and extension of the serial TOUGH+HYDRATE V1.5 code (hereafter referred to as pT+H).[25, 26] The pT+H V1.5 code incorporates the most recent advances in computer languages, numerical solvers, physics, thermodynamics, and hydrate science.[27] In addition to its new capabilities, it can resolve all the problems that have been addressed in the past by the widely-used serial T+H simulator for the study of the system behavior in hydrate-bearing geologic media in settings that range from laboratory experiments to field studies covering all types of hydrate deposits, ***e.g.***, Class 1[28, 29], Class 2[30-32], Class 3[28] and Class 4.[33-35]

Thus, pT+H V1.5 is a hydrate-specific, parallel, fully implicit, fully compositional numerical model that describes the CH_4-hydrate behavior in geological media. In its current state, it accounts for all known flow, thermal, physical-chemical, and thermodynamic processes involved in the formation/dissociation of CH_4-hydrates, which can be described by either an equilibrium or a kinetic reaction. It can describe all methods of hydrate dissociation: depressurization, thermal stimulation, inhibitor effects, and combinations thereof. It solves the coupled equations of heat and mass balance for all components involved in a hydrate-bearing geologic system, ***i.e.***, H_2O, CH_4, inhibitor(s) and, in the case of a kinetic reaction, $CH4 \cdot N_H H_2O$ (hydrate, where N_H is the hydration number). These mass components are distributed among four possible phases (gas, aqueous, ice, and hydrate) in 14 out of the 15 possible states of phase existence and co-existence—a state of 100% hydrate saturation is not considered because of its physical improbability. Parallelization in pT+H V1.5 is implemented using (a) OpenMPI multi-threading, (b) the METIS[36, 37] domain decomposition package to partition the mesh and optimize load balancing among the various processors, and (c) the most recent version of PETSc[38], a fast, scalable, customizable toolkit for linear algebra in parallel scientific computing.

Note that the pT+H V1.5 simulator does not account for potential migration of the grains of the hydrate-bearing media toward the well, i.e., it assumes perfect sand control. Because preliminary scoping calculations using pT+H V1.5 fully coupled with the RGMS geomechanical simulator[23] did not indicate significant deformations during the duration of the production test, only pT+H V1.5 was used for the simulations discussed in this paper. However, changes in the porosity caused by changes in the pressure distribution and the hydrate saturation S_H were described using the

simplified geomechanical model based on the S_H-dependent pore compressibility model[26] available in pT+H V1.5.

2.2. Geology, geometry and configuration

A detailed description of the geology, stratigraphy, geometry, and the various units at the site is provided by Boswell et al.[16] and Tamaki et al.[19] and will not be repeated here. The schematic in **Figure 1** provides a simplified description of the simulated system, including the dimensions of its various geologic units. The testing configuration involves a single vertical production well, and two observation wells located at a distance of r = 30 m and 50 m from the production well.

In this study, we used a cylindrical domain because of the limited information on lateral heterogeneities present in the sediments, for computational simplicity, and because the use of a single vertical well for production precluded the use of Cartesian coordinates. The vertical dimension of the system was chosen as shown in **Figure 1** because early scoping simulations conducted by our team (and previous experience with systems of this size and scope[28-32,35]) indicated no possibility of mass and heat exchange between the simulation domain, the overburden (above the top of the hydrate-bearing Unit D) at z = -699.3 m, and the underburden below z = -947.5 m for production periods far exceeding the duration of the planned field test. The radial dimension was chosen in a similar manner after early computations indicated no fluid and heat exchange at a radius of r = 800 m from the single vertical well over a year of production (this boundary was also monitored during full production simulations). Thus, the simulated domain included the targeted production B1 Sand layer of Unit B (hereafter referred to as the HU-B layer), the additional hydrate-bearing C1 Sand and D1 Sand layers of Units C and D (hereafter referred to as the HU-C and HU-D layers, respectively), the hydrate-free, water-saturated interlayers named "BC" and "CD", and the underburden (see Figure 1). As will be discussed later, the fine discretization of the simulated domain allowed the use of the same grid without modifications in all the investigated cases, thus providing a stable reference for comparisons of the results.

2.3. System properties and well description

Substantial information on the hydraulic properties of the various units in the subsurface of the planned field test and their spatial variability with depth was obtained through the evaluation of logging-while drilling data acquired at the Hydrate-01 STW[17, 19] and pressurized side-wall core samples[39]. These data were the basis for the system properties used in our and all other numerical simulations.[22] Because of the very significant variability of the hydraulic properties with depth, and our effort to maintain maximum fidelity to the data in the vertical discretization of the simulation domain, the various properties in each vertical subdivision were obtained as:

$$\bar{X}_{\Delta z} = \left. \int_{Z_1}^{Z_2} X \, dz \right/ \Delta z, \quad \Delta z = Z_2 - Z_1 \qquad \text{.....(1)}$$

where $\bar{X}_{\Delta z}$ is the average value of the property X within the Δz subdivision between the Z_1 and Z_2 elevations, and is obtained from the numerical integration of all the raw data of X vs. z. The resulting vertical distributions of porosity ϕ, intrinsic permeability k (expressed as ln k, in which k is in mD) and irreducible water saturation S_{irA} in the discretized subsurface profile are shown in **Figure 2**, which depicts the significant vertical heterogeneity at the site. **Figure 3** shows the integrals resulting from Eq. 1 for all the key hydraulic properties in the all-important HU-B layer (the production target), and **Figure 4** shows the vertical distribution of the gas hydrate saturation S_H and of the exponent n of the equation used by pT+H V1.5 (see **Table 1**) for the prediction of

the relative permeability of the aqueous phase. The distributions of the exponent n in the HU-B and the other hydrate-bearing layers were obtained from the regressions shown in **Figure 5**, which are based on the relationships between the intrinsic and the effective permeabilities in these layers; the exponent m describing the relative permeability of the gas phase is estimated as

$$m = n - 0.5\ \mathrm{Max}\{0.0,\ n\text{-}2\}$$

Note that, to address the possibility of a gas phase appearing in the BC and CD interlayers and/or the underburden in the course of production, n values for these media were approximated using data and parameters from earlier studies of systems featuring similar reservoir properties[32, 40, 41] as references.

The relative permeability and the capillary pressure relationships, as well as the thermal properties of the various geological media in the layers of **Figure 1**, are listed in **Table 1**. In all simulations, an anisotropy ratio of $k_r/k_z = 2$ was used—note that early scoping simulations conducted by our team indicated that anisotropy has practically no effect on the fluid production predictions for a ratio as high as $k_r/k_z = 10$ over a year of operation. In the absence of capillary pressure data, the parameter values in the van Genuchten (1980) equation[42] were obtained from appropriate analogs in earlier studies[32, 41] having approximately the same intrinsic permeability k. The thermal conductivity values are consistent with those of media with the same type and texture. Reasonable specific heat values were used for all the geologic media[32, 41] because data from direct measurements were unavailable.

Based on earlier studies that validated this approach[28], we approximated wellbore flow with Darcian flow using a pseudo-porous medium with porosity $\phi = 1$, a very high $k = 5\text{x}10^{-9}$ m^2 (= 5,000 Darcies), a capillary pressure $P_c = 0$, a relative permeability that is a linear function of the phase saturations in the wellbore, and a low (but nonzero) irreducible gas saturation $S_{irG} = 0.005$ (necessary to allow the emergence of a free gas phase in the well). Note that the length of the completion interval of the well was not the same in all the simulated cases.

2.4. Domain discretization

The significant vertical heterogeneity in the domain (see **Figures 2** and **4**) necessitated the use of a very fine discretization, resulting in a very large number of elements and equations. The use of very fine grids is a consistent requirement for reliable results in hydrate simulations because of the very steep thermal and pressure gradients associated with the strong endothermic reaction of hydrate dissociation.[43] To avoid having to solve impractically large problems, we conducted a series of scoping calculations aimed at determining an appropriate discretization that would result in sufficient resolution and smooth gradients along the r- and z-coordinates. The scoping computations indicated that these desirable traits could be satisfied with (a) a uniform discretization of $\Delta z = 0.1$ m in the HU-B layer, (b) a uniform discretization of $\Delta z = 0.25$ m in the hydrate-bearing HU-C layer, (c) a uniform discretization of $\Delta z = 0.51$ m in the HU-D layer (distant from Unit B and unaffected by production from the HU-B layer), and (d) variable Δz ranging from 0.1 m to 5 m in the water-filled interlayers and in the underburden. The latter was possible because of the diffusive nature of the water flow equations in these formations, which allowed coarser discretization without loss of accuracy if appropriately fine grids were used near the boundaries of the hydrate-bearing units to allow proper capturing of the curvature of flow lines. The variability in Δz with depth is fully described in **Figure 2**.

Discretization in the radial direction was also very fine in the vicinity of the well, beginning with the well radius of 0.05 m, followed by Δr ranging between 0.1 and 0.3 for $r < 100$ m, and then logarithmically increasing to 6.2 m at the final $r = R = 800$ m. The domain discretization included (a) a top and a bottom constant-conditions (pressure P and temperature T) horizontal boundary layer, each with a $\Delta z = 0.01$ m, and (b) a $\Delta r = 0.01$ m constant-conditions radial boundary at $r = 800$ m in order to allow (if needed) mass and heat exchanges with the interior of the domain. Thus, the cylindrical domain was discretized into 627 x 343 = 215,061 gridblocks in (r,z) using the MeshMaker V2.0 package.[44, 45] Treating hydrate dissociation as an equilibrium reaction[46] and accounting for the effect of the (generally low, at 0.5%)[17-19] salinity on hydrate dissociation resulted in a system of about 860K equations, the number of which dictated the use of the parallel version of the code and the use of high-performance computing resources for the solution of the problem.

2.5. Initial and boundary conditions

The initialization process followed the methodology described by Moridis et al.[15, 43] The top boundary was maintained at a constant temperature $T_t = 4.68$ °C and a constant hydrostatic pressure P_t that corresponded to the elevation at $z = -699.3$ m. The temperature T_b and pressure P_b at the bottom boundary (at the base of the domain at $z = -947.5$ m) were also constant, and were determined from T_t and pressure P_t using a geothermal gradient of $dT/dz = 0.037$ °C/m determined from field data[17], and a hydrostatic water distribution for water with a salinity of $X_s = 0.005$ (mass fraction). The time-invariant boundary conditions at the outer radial boundary at $r = R = 800$ m were similarly determined. The thickness of the underburden, and the distance of the producing HU-B layer from the upper limit of the simulated domain had been determined to be sufficient to ensure that pressure and temperature changes caused by hydrate dissociation and gas production would not reach the system boundaries during the simulation period.

The initial P- and T-distributions within in the domain were determined from the conditions at the boundaries, and reflected hydrostatic conditions and the geothermal gradient at that site. In addition, the uppermost gridblock of the well was treated as an internal boundary condition, describing fluid production in response to a time-variable bottomhole pressure P_W .

2.6. Production scenarios and simulated cases

Predicted CH_4 production from the HU-B layer in the Hydrate-01 STW is based on depressurization-induced dissociation of hydrates. Our investigation covered several cases involving (a) different P_W regimes and (b) uninterrupted or interrupted operations, denoted respectively by the N and S moniker in their case names. Our studies involved the following cases:

- Case RN: This is the reference case, denoted by the "R" in its name. In this case, the length of the production (perforated) interval of the well is 10 m, and the top of the well is placed 3 m below the top of the HU-B layer. The advantages conferred by this location of the production interval include an expected reduction of the produced water because of the increased distance from the fully water-saturated BC interlayer and the overburden. The multi-stage (step-wise) depressurization process in Case RN, as described by the operational schedule of the P_W over time shown in **Figure 6**, was expected to cause a large initial (and rapidly decreasing) depressurization regime that would lead to large early gas production. Selection of this production regime as the reference case was based on the promising results of multi-stage depressurization reported in the laboratory experiments of Gao et al.[47], and on our preliminary

simulation studies on reservoir-scale production from hydrates in the course of this investigation. Note that the final P_W = 2.8 MPa is sufficiently high to prevent the formation of ice and its adverse effect on effective permeability.

- Case RS: This case differs from Case RN in that it involves two well shut-ins (**Figure 6**): the first lasts from t = 50 days until t = 70 days, and the second from t = 210 days to t = 220 days.
- Case LN: This case involves a well of the same length and position as those in Case RN, but the P_W declines linearly (hence the "L" in the case name) to a final level of P_W = 2.8 MPa, as described in **Figure 6**. The rationale for this P_W pattern is to mitigate the potentially negative geomechanical response and possible particle transport issues (i.e., significant sand production) that could be induced by the very large and sudden depressurization steps in the P_W regime of Case RS.
- Case LS: This case differs from Case LN in that it involves two well shut-ins (**Figure 6**) at the same times as in Case RS.
- Case 1N: This is a variant of Case RN, involving many small depressurization steps instead of the few large ones used in Case RN, and the P_W schedule is shown in **Figure 7**. The reason for this approach is, again, to minimize the possible negative geomechanical and particle transport consequences of rapid depressurization. In this case the length of the production (perforated) interval of the well is 7 m, and the top of the completion interval is placed 3 m below the top of the HU-B layer. Given the fact that the depressurization proceeds slowly and the perforated interval is shorter, the initial fluid production rates are expected to be significantly lower than those in case RN. Note that the final P_W = 0.68 MPa (100 psia) is well below the quadruple point of the CH_4-hydrate and is likely to lead to (a) high hydrate dissociation and CH_4 production rates and (b) ice formation in the reservoir.
- Case 1S: This case differs from Case 1N in that it involves two well shut-ins (**Figure 7**): the first lasts from t = 70 days until t = 100 days, and the second from t = 210 days to t = 220 days.
- Case 2N: This is variant of Case LN, involving the same well length and position as in case 1N, but with a depressurization schedule that leads to the final P_W = 0.68 MPa (100 psia) over a much longer period (**Figure 7**).
- Case 2S: This case differs from Case 2N in that it involves two well shut-ins (**Figure 6**) at the same times as in Case 1S.

3. Results and discussion

3.1. Cases RN and RS: Hydrate dissociation/reformation

Figures 8a and **8b** show the rate of hydrate dissociation/formation, Q_{DF}, in (a) Cases RN and RS and (b) LN and LS, respectively. Note that Q_{DF} is a cumulative rate that describes the behavior of the entire reservoir.

The effect of the sharp P_W drops at the two depressurization steps at t = 30 days and t = 60 days in Case RN (see **Figure 6**) is obvious in the initial "spikes" in Q_{DF} immediately after resumption of production, indicating rapid gas release, and in the substantially larger rates that follow. Both spikes in Q_{DF} reach very high levels, but last for a very short time: the first reaching Q_{DF} = 32,900 SCMD (1.16 MMSCFD) at t = 60.05 days, and the second one at reaching Q_{DF} = 37,300 SCMD (1.31 MMSCFD) at t = 60.05 days. The first spike is followed by a mildly increasing Q_{DF} on the order of 2,800 SCMD (100 MSCFD). The second spike (the second depressurization step to the final P_W) is followed by 5 distinct dissociation periods/steps: (a) an initial period of continuous mild Q_{DF} decline from about 22,600 SCMD (800 MSCFD) at t = 61.4 days to 10,170 SCMD (360 MSCFD) at about t = 185.1 days, (b) a period of faster decrease to 7,000 SCMD (250 MSCFD) at

t = 195.5 days, (c) a second period of mild decline to 5,800 SCMD (205 MSCFD) at t = 280 days, (d) a second period of rapid decrease to 3,900 SCMD (138 MSCFD) at about t = 315 days, and (e) a period of continuous Q_{DF} increase to 5,200 SCMD (183 MSCFD) until the end of the RN simulation at t = 428 days. (Note: this is beyond the duration of the planned test, but the simulation was allowed to continue to obtain a sense of the longer-term pattern of Q_{DF}).

Case RS shares the same Q_{DF} behavior until t = 50 days because of the common P_W evolution until that time. The first shut-in at that time leads to strongly negative Q_{DF}, indicating hydrate reformation in the reservoir and thus a reduction in free gas. This process is enhanced due to the substantial drop in temperature created by the endothermic dissociation of hydrate. As pressure recovers during shut-in, hydrate formation from the free gas and available water is enhanced by the lower temperatures in the reservoir. This reformation peaks at a rate of almost -11,300 SCMD (-400 MSCFD) at about t = 50.7 days, after which time the rate of hydrate formation in the reservoir declines rapidly and reaches zero at t = 55.6 days. The early and rapid hydrate reformation occurs in the immediate vicinity of the well, where the pressure increases rapidly while temperature increases only slightly. However, the pressure gradients at the beginning of shut-in persist in a large part of the reservoir, leading to continuous hydrate dissociation further away from the well that eventually balance hydrate formation at t = 55.6 days and then exceed it, leading to net hydrate dissociation past that point. However, as the pressure anomalies/changes in the reservoir become attenuated, P generally increases (as expected, given boundary conditions that simulate inflow from adjacent formations), leading to an almost zero Q_{DF} (93 SCMD = 3.3 MSCFD) at the end of the first shut-in. Q_{DF} is certain to reach zero if a longer shut-in is involved and a new equilibrium is reached in the reservoir.

What is particularly interesting is the Q_{DF} behavior in Case RS after the first shut-in, which begins before the second step of P_W reduction in Case RN and ends with a return to the final P_W level at 2.8 MPa. As a result, more hydrate in the vicinity of the well is now available for dissociation when production resumes, and this hydrate exists at a higher P. When production resumes, the initial pressure differential ΔP_W between the well and the HU-B layer is high, leading to the expected typical spike in Q_{DF}, but this occurs at a slight delay (at t = 71.46 days) and reaches a much lower level (18,600 SCMD = 656 MSCFD) than the second such spike for Case RN because the resumed ΔP_W is still lower than the P_W drop in Case RN. However, Q_{DF} in Case RS (a) decreases monotonically for t > 70 days until the onset of the 2nd shut-in at t = 210 days (at which time Q_{DF} = 10,260 SCMD = 363 MSCFD), and (b) is significantly and consistently higher than that for Case RN during this period.

It is also interesting to note that the cumulative volume that the first shut-in removes from dissociation in Case RS (= the volume between t = 50 days and t = 70 days in Case RN = 1.725x10^6 ST m^3) is surpassed by that corresponding to the excess in Q_{DF} in Case RS over that in Case RN from t = 70 days to t = 210 days. Coupled with the consistent higher Q_{DF} in Case RS, this provides an initial indication that the shut-in may have beneficial effects on hydrate dissociation when production is based on early, sharp step-wise declines in P_W. Possible reasons for this unexpected result are (a) that the interruption of production allows water to drain and the aqueous and gas phases to be more effectively separated (thus enhancing later dissociation), (b) the re-pressurization of the reservoir during shut-ins under the effect of the boundaries leads to larger ΔP_W and more efficient depressurization and hydrate dissociation when production resumes, and (c) and also because the shut-in may result in higher temperatures because of heat inflows from the surroundings and the release of heat caused by hydrate reformation (given the exothermic nature of the reaction).

The Q_{DF} of the hydrate reformation during the second shut in is much higher (in absolute value) than that in the first shut-in because this reaction is enhanced as P recovers from the much lower levels and over a larger part of the reservoir at the beginning of the shut-in. At the peak of hydrate formation at t = 214.6 days, Q_{DF} = -25,600 SCMD (-904 MCFD). Immediately after the bottomhole pressure P_W is restored in Case RS, Q_{DF} increases very rapidly from Q_{DF} = -22,830 SCMD (-806 MSCFD) at t = 210.01 days to 13,130 SCMD (= 464 MCFD) at t = 221.3 days, and then slower to reach Q_{DF} = 13,800 SCMD 487 MCFD) at t = 226.9 days, after which time it declines continuously and monotonically until it reaches a 6,780 SCMD (= 240 MCFD) at the end of the RS simulation at t = 327.7 days. Note that in these and all other cases discussed by this paper, the observations apply only to the periods covered by the simulations, and no extrapolation or speculation is possible past these points.

3.2. Cases LN and LS: Hydrate dissociation/reformation

The evolution of Q_{DF} in Cases LN and LS, which corresponds to the smooth, linear decline in P_W shown in **Figure 6**, is very different than that seen in Cases RN and RS. In Cases LN and LS, Q_{DF} is lower than in Cases RN and RS, as would be expected due to the much more rapid depressurization regime of the latter. In Case LN (**Figure 8b**), Q_{DF} increases monotonically until a single (global) maximum of Q_{DF} = 14,450 SCMD (510 MCFD) is reached at t = 180 days that coincides with the time when the final (lowest) P_W is attained at the well, beyond which time Q_{DF} declines continuously to reach 3,160 SCMD (112 MCFD) at the end of the simulation at t = 404.6 days. The decline after a maximum is reached is attributed to several factors: (a) P_W is no longer decreasing, thus maximum depressurization has been attained; (b) the pressure differential between the well and the hydrate-bearing HU-B layer that fuels hydrate dissociation begins to decrease as time advances past t = 180 days; and (c) the endothermic dissociation reaction has lowered T in the HU-B layer, causing further dissociation to decelerate.

The hydrate reformation that begins after the beginning of the first shut-in in Case LS exhibits the expected peak, which, however, occurs at a much lower rate of Q_{DF} = -8,330 SCMD (294 MCFD) than that in Case RS. This was expected, given the much lower pressure at which P_W operated at the time of the first shut-in in Case RS. The behavior of Q_{DF} in this case is consistent with expectations and similar to that in case RS: after the initial fast reformation, Q_{DF} slows down rapidly for reasons already explained, and it is then followed by a low-level net hydrate dissociation in the reservoir that tends rapidly to zero. What is particularly interesting is what happens after the end of the first shut-in: the typical Q_{DF} peak reaches only Q_{DF} = 3,970 SCMD (140 MCFD) and lasts only a short time (from t = 70.03 days to t = 77.3 days), beyond which it practically coincides with that of Case LN. In essence, the two different P_W regimes in Cases LN and LS appear to have practically no effect on the Q_{DF} performance for t > 77.3 days, and this is at first attributed to the slow, linear lowering of P_W that seems to have had a minimal impact on the main body of the hydrate until this point.

However, this is difficult to reconcile with the later evolution of Q_{DF} in Case LS. After practically coinciding with Case LN, Q_{DF} for Case LS begins to deviate slightly at about t = 126.7 days, and then exhibits oscillations and two local maxima at t = 161 days to t = 180 days, corresponding to Q_{DF} =11,400 SCMD (403 MCFD) and Q_{DF} =11,740 SCMD (416 MCFD), well below the maximum in Case LN. While the second local maximum (peak) can be explained as discussed in Case LN, the reasons for the first one are not obvious. The current hypothesis is that hydrate reformation following the first shut-in leads to localized high hydrate saturation regions

near the well that are more resistant to depressurization due to reduced effective permeability, hence the less effective dissociation.

The second shut in Case LS follows a pattern similar to that discussed in Case LN, defined by (a) a maximum hydrate reformation rate of Q_{DF} = -21,700 SCMD (-766 MCFD) at t = 213.4 days, (b) a short period of explosive increase in Q_{DF} from -17,000 SCMD (-600 MCFD) at t = 220.01 days to 13,500 SCMD (477 MCFD) at t = 221 days, (c) and a short period of modest increase in Q_{DF} to 13,750 SCMD (485 MCFD) at t = 225.8, after which (d) Q_{DF} declines continuously to reach 5,000 SCMD (177 MCFD) at t = 343.1 days, dipping well below the Q_{DF} level reached in Case LN at the same time. This is significantly different from the behavior of Q_{DF} in Cases RN and RS in **Figure 8a**.

Of particular interest is the hydrate behavior during production interruptions (or even cessation), as depicted in **Figure 9** that describes in detail the evolution of the rate of reformation (negative Q_{DF}) during the second shut-in in Cases RS and LS. It is obvious from **Figures 8** and **9** that the rate of hydrate reformation is very rapid, with CH_4 and water recombining to form new solid hydrate until one of the two (almost always the former) is exhausted. This has general implications for considerations related to long-term CH_4 production from hydrates, alleviating possible concerns that such production may lead to runaway reactions and uncontrollable releases of gas. In essence, hydrate systems appear to be self-limiting, responding very rapidly to the cessation of dissociation-inducing methods such as depressurization or thermal stimulation.

3.3. Cases RN, RS, LN, LS: Gas production rates at the well

Figures 10a and **10b** describe the gas production rates (and the source of the produced gas) in (a) Cases RN and RS and (b) LN and LS, respectively, in semi-log plots. **Figures 11a** and **11b** provide the same information on a linear scale for maximum clarity of the magnitudes of the various components of productions, which cannot be adequately captured by the logarithmic axes of the semi-log plots. These figures include the following variables: the total CH_4 production rate at the well Q_{PT}, the rate of CH_4 production originating from the gas phase Q_{PG}, the rate of CH_4 production obtained from its exsolution from the produced aqueous phase Q_{PA}, and, for reference, the corresponding rate of hydrate dissociation or formation Q_{DF}. Obviously, $Q_{PT} = Q_{PG} + Q_{PA}$.

Review of these figures, and a comparison to **Figure 8**, reveal the following:

- For t > 30 days (when the 2nd depressurization step occurs) and until the second shut-in, Q_{PT} and Q_{DF} follow the same patterns, running roughly parallel to each other in all cases (RN, RS, LN and LS). The reasons for the similarity in behavior have been discussed in Sections 3.1 and 3.2. Following the much larger Q_{DF} follow upon the onset of production after the second shut-in in Cases RS and LS, Q_{PT} and Q_{DF} tend to converge. This is particularly obvious in **Figure 11**.
- For t < 30 days (before the 2nd depressurization step) $Q_{PT} > Q_{DF}$ and even $Q_{PA} > Q_{DF}$ (for about 20 days), indicating that most of the produced gas originates from CH_4 exsolution from the produced water. This is because the initial depressurization step (**Figure 6**) is insufficient to cause significant hydrate dissociation.
- For t > 30 days, Q_{PT} is generally lower than Q_{DF}. This is a very desirable trait because the opposite would indicate a very large contribution from exsolved CH_4 in produced water, and this would be a very negative development given the very low solubility of CH_4: very large (and undesirable) volumes of water would be needed for a reasonable level of gas production. This is confirmed by the relative magnitudes of Q_{PT} and Q_{PA}, the latter being an order of magnitude (or more) smaller than the former after the initial stages of production,

indicating that the majority of the CH_4 produced at the well originates from the gas phase derived from depressurization-induced hydrate dissociation. Thus, the "spikes" of Q_{PT} are analogous to those in Q_{DF} and occur after the resumption of production, but often (as expected) with a delay from the times of the Q_{DF} occurrence. The first spike reaches a Q_{PT} level of 14,100 SCMD (500 MSCFD). After it settles down, the first spike is followed by a mildly increasing Q_{DF} on the order of 2,150 SCMD (76 MSCFD). The second depressurization step to the final P_W is followed by 4 distinct dissociation periods/steps identified in **Figure 10a**: (a) an initial period of continuous mild Q_{PT} decline from about 15,500 SCMD (547 MSCFD) at t = 61.4 days to 8,850 SCMD (313 MSCFD) at about t = 191 days, (b) a period of faster decrease to 6,900 SCMD (244 MSCFD) at t = 197 days, (c) a second period of mild decline to 4,550 SCMD (173 MSCFD) at t = 320 days, and (d) a period of Q_{PT} increase to 4,900 SCMD (173 MSCFD) until the end of the RN simulation at t = 428 days. The small difference Q_{DF} - Q_{PT} indicates that most of the gas released from dissociation is produced and that gas accumulation in the reservoir is expected to be slow and low.

- At later times, Q_{DF} dips below Q_{PT} in all cases, indicating that production at these times is supported by the free gas accumulated in the reservoir. This occurs later in Cases LN and LS (360 and 340 days, respectively) than in Cases RN and RS (280 days and 350 days respectively). This decline appears to be (a) permanent in the linearly-declining depressurization Cases LN and LS, but (b) only temporary in the multi-step depressurization Cases RN and RS, in which Q_{DF} appears to recover and to exceed Q_{PT} at later times. This is clearly shown in **Figure 11**.
- A confirmation of the dominant role of gas phase-originating CH_4 is provided by the proximity of the magnitudes of Q_{PT} and Q_{PG}, with $Q_{PT} > Q_{PG}$ and the former running parallel to the latter for the larger part of the duration of the simulated production test. The difference Q_{PT} - Q_{PG} = Q_{PA} is small.
- Q_{PT} in Cases RN and RS is consistently larger than that in Cases LN and LS, respectively. This indicates the superiority of the multi-stage (step-wise) depressurization regime over that of a continuous P_W decrease as a hydrate dissociation strategy.
- A major issue emerging from the analysis of these figures is that (a) the shut-ins appear to have a positive effect on Q_{PT} in Case RS, leading to consistently higher production rates after every shut-in than those in the uninterrupted Case RN. Conversely, the interruption of production in Case LS leads to production rates that are (a) consistently lower than those in the uninterrupted Case LN after the first shut-in, and, (b) generally lower after the second shut-in, although there is an interval in which they are higher.

The contribution of CH_4 from the gas phase (released by hydrate dissociation) is evident in **Figure 12**, which shows the ratio of CH_4 produced in the gas phase to the total CH_4 production, $R_{GT} = Q_{PG}/Q_{PT}$. R_{GT} rises very rapidly in Cases RN and RS, reaching and exceeding the 80% level after the 2nd depressurization step at t = 30 days, and exceeding the 90% level after the 3rd depressurization step, as dictated by the operational schedule of **Figure 6**. The well shut-ins appear to have a very minor effect on the R_{GT} evolution in both these cases, which have similar performance. In Cases LN and LS, it takes much longer for R_{GT} to reach the 80% and 90% levels (about 70 and 90 days, respectively), and this is consistent with the lower gas release rates associated with the mild depressurization regimes in these cases. Note (a) the clear downward trend in R_{GT} in Cases LN and LS for $t > 340$ days, which is an indication of increased contribution of Q_{PA} to production Q_{PT}, possibly because of water influx from the boundaries (b) the practically

stable R_{GT} levels in Cases RN and RS at the same time. This appears to be another indication of the superiority of multi-depressurization schemes in gas production from CH_4 hydrates.

3.4. Cases RN, RS, LN, LS: Cumulative volumes of released, produced and free gas

Figures 13a and **13b** describe the cumulative volumes of the gas released from dissociation, V_{DF}, and produced gas, V_{PT}, in (a) Cases RN and RS and (b) LN and LS, respectively. The advantage of the analysis of these variables is that V_{DF} and V_{PT} are free from the significant short-term variability of the related rates (Q_{DF} and Q_{PT}, respectively), and allows reaching conclusions that cover any subset of the expected duration of the production test.

Review of these figures reveals the following:

- V_{PT} and V_{DF} follow the same general patterns in the uninterrupted production Cases RN and LN. The V_{PT} and V_{DF} patterns are different in the RS and LS cases because of (a) the well shut-ins, reflected in the constant V_{PT} levels ($Q_{PT} = 0$) during them, and (b) hydrate reformation during shut-ins, leading to a temporary decline in V_{DF}.
- With the exception of early times ($t < 50$ days), V_{PT} is consistently lower than V_{DF} in all cases, as expected from the similar relationship between Q_{PT} and Q_{DF}. This confirms that the HU-B layer is a promising target when production follows the schedule of any of the Cases RN, RS, LN, and LS because the produced CH_4 is not expected to be dominated by exsolved gas from produced water.
- For reasons expected from the evolution of the relative magnitudes of Q_{DF} and Q_{PT} (**Figures 10** and **11**), and for reasons already explained, CH_4 release and production in Cases RN and RS are consistently higher than in Cases LN and LS, indicating the superiority of multi-step depressurization as a hydrate depressurization strategy.
- The V_{PT} and V_{DF} results confirm the earlier observation that the shut-ins appear to have a positive effect on production in Case RS. The dV_{DF}/dt and dV_{PT}/dt slopes are steeper in Case RS, with the associated V_{PT} and V_{DF} curves intersecting and exceeding in the long run (for $t > 300$ days) those from the uninterrupted Case RN, indicating greater CH_4 release and production. The reason for the improved performance after shut-ins can be attributed to several factors: drainage of the earlier-released water toward the base of the reservoir and improved separation of the aqueous and gas phases; a higher ΔP_W pressure differential because of the recovery of pressure in the reservoir; higher temperatures in the reservoir because of (a) warmer water inflow from the outer boundaries of the system toward the well, (b) conduction-induced heat flows and (c) heat release following the exothermic reactions of hydrate reformation. All of those, separately or in combination, have the potential to enhance dissociation upon resumption of production after shut-ins.
- Conversely, the V_{PT} and V_{DF} results confirm the earlier observation that the shut-ins appear to adversely affect CH_4 release and production in Case LS. As **Figure 13b** clearly indicates, V_{PT} and V_{DF} in Case LS never fully recover after the shut-ins, and their curves run parallel to (and substantially lower than) those corresponding to Case LN. Their parallel trajectory indicates that, following the shut-ins, in Case LS there is a persisting deficit in both CH_4 release and production that cannot be overcome during the expected length of the field test.

The advantage conferred to Case RS by the well shut-ins, and its successful recovery following the resumption of production is also evident in the evolution of the amount of the free gas V_F in the reservoir over time (**Figure 14**). The significant reduction in (and even disappearance of) the free gas caused by the hydrate reformation during the shut-ins is rapidly overcome in Case RS, with V_F rapidly converging toward that from the uninterrupted Case RN after each shut-in, and

exceeding it after about t = 275 days. On the other hand, after some initial convergence early after the shut-ins, the evolution of V_F in Case LS shows divergence from that of Case LN, and the two end up having have roughly parallel trajectories with substantial separation between them.

3.5. Cases RN, RS, LN, LS: Water production rates

Figures 15a and **15b** show the evolution over time of the mass flow rates of water (a) produced at the well Q_{wW} and (b) inflows from the top and bottom boundaries of the HU-B layer, Q_{wT} and Q_{wB}, in Cases RN and RS, respectively. Additionally, the cumulative water inflow $Q_{wA} = Q_{wT} + Q_{wB}$ from the boundaries into the HU-B layer is included in the figures. **Figures 16a** and **16b** show the same information for Cases LN and LS, respectively. Note that the simulation results in all these cases indicated no water and/or heat exchanges between the interior of the domain and its top horizontal, bottom horizontal and outer radial boundary at r = 800 m, nor between the HU-C and HU-D layers their adjacent units/boundaries.

Review of these figures reveals the following:

- The water production rate at the well Q_{wW} (a) increases consistently as time advances for the entire duration of the study (t = 380 days) in the multi-step depressurization Cases RN and RS, and (b) increases until t = 340 days in the quasi-linear depressurization Cases LN and LS, after which time it begins to decrease (as Q_{wT}, Q_{wB}, and Q_{wA} also do).
- While shut-ins (Cases RS and LS) lead to spikes after the resumption of production (for reasons already explained), these do not last long. In all cases, the maximum Q_{wW} values are in the 2,500 BPD range (reaching 3,000 BPD in the spikes at the resumption of production after shut-ins) do not appear excessive. In general, and spikes notwithstanding, the Q_{wW} levels do not differ substantially in all four cases show in in **Figure 15**.
- Water inflows from the boundaries are significant, with contribution of the bottom boundary $Q_{wB} > Q_{wT}$ because of (a) higher k and (b) lower S_H near the base of the HU-B layer, resulting in a higher overall effective permeability (see Figures 4 and 6).
- Q_{wA} represents a large fraction of Q_{wW}, indicating replenishment of produced water (originating from native water and water released from hydrate dissociation) by water inflows from the top and bottom boundaries. This is not a positive development because it reduces the effectiveness of depressurization and adversely affects the water disposal activities. Note that the long-term trend in Cases LN and LS appears to indicate parity of the produced and replenished water rates (and even $Q_{wW} < Q_{wA}$), which could further aggravate the effectiveness of depressurization and hydrate dissociation. Such parity is also observed in cases RN and RS, but it is only temporary and the $Q_{wW} > Q_{wA}$ relationship is quickly restored (providing another piece of evidence in support of the superiority of the multi-depressurization schemes).
- Spikes excluded, as expected from the associated Q_{PT} behavior, the shut-ins lead to long-term trends of (a) an increase in Q_{wW} in Case RS over that in Case RN and (b) a lower Q_{wW} in Case LS than that in Case LN.
- In general, shut-ins do not appear to significantly affect water production, as the interruption of production is followed by higher initial Q_{wW} and spikes when production resumes.

3.6. Cases RN, RS, LN, LS: Water-related parameters

As indicated by Moridis et al.[11], production of CH_4 from hydrates from any given accumulation is evaluated using two criteria: (a) the absolute criterion, involving Q_{PT} and describing the overall CH_4 production potential and (b) the relative criterion, describing the water-to-gas ratio R_{WG} =

Q_{wW}/Q_{PT} that describes the amount of (unwanted) water associated with the CH_4 production. Obviously, a promising production target is associated with the maximization of the absolute criterion and the minimization of the relative criterion. In a completely isolated system (i.e., bounded by impermeable boundaries), the long-term value trends asymptotically toward 4.[28]

Figure 17 shows the evolution of R_{WG} of the relative criterion in all the cases. While R_{WG} initially declines from a very high initial level of over 225 (when water is the only produced fluid and the only CH_4 is that obtained from exsolution, see **Figure 12**) to as low as 15 (Cases RN and RS) or 30 (Cases LN and LS), the long-term trend of R_{WG} is increasing, indicating increasing contribution of water inflows from the boundaries. This is consistent with the similar earlier observations from **Figures 12**, **15** and **16**. Of interest are (a) the practically stable R_{WG} in Case RN for $t > 330$ days > and (b) the rapid increase of R_{WG} for $t > 280$ in Case LS, which strengthens its ranking as the worst performer among the four cases, as evidenced from the results shown in **Figures 10** to **14**. Note that the effect of shut-ins on the magnitude of R_{WG} and its evolution over time do not appear important in the production test targeting the HU-B layer.

The significant water inflow from the boundaries is also further confirmed by the replenishment ratio of water, defined by $R_{BW} = Q_{wA}/Q_{wW}$ and described for all cases in **Figure 18**. As explained earlier, a high R_{BW} indicates ineffective depressurization and, consequently, dissociation. This figure shows that R_{BW} in all cases reaches and exceeds the 80% level very early in the production process (i.e., in 30 days or less). The well shut-ins in Cases RS and LS reduce R_{BW}, but only temporarily and for very short periods immediately after the resumption of production. What is cause of concern is that the long-term trend of R_{BW} exceeds 90% in all cases, and can reach 1 (Cases RN, LS), or even exceed it (Cases LN and LS, possibly consistently). This is in agreement with the observations from **Figure 17**. Such a scenario can be (possibly) explained by the partial dissociation of a local body of hydrate that continues to act as a barrier to water inflow near a boundary (hence the lower late-time Q_{wW} in **Figure 16**). Such a localized dissociation could explain the significant Q_{PT} in this case at that time (**Figure 10**). In general, as **Figure 18b** indicates, shut-ins appear to be associated with somewhat higher, but not significantly different, terminal (late-time) R_{BW} levels in the HU-B production test.

3.7. Cases RN, RS, LN, LS: Response in the observation wells

The importance of the observation wells cannot be overemphasized, as they represent the main instruments that allow direct observations and measurements of hydrate dissociation and behavior over the duration of the production test. Thus, it is important that the two observation wells at the site of the field test—at distances of $r = 30$ m and $r = 50$ m from the production well, and referred to as the O30 and O50 well, respectively—be appropriately located to monitor the relevant reservoir properties and their changes during the production operations.

Figures 19, **20** and **21** show the evolution of P, T, and of the pore-volume averaged gas saturation S_G in the two observation wells in all cases. The evolution of P in **Figure 19** captures all the changes in the P_W regimes in the various cases, allowing clear identification of all times when the P_W changes. Thus, the various depressurization stages in Case RN, the slow linear P_W decline in Case LN, and the shut-ins in Cases RS and LS are identified by unmistakable inflection points at the known times of change. Because of the low compressibility of water, the pressure wave travels very fast in fully-saturated media, and changes in P_W are sensed simultaneously in both wells at all times and in all cases, despite the difference of 20 m in their distance from the well. This indicates their suitability as pressure observation wells in all cases. However, while pressure monitoring in these wells is necessary, it is by no means sufficient in the understanding

and analysis of gas production from hydrate deposits. Increasing P at later times after the final minimum P_W is reached (beginning as early as at t = 275 days—Case RN—and continuing afterwards) is probably associated with the water inflows that have been previously indicated by other variables. The O30 well is an exception, as its P evolution (continuous decline in Case LN and stability in Case LS) suggests (a) continuing or balanced dissociation and (b) a localized response that is in contrast with that monitored in the O50 well. In general, shut-ins are shown to result in late-time P_W levels that are (a) lower in the multi-stage depressurization Case RS than those in the uninterrupted Case RN and (b) higher in Case LS than that in the uninterrupted Case LN.

Temperature is expected to be a much better indication of hydrate behavior than pressure because of the large enthalpy of the hydration/dissociation reaction. Thus, hydrate dissociation is generally expected to be (a) indicated by the lowering of T (the reverse is expected in the hydrate formation) and (b) be delayed relative to the P-response because the dissociation front moves slower than the pressure front in hydrate-bearing media. Additionally, there is field evidence that the temperature front does not arrive at the same time along the length of the observation well, but can appear locally and unexpectedly at different levels within the wells dependent on geologic conditions and the heterogeneity in S_H, which can lead to dendritic patterns ('fingering') of the dissociation front.[7] Of course, the T-profile can be affected by other factors, such as water flows through the observation wells that can confuse observations.

Figure 20a indicates a sharp decrease in T at the r = 30 m well and a slight one at the r = 50 m well as early as t = 0 days in Cases RN and RS, i.e., at the time of the first depressurization step. Much stronger decreases are observed in both wells at t = 30 days and 60 days, i.e., at the time of the second and third (and final) depressurization step in this case. These responses provide strong (but indirect) indication of dissociation. Similarly, there is significant warming at the O30 and the O50 well in Case RS at t = 50 days and at t = 210 days, directly associated with hydrate reformation after the well shut-ins and further indicating that the well locations are appropriate for observing the hydrate behavior in the reservoir. The T-response in **Figure 20b** provides additional confirmation of the suitability of the observation wells, as it captures the T-increase associated with hydrate formation caused by the well shut-ins at t = 50 days and at t = 210 days in Case LS, as these deviate from Case LN. As in the case of the P results in **Figure 19**, increasing T at later times appear to an indication of the already-discussed water inflows from the boundaries (especially from the warmer lower border of the HU-B layer) after the final minimum P_W is attained. The observations at the O30 well in Cases LS and LR are exceptions, in which the evolution of T indicates cooling (indirect evidence of continuous dissociation) and a localized response that is markedly different from that at the O50 well in the same cases.

Observation of free gas in the simulated observation wells is the only possible direct indicator of hydrate dissociation because a free gas zone does not exist in the HU-B layer at the beginning of the simulation. The results in **Figure 21** fully confirm the suitability of the two observation wells. Thus, gas in measurable quantities evolves at the O30 and the O50 wells at t = 35 and 50 days, respectively, in Case RN. The same evolution happens at t = 50 days and t = 80 days in Case LN because of the much slower rate of depressurization at the production well. In Case RS , the well shut-ins are clearly denoted by (a) the disappearance of the free gas because of hydrate reformation at t = 52 days in the O30 well, (b) its reappearance at about t = 70.2 days (slightly after the resumption of production) and (c) the almost simultaneous and reappearance of gas at t = 220 days. This coincides roughly with the end of the second shut-in and is almost identical in behavior with that of the O50 well at the same time. Similar observations can be made for both

wells in Case LS. Long-term declines in S_G are attributed to water inflows from the boundaries and the reduction of the related Q_{DF} and Q_{PT} rates discussed previously. The O30 well exhibits in Cases LN and LS an aberrant behavior that is similar to that identified in **Figures 17, 19** and **20**, involves continuously increasing S_G for $t > 280$ and 320 days, respectively, and constitutes direct evidence of continuing hydrate dissociation that is localized in nature and very different from the observations at the O50 well. A possible explanation for such behavior would be the dissociation of a body of hydrate at this location, and this would be consistent with the increase in R_{WG} at the same time that was discussed earlier (see Section 3.6 and **Figure 17**).

Thus, the observation wells are appropriately positioned and both should be able to capture the *P, T* and S_G behavior during the gas production from the HU-B layer in any of the four cases investigated up to this point. Note that Case LN (and, to a lesser extent, Case LS) exhibits late-time "aberrant" behavior that significantly deviates from that in the other cases. We speculate (but we have no way of proving) that this is attributed to partial dissociation of localized hydrate formation that restricts water flows without inhibiting gas flow, thus leading to enhanced localized dissociation and gas release, with correspondingly lower *P* and *T*.

3.8. Spatial distributions of key flow and thermodynamic variables

The evolution of the spatial distributions of *P*, *T*, S_H and S_G in Case RN are shown in **Figures 22**, **23**, **24** and **25**, respectively. Because of the diffusive nature and the high velocity of the pressure wave, the pressure disturbance caused by the variation in the P_W extends to a radial distance of about 400 m of the $r = 800$ m domain, and well beyond the vertical boundaries of the HU-B layer. As depressurization continues, the footprint of measurable *P* changes continues to expand.

The temperature disturbance in **Figure 23** is fully contained within the HU-B layer, prevented from expanding beyond its boundaries because of the location of the well below the top of the hydrate zone, and because of the inflow of water from the top and bottom boundaries (the BC interlayer and the underburden). The footprint of the spatial distribution of *T* expands with time as hydrate dissociates and the affected region becomes cooler, reaching a maximum distance of about 120 m from the well at $t = 365$ days. This region of significant cooling is what drives the hydrate reformation process discussed in Sections 3.1, 3.2, and 3.9, during shut-in and reservoir repressurization. The S_H distribution in **Figure 24** demonstrates the significant vertical heterogeneity of the HU-B layer, shows maximum dissociation near the well (as expected), and the pattern of the dissociated region is in rough agreement with the *T*-distribution. Note because of the high initial S_H and the significant variability, subtle changes are not easily discernible in **Figure 24**. The obvious conclusion from the inspection of the limited radius in this figure and the limited extent of the dissociated hydrate (indicated by $S_H = 0$) is that only a minuscule fraction of the original hydrate in place in the simulated domain of the HU-B layer is affected by depressurization during the test period. Finally, the spatial distribution of S_G in **Figure 25** shows significant heterogeneity (an inevitable natural consequence of the heterogeneous S_H distribution) and continuous expansion of its footprint over time, reaching a maximum distance of about 170 m from the well at $t = 365$ days. As expected, the highest S_G concentrations occur in the vicinity of the well and near its top, as dictated by the gas buoyancy and the high intensity of the dissociation at these locations.

A comparison of the S_G saturation distributions between Cases RN and RS at $t = 90$ and $t = 270$ in **Figure 26** shows the effects of the two shut-ins even at relative long times after their ends. Thus, the extent of the occurrence of $S_G > 0$ is more extensive in all the RN cases at the same times. The

additional S_G distribution at t = 220 days shows the partial disappearance of the gas, caused by hydrate reformation, at the time of the end of the second shut-in.

3.9. Cases 1N, 1S, 2N, 2S: Hydrate dissociation/reformation

Because of the extensive discussion of the results in Cases RN, RS, LN and LS, the following analyses 1N, 1S, 2N and 2S will be more concise, as there is no need to repeat the underlying reasons for similar system behavior. **Figures 27** and **28** show the rate of hydrate dissociation/formation Q_{DF} in (a) Cases 1N and 1S and (b) 2N and 2S, respectively. Note that Q_{DF} is a composite rate that describes the cumulative behavior of the entire reservoir.

The effect of the multiple P_W depressurization steps is obvious in the pattern of the evolution of Q_{DF} in Case 1N (see **Figure 27a**), which is characterized by multiple spikes, each coinciding with the corresponding pressure drop (**Figure 7**). For maximum clarity of the attained Q_{DF} levels at all scales, both the semi-log and the linear plots are included in **Figure 27**. The main observations to be gleaned from inspection of this figure are the following:

- With the exception of the period after the second shut-in, the Q_{DF} levels in Case 1S are generally lower than, but close to, those in Case 1N, although they all tend to converge.
- The hydrate reformation rates are also very high (reaching a maximum of about -13,000 SCMD = -460 MSCFD) during the second shut-in of Case 1S.
- Unlike the RN and RS cases, in which a maximum Q_{DF} is reached on the middle of the production test, Q_{DF} continues to increase for much longer, reaching maxima of 36,400 and 33,300 SCMD (1.285 and 1.176 MMSCFD, respectively) in Cases 1N and 1S, both at the same time t = 350 days. As in all previous cases, the decline in Q_{DF} after a maximum is attained is attributed to a combination of (a) the attenuation of the depressurization effect over an ever-increasing reservoir radius and (b) the cooling of the reservoir caused by the continuing hydrate dissociation.
- Beginning at about t = 300 days, Q_{DF} in Case 1S is consistently higher than that in Case 1S, with the two curves running roughly parallel to each other. This provides an early indication of the beneficial effects of shut-ins for the reasons already discussed, and is in agreement with the similar observations from Cases RN and RS.
- Of interest is the coincidence of the times when the Q_{DF} maxima are observed in Cases 1N and 1S, which indicates that the conditions that lead to the subsequent decline in Q_{DF} occur at the same time.

Note that the final P_W in Cases 1N, 1S, 2N and 2S are (a) significantly lower than the minimum P_W = 2.8 MPa in Cases RN, RS, LN and LS and (b) well below the quadruple point of hydrate, leading to ice formation. Fortunately, the evolving ice does not persist for long, as it is rapidly melted by warmer water flowing toward the well.0

Q_{DF} in Case 2N (**Figure 28**) increases with time, reaching a maximum of 22,400 SCMD (790 MSCFD) at the time of the maxima in Cases 1N and 1S, i.e., at t = 350 days. Q_{DF} in Case 2S takes a long time to recover to, and subsequently exceed, the Q_{DF} levels of Case 2N after each shut-in. The results in **Figure 28** show a repetition of the pattern seen in Case LS that is characterized by a maximum Q_{DF} = 13,600 SCMD (480 MSCFD) that occurs at a time (t = 310 days) well before the minimum P_W is reached, followed by continuous decline in Q_{DF} afterwards.

Possible reasons for this behavior cannot be explained by those proffered in Case LS because of the very different P_W regimes in the two cases. A plausible explanation is the effect of ice formation in the vicinity of the well after P_W dips below the quadruple point P_{QP} of the CH_4 hydrate (P_{QP} = 2.65 MPa). This ice, in combination with the solid hydrate, can significantly reduce the

depressurization effectiveness of the well, leading to the observed Q_{DF} decline. Why this can occur in Case 2S and not in Case 2N can potentially be attributed to warming of the reservoir during shut-ins, effected by (a) advective warmer water inflows and (b) conductive geothermal inflows from the boundaries, in addition to (c) heat released by the exothermic reaction of hydrate reformation in the reservoir, all of which can cause the melting of ice. Thus, the difference in behavior is clearly related to the shut-ins, and is the subject of a continuing investigation. The well shut-in is also followed by rapid hydrate reformation that reaches a maximum (in an absolute sense) of Q_{DF} = 12,900 SCMD (-455 MSCFD) at t = 211.1 days.

Comparison of the Q_{DF} in **Figures 27** and **28** confirms the earlier conclusions that (a) multi-step depressurization schemes (Cases 1N and 1S) are inherently more effective in the release of CH_4 from hydrate dissociation than quasi-linear (continuous) depressurization methods (Cases 2N and 2S), and (b) late-time behavior suggests that shut-ins enhance Q_{DF} in step-wise depressurization schemes, but have a detrimental effect when quasi-linear depressurization is applied; however, more reliable information is to be gleaned from the cumulative production estimates over the duration of the field test..

3.10. Cases 1N, 1S, 2N, 2S: Gas production rates at the well

Figure 29 describes the gas production rates (and their contributors) in Cases 1N and 1S in semi-log and linear plots for maximum clarity of the magnitudes of the various components of production, which cannot be adequately captured by the logarithmic axes of semi-log plots. **Figure 30** provides the same information for Cases 2N and LS, same information. As previously, these figures include the following variables: Q_{PT}, Q_{PG}, Q_{PA}; for reference, the corresponding Q_{DF} plots are also included.

Review of these figures, and a comparison to **Figures 27** and **28** reveal the following:

- In general, Q_{PT} and Q_{DF} do not follow the same patterns observed in Cases Rx and Lx (x = N,S), in which these curves were parallel to each other. This is caused by the very large initial contributions of exsolution gas to Q_{PT}. Such a parallel pattern begins to evolve only very late, i.e., after about 300 days, when Q_{PG} becomes the dominant contributor to Q_{PT}.
- Q_{PT} exceeds Q_{DF} only very late, i.e., after t = 150 and 170 days in Cases 1N and Case 1S, respectively. This is undesirable because it indicates the very long dependence of Q_{PT} on the low Q_{PA} contributions of CH_4 exsolved from water, and the associated large amounts of produced water for a very modest gas production. This is confirmed by the relative magnitudes of Q_{PG} and Q_{PA}, the latter being smaller than the former for t < 130 days in Cases 1N and 1S, 87.5 days in Case 2N and 110 days in Case 2S. Thus, in these cases and until these relatively late times, the well produces mostly water and the majority of the CH_4 produced at the well originates from gas exsolution.
- Q_{PG} becomes the increasingly dominant contributor to Q_{PT} past these times. When this occurs, $Q_{PT} > Q_{PG}$, the two run parallel to each other (see **Figure 29b** and **30b**), and their difference is small. This indicates that most of the gas released from dissociation is produced, and that gas accumulation in the reservoir is expected to be slow and low. The relative magnitudes of Q_{PT} and Q_{PG} in the various mirror those of Q_{DF} observed in **Figures 27** and **28**: they are (a) higher in Case 1S than those in Case 1N and (b) lower in Case 2S than those in Case 2N. Additionally, the Q_{PT} maxima in all cases occur at the times of Q_{DF} maxima: max{Q_{PT}} = 28,650 SCMD (1.012 MMSCFD) in Case 1S > 26,200 SCMD (925 MSCFD) in Case 1N, and max{Q_{PT}} = 10,000 SCMD (352 MSCFD) in Case 2S < 17,300 SCMD (611 MSCFD) in Case 2N.

- Case 2S is characterized by the lowest Q_{DF} and Q_{PT} levels of all four Cases 1x and 2x (**Figure 30b**) for reasons discussed earlier.
- Q_{PT}, Q_{PG} and Q_{PA} in Cases 1N and 1S are consistently (and significantly) higher than those in Cases 2N and 2S, respectively. This is an additional confirmation of the superiority of the multi-step depressurization regime as an effective hydrate dissociation strategy, and is in agreement with the similar observation from Cases RN and RS.
- The information on the evolution of Q_{PT}, Q_{PG}, Q_{PA} over time is insufficient to reach firm conclusions on the possible advantages or disadvantages conferred by shut-ins to production from hydrates following the P_W regimes of Case 1N and 2N. Early shut-ins lead to a decrease in Q_{PT}, but the pattern is reversed later with no clear indication of the overall performance during the length of the production test. Late-time behavior tends to indicate that shut-ins enhance Q_{DF} in step-wise depressurization schemes, but have a detrimental effect when quasi-linear depressurization is applied. Cumulative production data are probably better indicators of the overall behavior.

The contribution of CH_4 from the gas phase (created by the hydrate dissociation and the release of the gas) is evident in **Figure 31**, which shows that $R_{GT} = Q_{PG}/Q_{PT}$ rises very slowly in all cases, consistent with the slow depressurization. Thus, R_{GT} reaches the 80% level after 190 days in all cases, but relapses in Cases 1S and 2S after the second shut-in, requiring an additional 10 and 45 days to reach that level again. On the other hand, and unlike Cases Rx and Lx (x = N,S), R_{GT} continues to increase at late times and after the second shut-in, reaching very high levels approaching 98% because of the increasing gas releases induced by the very low P_W at the end of the production test period. The only notable exception is case 2S, in which R_{GT} declines after t = 310 days; this is attributed to the decline in Q_{PT} that is evident in **Figure 30b**.

Of particular interest is that, although ice does begin to form in the vicinity of the well when P_W decreases below the quadruple point of CH_4 hydrates (about 2.6 MPa), (a) this does not appear to have any negative consequences on the effective permeability, CH_4 release and production (as indicated by the continuously increasing Q_{DF} and Q_{PT}) of Cases 1N, 1S and 2N, and (b) it disappears rapidly, melting under the effect of warmer water flowing toward the well from the deeper within the HU-B layer and from the boundaries. Why this may not occur in Case 2S (a possible reason for its aberrant behavior) is not yet clear.

3.11. Cases 1N, 1S, 1N, 1S: Cumulative volumes of released, produced and free gas

Figures 32a and **32b** describe the cumulative volumes V_{DF} and V_{PT} in Cases (a) 1N and 1S and (b) 1N and 1S, respectively. As stated previously, V_{DF} and V_{PT} are free from the significant variabilities in Q_{DF} and Q_{PT}, respectively – remember that the latter did not allow reaching firm conclusions regarding the effects of the shut-ins over the duration of the production test. Review of these figures reveals the following:

- V_{PT} and V_{DF} follow the same general patterns described earlier in Cases Rx and Lx (x=N,S).
- V_{PT} exceeds V_{DF} for long times in all cases, as expected from the similar relationship between Q_{PT} and Q_{DF} and indicating This is an indication that the HU-B layer is a challenging target when production is based on the depressurization schemes of these cases.
- For reasons expected from the evolution of the relative magnitudes of Q_{DF} and Q_{PT} (**Figures 27** to **30**), and for reasons already explained, CH_4 cumulative release and production in Cases 1N and 1S is consistently higher than that in Cases 2N and 2S, respectively. This is an additional evidence of the superiority of multi-stage depressurization methods.

- The V_{PT} and V_{DF} results indicate that the shut-ins appear to have practically no effect on production in Cases 1N and 1S over the planned 1-year length of this study. The dV_{DF}/dt and dV_{PT}/dt slopes are similar, and the V_{PT} and V_{DF} curves from Cases 1N and 1S practically coincide at t = 1 year with those from the uninterrupted Cases 1N and 1S. The pattern is completely different in Cases 2N and 2S, which show divergence of V_{PT} and V_{DF} as time advances, with cumulative release and production in Case 2N significantly outperforming those in Case 2S.
- However, the pattern changes at later times, and shut-ins lead to higher V_{PT} and V_{DF} in Case 1S than in Case 1N for t > 1 year. This superiority is certain to continue, as indicated by the rates in **Figure 29**. The obvious general conclusion mirrors earlier realizations: shut-ins are beneficial in the long run when production is based on multi-stage depressurization, but have a detrimental effect in quasi-linear depressurization schemes.
- The evolution of the amount of the free gas V_F in the reservoir over time (**Figure 33**) is also in agreement with the previous observations. The significant reduction in (and even disappearance of) the free gas caused by the hydrate reformation during the shut-ins is rapidly overcome in Cases 1S and is slower in Case 2S; following the second shut-in, V_F in Case 1S rapidly converges toward (and eventually coincides with) that from the uninterrupted Case 1N near the 1-year mark, and then exceeds it at later times. V_F in Case 2S reaches (and briefly exceeds) the Case 1N level, but is consistently lower for t > 335 days.

3.12. Cases 1N, 1S, 1N, 1S: Water production rates

Figures 34a and **34b** show the evolution over time of Q_{wW}, Q_{wT}, Q_{wB} and Q_{wA} in Cases 1N and 1S, respectively. **Figures 35a** and **35b** show the same information for Cases 2N and 2S, respectively. As in Cases Rx and Lx (x=N,S), the simulation results indicated no water and/or heat exchanges (a) between the interior of the domain and its top horizontal, bottom horizontal and outer radial boundary at r = 800 m, and (b) between the HU-C and HU-D layers and their adjacent units/boundaries.

Review of these figures reveals the following:

- The water production rates at the well Q_{wW} increase consistently as time advances in all cases; while shut-ins in Cases 1S and 1S lead to spikes after the resumption of production (for reasons already explained), these last for very short periods, and the resulting Q_{wW} maximum values do not appear excessive: the long-term trends (even with spikes included) are in the 3,000 BPD range in Cases 1N and 1S, and in the 1,900-2,200 BPD range in Cases 2N and 2S.
- Water inflows from the boundaries are significant, with contribution of the bottom boundary $Q_{wB} > Q_{wT}$ for the same reasons discussed in Cases RN, RS, LN and LS.
- Q_{wA} represents a large fraction of Q_{wW}, indicating replenishment of the native free water and that released from the hydrate dissociation by water inflows from the top and bottom boundaries, with all the associated negative implications (discussed earlier).
- Spikes excluded, as expected from the associated Q_{PT} behavior, the shut-ins lead to long-term trends of an increase in Q_{wW} in Cases 1N and 1S over those in Cases 2N and 2S for most of the duration of the simulated test. Case 2S shows a near constant Q_{wW} for t > 310 days. This is consistent with the explanation of possible ice formation near the well that has the potential to reduce the effective permeability and the fluid production (**Figure 30b**).

- As in Cases Rx and Lx (x = N,S) , shut-ins do not appear to have a significant impact on water production, as the cessation of production is followed by higher rates when depressurization resumes.

3.13. Cases 1N, 1S, 2N, 2S: Water-related parameters

Figure 36 shows the evolution of R_{WG} of the relative criterion in these cases. R_{WG} initially declines from a very high initial level of over 330 (when water is the only produced fluid and the only CH_4 is that obtained from exsolution) to as low as 30 (Case 2S) or 20 (Cases 1N, 2N and 1S). The long-term trend is decreasing until a certain time (t = 350 days for most cases), indicating limited water inflows from the boundaries until that time; water inflows increase afterwards, leading to higher R_{WG}. The exception is Case 2S, which shows an upward trend for t > 310 days that can be attributed to boundary water inflows under conditions of reduced water production. As evidenced from **Figure 36b**, the adverse effect of shut-ins on the magnitude of R_{WG} and its evolution over time is rather significant when applying the design of Cases 1S or 2S to the test targeting the HU-B layer.

The significant water inflows from the boundaries are also further confirmed by the replenishment ratio of water, defined by $R_{BW} = Q_{wA}/Q_{wW}$ and described for all cases in **Figure 37**. R_{BW} in all cases are in the 70-80% range almost from the onset of production until about 80 days, and exceeds the 80% until about t = 300 days in Cases 1N, 1S and 2N; after that time, R_{BW} (a) first declines until t = 350 days, probably because large amounts of released gas may inhibit water flow into the domain through its boundaries and (b) then increases continuously because of increased water inflows. The well shut-ins in Cases 1S and 2S lead to complex R_{BW} behavior: there appears to be a significant R_{BW} reduction in Case 2S, and a very minor one in Case 1S after the first shut-in; after the second shut-in, R_{BW} decreases to very low levels in Case 1S, from which it recovers rapidly. Conversely, R_{BW} in Case 2S is much higher (approaching 1) when production resumes, but then it declines slowly. The reasons for these behaviors of Case 2S (as well as those identified earlier) are unclear at this point, and the subjects of continuing investigations.

3.14. Cases 1N, 1S, 2N, 1S: Response in the observation wells

Figures 38, **39** and **40** show the evolution of P, T and of the pore-volume averaged gas saturation S_G in the two observation wells in all these cases. The evolution of P in **Figure 38** captures all the changes in the P_W regimes in the various cases, allowing clear identification of all times when the P_W changes. Thus, the multiple depressurization stages in Case 1N, the quasi-linear P_W decline in Case 1N, and the shut-ins in Cases 1S and 1S are identified by unmistakable inflection points that mark the known times of change. The continuously decreasing P as time advances is probably associated with the limited water inflows resulting from adverse relative permeability to water caused by the large CH_4 releases the final (and very low) P_W is reached. The flattening of the P curves at very late times are clear indications of water inflows from the boundaries.

The first shut-ins in Cases 1S and 2S are captured by the T-response in **Figure 39**, but the associated disturbance is much less pronounced than that of P. Compared to the fast P-response caused by the relative incompressibility of water, the T-response in **Figure 39** (a much more reliable, but still indirect, indicator of hydrate dissociation) shows a significant delay in Cases 1N and 1S, beginning to register temperature changes clearly associated with hydrate dissociation at t = 170 days and t = 190 day at the O30 and the O50 well, respectively. Note the very weak (barely discernible) T-response to the 1st shut-in, which can be potentially overlooked or mischaracterized

as measurement error. In the smoother-declining P_W of Cases 2N and 2S, the first T-based indication of dissociation is registered at about 160 days at the O30 well, and at about 190 days in the O50 well. Beyond these times, sharp T-reductions in all four cases of **Figure 39** (and increases after the second shut-ins in Cases 1S and 2S) appear to be strong indications of continuing reactions of hydrate dissociation or formation in the HU-B layer. The lower temperatures in Cases 1N and 1S are indicative of the more active dissociation of the associated depressurization scheme (see **Figures 29** and **30**). All the temperature indications of hydrate dissociation or formation are in complete agreement with the evolution and occurrence of free gas denoted by $S_G > 0$ at the location of the wells (**Figure 40**).

The S_G response in the observation wells completely misses the first shut-in Cases 1S and 2S, and this may be a factor that can affect the selection of the depressurization regime to be used in the production test. S_G appears to be continuously increases at the observation wells in all cases until about the time when the maximum levels of Q_{DF} and Q_{PT} are observed (see **Figures 29** and **30**), reflecting the continuing (and increasing) hydrate dissociation and (possibly) indicating the limited water inflows suggested by other previously discussed parameters until these times. Beyond these times, there is a decreasing S_G trends in both wells that is clearly related to (and possibly explained by) the sharp decline in Q_{DF} and Q_{PT} that begin at the same times.

These results indicate that observation wells are appropriately positioned and both able to capture the P, T and S_G behavior during the gas production from the HU-B layer in any of the eight cases investigated in this study.

Summary and Conclusions

We investigate by means of numerical simulation a planned year-long field test of depressurization-induced production from a permafrost-associated hydrate reservoir on the Alaska North Slope at the site of the recently-drilled Hydrate-01 Stratigraphic Test Well, the installation of which provided evidence of the suitability of the test site. The main objective of this study is to assess quantitatively the impact of temporary interruptions (well shut-ins) on the expected fluid production performance from the well-characterized and strongly heterogeneous gas hydrate accumulation in the B1 Sand of the stratigraphic Unit B during controlled depressurization over different time scales, as well as on other relevant aspects of the system response that have the potential to significantly affect the design of the field test. Such interruptions in productions are a virtual certainty because of scheduled and required well-servicing operations or because of unintended disruptions. An additional objective is to glean from the various test cases we investigate any additional information that can be used to formulate decisions on production strategies and to improve the overall design not only of the long-term test, but also of possible future production activities under these or similar conditions.

We investigate a total of eight cases:

- Cases Rx and Lx (x = N,S), defined by bottomhole pressure P_W schedules that involve respectively (a) a reference case of rapid 3-step depressurization regime and (b) a rapid linear depressurization regime, both to a final P_W = 2.8MPa over a 60-day period, beyond which P_W remains constant until the end of the year-long test (**Figure 6**). The final P_W precludes the emergence of ice in the hydrate deposit. The “S” in the case b=names indicates the occurrence of 2 shut-ins, and “N” moniker denotes uninterrupted operation.
- Cases 1x and 2x (x = N,S), defined by bottomhole pressure P_W schedules that involve respectively (a) multi-step depressurization regime and (b) a quasi-linear depressurization regime, both to a final P_W = 0.6 MPa over the test period (**Figure 7**). The “S” and “N”

monikers in the case names are as defined above. The final pressure is well below the quadruple point P_{QP} of CH_4-hydrate, indicating that the formation of ices is possible in the course of the test.

We compare key performance metrics for the various production scenarios, and their evolution over the duration of the test. Based on the results of this study, the following conclusions can be reached:

(1) In terms of the cumulative gas release V_{DF} and cumulative gas production V_{PT} over the production test duration, the impact of the shut-ins in the various cases is non-uniform, and is strongly related to the different P_W regimes.

(2) Shut-ins obviously reduce gas release and production during and immediately after their occurrence, but their longer-term effects are strongly dependent on the depressurization regime and on the time of observation, covering the entire range of potential outcomes.

(3) Shut-ins lead to higher long-term release and production rates (Q_{DF} and Q_{PT}, respectively) and cumulative volumes (V_{DF} and V_{PT}, respectively) in the cases associated with multi-step depressurization (Cases RS and 1S) over the cases of uninterrupted production (Cases RN and 1N), and the benefits increase and become evident earlier if the initial pressure drops are substantial. In a certain sense, shut-ins appear to have a positive effect on the long-term production performance, and this is attributed to (a) drainage of the released water that leads to more pronounced phase segregation and gas accumulation near the reservoir top, which can lead to enhanced gas production, (b) larger depressurization at the well ΔP_W and, consequently, more effective dissociation because of reservoir pressure recovery after the shut-ins, and higher temperatures caused by (c) conduction-driven geothermal inflows, (d) warmer water advective inflows from the boundaries into the colder reservoir, as well as (e) the exothermic reactions of hydrate reformation. If this observation is confirmed by more simulation and field studies, scheduled shut-ins may become part of strategies for maximizing gas production from hydrate accumulations.

(4) Conversely, shut-ins appear to have a decidedly detrimental effect on the release and production rates (Q_{DF} and Q_{PT}, respectively) and cumulative volumes (V_{DF} and V_{PT}, respectively) in all shut-in cases associated with quasi-linear (continuous) depressurization (Cases LS and 2S), which have a consistently and substantially lower performance than the cases of uninterrupted production (Cases LN and 2N).

(5) For the year-long production test, shut-ins do not appear to have a significant practical impact on V_{DF} and V_{PT} in Cases 1S and 1N, as their predictions converge at the end of the test.

(6) Shut-ins lead to a rapid reformation of hydrates, even to the point of disappearance of a free gas phase in the reservoir.

(7) Shut-ins lead to increased terminal rates (i.e., at the end of the production test) of gas production Q_{PT} in Cases RS and 1S (involving multi-step depressurization regimes) over those in Cases RN and 1N, respectively. The opposite occurs in Cases LS and 2S (involving near-linear depressurization regimes), in which the terminal Q_{PT} are lower than those in the uninterrupted Cases LN and 2N. The significant variability in the Q_{PT} over the duration of the test makes V_{PT} a more reliable criterion for the evaluation of the impact of the production interruptions.

(8) Shut-ins lead to somewhat higher terminal rates of water production Q_{wW} in Cases RS and 1S (in the 2500 BPD range, with spikes in the 3000 BPD range) than those in Cases RN and 1N, respectively. The opposite occurs in Cases LS and 2S (involving near-linear

depressurization regimes), in which the terminal Q_{wW} are lower than those in the uninterrupted Cases LN and 2N.

(9) Shut-ins do not appear to have a significant impact on water production, as the cessation of production is followed by production at higher rates when depressurization resumes. Similarly, (a) the fraction of produced CH4 originating from exsolution from the water, (b) the water-to-gas ratio, and (c) the rate of replenishment of produced water by boundary inflows do not appear significantly affected by shut-ins, the effects of which seem to be temporary in most cases.

(10) Cases Rx and Lx (x=N,S) have a drastically different behavior than that of Cases 1x and 2x because of the difference in the depressurization schedules. In the former, maximum Q_{DF} and Q_{PT} levels are attained at or immediately after the final $P_W = 2.8$ MPa is reached; in the latter, Q_{DF} and Q_{PT} continue to increase until the end of the production test in response to the continuously decreasing P_W. Case 2S exhibits a different behavior, with Q_{DF} and Q_{PT} declining after $t = 310$ days, a behavior attributed to ice formation near the well that cannot be melted by invading warmer water during the length of the test, possibly because of the spatial distribution and saturation levels caused by the second shut-in.

(11) Further on the subject of differences between (a) Cases Rx and Lx and (b) Cases 1x and 2x: the levels of V_{PT} in the former far exceed those in the latter, being more than double. On the other hand: the terminal levels of Q_{PT} in Cases 1N, 1S and 2N are much larger than those in Cases RN, RS, LN and LS, the latter being on the same order as Q_{PT} in Case 2S; conversely, the early Q_{PT} in Cases 1x and 2x are very low and remain so for a long time, compared to those from Cases Rx and Lx. These observations may be serve as a criterion for the selection of the depressurization strategy to be followed during the test.

(12) Additionally on the subject of differences between the cases and on criteria for selection of the P_W regime: exsolved CH_4 (rather than that released from hydrate dissociation) is the main source of the produced CH_4 for very long times in Cases 1x and 2x, providing more that 50% of Q_{PT} for 100 days or longer, and requiring more than 170 days to drop below 20%. This is an indicator of ineffective dissociation, as mostly water and little gas is initially produces in these cases given the low solubility of CH_4 in water. On the other hand, hydrate-originating gas (as described by the R_{GT} term) provides over 80% of Q_{PT} as early as $t = 30$ days in the rapidly depressurized Cases Rx and Lx, and 90+% after 90 days.

(13) In all cases, multi-step depressurization is shown to be a far superior choice to that of continuous, quasi-linear depressurization, resulting in consistently larger gas production rates. This confirms the earlier laboratory findings of Gao et al.[47] and our early scoping calculations.

(14) The water-to-gas ratios R_{WG} in Cases Rx and Lx recline rapidly from an initial level of 220 to about (a) 15 in 30 days (Cases RN and RS) and (b) 30 in 150 to 160 days (Cases LN and LS), after which times they begin to slowly increase because of water inflows from the boundaries. The decline in R_{WG} in Cases 1x and 2x occurs at a much slower pace, beginning with an initial $R_{WG} = 330$ and decreasing to $R_{WG} = 30$ after more than 300 days, reflecting the more inefficient dissociation by the associated P_W regimes of slow depressurization.

(15) In all 8 cases, the water replenishment ratio (reflecting replacement of produced water by boundary inflows) R_{BW} reaches and exceeds the 80% level within 30 days or less, and remains consistently at this or a higher level for the rest of the production test. Actually, R_{BW} can reach (and occasionally exceed) 100% in Cases Rx and Lx near the end of the

production test. This indicates that water inflows from the underburden and the overburden of the targeted hydrate-bearing layer are a consistent problem, limiting the effectiveness of depressurization and, consequently, that of hydrate dissociation.

(16) Two observation wells located at distances of 30 m and 50 m from the production well are appropriately positioned and both able to capture the P, T and S_G behavior in response to P_W changes during the gas production from the hydrate-bearing B1 Sand layer of Unit B in any of the eight cases investigated in this study. The pressure observations in both wells capture all changes in the P_W almost immediately in the rapidly dissociating Cases Rx and Lx, and much slower in the slower depressurized Cases 1x and 2x. The pressure response is consistently faster than the temperature response in all cases because of the very low compressibility of water that enables rapid migration of the pressure front, while temperature registers changes caused by fluid advection, heat conduction and hydrate dissociation, all of which advance at a lower pace than the pressure front. However, the temperature response in all cases also captures all changes in the P_W regimes, but may be affected by water inflows at late times. Additionally, the T-response to the 1st shut-in is very weak in Cases 1x and 2x, and can be potentially overlooked or mischaracterized as measurement error. The evolution of a free gas phase is the most reliable and the only direct indicator of hydrate dissociation. It is the slowest to emerge and it also captures all P_W changes in the rapidly depressurized Cases Rx and Lx. Thus, free gas at the r = 30 m observation well is observed as early as 30 days in the Rx cases and 50 days in the Lx cases. The emergence of free gas is much slower in the slowly-depressurized Cases 1x and 2x, taking at least 150 days to be detected in the observation wells, and the S_G response is unable to capture the first shut-in in these cases. Because of the importance of observation wells as the only means to monitor the system performance, the difference in their observations may be used as an additional criterion for the selection of the appropriate depressurization regime to be applied during the test. For obvious reasons, the response of the r = 50 observation well is consistently slower than that of the r = 30 m well. The onset of shut-ins is easily discernible in the response of the observation wells, identified by (a) P- and T- increases caused by inflows from the boundaries and (b) S_G decreases (even to zero levels) caused by hydrate regeneration fueled by the increasing pressures.

Acknowledgment

This work was supported by the Assistant Secretary for Fossil Energy, Office of Natural Gas and Petroleum Technology, through the National Energy Technology Laboratory, under the U.S. Department of Energy, Contract No. DE-AC02-05CH11231. This research used the Lawrencium computational cluster resource provided by the IT Division at the Lawrence Berkeley National Laboratory, supported by the Director, Office of Science, Office of Basic Energy Sciences, of the U.S. Department of Energy under Contract No. DE-AC02-05CH11231.

Alaska gas hydrate research is being conducted as a collaboration between Japan MH21-S and the U.S. DOE-NETL Gas Hydrate R&D program. The authors would like to express their sincere appreciation to the U.S. DOE-NETL, and the Japan Ministry of Economy, Trade, and Industry for providing the permission to disclose this research. Any use of trade, product, or firm names is for descriptive purposes only and does not imply endorsement by the U.S. Government or the Japanese Government.

References

(1) Boswell, R. and Collett, T.S., 2011. Current perspectives on gas hydrate resources. *Energy & Environmental Science*, **4** (4): 1206-1215.

(2) Boswell, R., Schoderbek, D., Collett, T.S., Ohtsuki, S., White, M. and Anderson, B.J., 2017. The Iġnik Sikumi Field Experiment, Alaska North Slope: Design, Operations, and Implications for CO2–CH4 Exchange in Gas Hydrate Reservoirs. *Energy & Fuels* **31**(1): 140-153.

(3) Dallimore, S.R., Yamamoto, K., Wright, J.F. and Bellefleur, G., 2012. Proof of concept for gas hydrate production using the depressurization technique, as established by the JOGMEC/NRCan/Aurora Mallik 2007–2008 Gas Hydrate Production Research Well Program. *Geological Survey of Canada, Bulletin* **601**: 1-15.

(4) Kurihara, M., Sato, A., Funatsu, K., Ouchi, H., Masuda, Y., Narita, H. and Collett, T.S., 2011. Analysis of formation pressure test results in the Mount Elbert methane hydrate reservoir through numerical simulation. *Marine and Petroleum Geology* **28**: 502-516.

(5) Konno, Y., Kato, A., Yoneda, J., Oshima, M., Kida, M., Jin, Y., Nagao, J. and Tenma, N., 2019. Numerical analysis of gas production potential from a gas-hydrate reservoir at Site NGHP-02-16, the Krishna–Godavari Basin, offshore India–Feasibility of depressurization method for ultra-deepwater environment. *Marine and Petroleum Geology* **108**: 731-740.

(6) Yamamoto, K., Suzuki, K., Wang, X., Matsunaga, T., Nishioka, I., Nakatsuka, Y. and Yoneda, J., 2019. The second offshore production test of methane hydrates in the Eastern Nankai Trough and site characterization efforts. Fire in the Ice: Department of Energy, Office of Fossil Energy, National Energy Technology Laboratory, *Methane Hydrate News Letter* **19** (1): 9-15.

(7) Yamamoto, K., Boswell, R., Collett, T., Dallimore, S., Lu, H., 2022. Review of past gas production attempts from subsurface gas hydrate deposits and necessity of long-term production testing. *Energy & Fuels*. https://pubs.acs.org/doi/10.1021/acs.energyfuels.1c04119

(8) Dallimore, S.R., Wright, J.F., Yamamoto, K. and Bellefleur, G., 2012. Proof of concept for gas hydrate production using the depressurization technique, as established by the JOGMEC/NRCan/Aurora Mallik 2007-2008 Gas Hydrate Production Research Well Program. *Bulletin of the Geological Survey of Canada* **601**: 1-15.

(9) Ashford, D.I., Numasawa, M., Martin, C.K., Yamamoto, K., Dallimore, S.R., Wright, J.F., Nixon, F.M., Applejohn, A. and Taylor, A.E., 2012. Overview of engineering and operations activities conducted as part of the JOGMEC/NRCan/Aurora Mallik 2007–2008 Gas Hydrate Production Research Well Program, Part A: 2007 field program. Scientific results from the JOGMEC/NRCan/Aurora Mallik 2007-2008 gas hydrate production research well program, pp.35-51.

(10) Li, J.-F., Ye, J.-L., Qin, X.-W., Qiu, H.-J., Wu, N.-Y., Lu, H.-L., Xie, W.-W., Lu, J., Peng, F., Xua, Z.-Q., Lu, C., Kuang, Z.-G., Wei, J.-G., Liang, Q.-Y., Lu, H.-F. and Kou, B.-B., 2018, The first offshore natural gas hydrate production test in South China Sea. *China Geology* **1**: 5−16.

(11) Moridis, G. J., Collett, T. S., Boswell R., Kurihara M., Reagan M. T., Koh C., and Sloan E. D. 2009. Toward Production From Gas Hydrates: Current Status, Assessment of Resources, and Simulation-Based Evaluation of Technology and Potential, *SPE Res Eval & Eng* **12** (5): 745-771. SPE-114163-PA.

(12) Boswell, R., Hancock, S., Yamamoto, K., Collett, T., Pratap, M., Lee, S.-R., 2020. Natural gas hydrates: status of potential as an energy resource, In: T.M. Letcher (Editor), Future Energy (Third Edition). Elsevier, Boston, pp. 111-131.

(13) Moridis, G.J., Collett, T.S., Pooladi-Darwish, M., Hancock, S., Santamarina, C., Boswell, R., Kneafsey, T., Rutqvist, J., Kowalsky, M.J., Reagan, M.T., Sloan, E.D., Sum, A.K., and Koh,

C., 2011, Challenges, Uncertainties and Issues Facing Gas Production From Hydrate Deposits in Geologic Systems. *SPE Res. Eval. & Eng* **14** (1): 76-112.

(14) Boswell, R., Myshakin, E., Moridis, G.J., Konno, Y., Collett, T.S., Reagan, M.T., Ajayi, T., Seol, Y., 2018, India National Gas Hydrate Program Expedition 02 summary of scientific results: Numerical simulation of reservoir response to depressurization, J. *Marine and Petroleum Geology* **108**: 154-166.

(15) Moridis, G., M.T. Reagan and A.F. Queiruga, 2019. Gas Hydrate Production Testing: Design Process and Modeling Results, OTC-29432-MS, paper presented at the 2019 Offshore Technology Conference, 6 – 9 May 2019, Houston, Texas.

(16) Boswell, R., Collett, T., Okinaka, N., Hunter, R., Suzuki, K., Tamaki, M., Yoneda, J., Haines, S., Itter, D., Myshakin, E., Moridis, G., 2022. Alaska North Slope Hydrate-01 Stratigraphic Test Well Program: Technical Results. *Energy & Fuels* https://pubs.acs.org/doi/10.1021/acs.energyfuels.2c00327

(17) Collett, T., Zyrianova, M., Okinaka, N., Wakatsuki, M., Boswell, R., Marsteller, S., Minge, D., Crumley, S., Itter, D., Hunter, R., Garcia-Ceballos, A., Jin, G., 2022. Design and operations of the Hydrate-01 stratigraphic test well, Prudhoe Bay Unit, Alaska North Slope. *Energy & Fuels* https://pubs.acs.org/doi/10.1021/acs.energyfuels.1c04087

(18) Haines, S. S., Collett, T., Yoneda, J., Shimoda, N., Boswell, R., Okinaka, 2022, Gas Hydrate Saturation Estimates, Gas Hydrate Occurrence, and Reservoir Characteristics Based on Well Log Data from the Hydrate-01 Stratigraphic Test Well, Alaska North Slope, *Energy & Fuels* https://pubs.acs.org/doi/10.1021/acs.energyfuels.1c04100

(19) Tamaki, M., Fujimoto, A., Boswell, R., Collett, T., 2022. Geological reservoir characterization of a gas hydrate prospect associate with the Hydrate-01 stratigraphic test well, Alaska North Slope. *Energy & Fuels* https://pubs.acs.org/doi/10.1021/acs.energyfuels.2c00336

(20) Uchida, S., Seol, Y., Yamamoto, K.,2022. Sand migration simulation during gas production from gas hydrate reservoir at Kuparuk State 7-11-12 site in the Prudhoe Bay Unit, Alaska. *Energy & Fuels* https://pubs.acs.org/doi/10.1021/acs.energyfuels.2c00046

(21) Nakajima, C., Ouchi, H., Tamaki, M., Akamine, K., Sato, M., Otsuki, S., Naiki, M., 2022. Sensitivity and uncertainty analysis for natural gas hydrate production testing in Alaska. *Energy & Fuels* https://pubs.acs.org/doi/10.1021/acs.energyfuels.2c00335

(22) Myshakin, E., Garapati, N., Seol, Y., Gai, X., Boswell, R., Ohtsuki, S., Kumagai, K., Sato, M., Suzuki, K., Okinaka, N., 2022. Numerical simulations of depressurization-induced gas hydrate reservoir (B1 sand) response at the Prudhoe Bay Unit Kuparuk 7-11-12 pad on Alaska North Slope. *Energy & Fuels* https://pubs.acs.org/doi/10.1021/acs.energyfuels.1c04099

(23) Zhang, J., Development of a Parallel Geomechanics Code Based on the Message-Passing-Interface (MPI) Approach and Iterative Coupling with a Parallelized Flow and Thermal Simulator for the Analysis of System Behavior in Hydrate-Bearing Geologic Media, PhD Dissertation, Petroleum Engineering Dept., Texas A&M University, College Station, Texas, August 2021.

(24) Zhang, J., G.J. Moridis and T.A. Blasingame, Message-Passing-Interface (MPI) Parallelization of Iteratively Coupled Fluid Flow and Geomechanics Codes for the Simulation of System Behavior in Hydrate-Bearing Geologic Media, Paper Presented at the 2021 SPE Annual Technical Conference and Exhibition, Dubai World Trade Centre, Dubai, United Arab Emirates, September 2021. SPE-206161-MS.

(25) Moridis, G. J. and Pruess K. 2014. User's Manual for the TOUGH+ Core Code v1.5: A General-Purpos Simulator of Non-Isothermal Flow and Transport Through Porous and Fractured Media. Lawrence Berkeley National Laboratory, Berkeley, California, USA.

(26) Moridis, G. J. 2014. User's Manual for the Hydrate v1.5 Option of TOUGH+ v1.5: A Code for the Simulation of System Behavior in Hydrate-Bearing Geologic Media. Lawrence Berkeley National Laboratory, Berkeley, California, USA.

(27) Moridis, G.J., Reagan, M.T., Queiruga, A.F., Collett, T.S., Boswell, R., 2019. Evaluation of the Performance of the Oceanic Hydrate Accumulation at the NGHP-02-9 Site of the Krishna-Godawari Basin During a Production Test and During Single and Multi-Well Production Scenarios. *Marine and Petroleum Geology* **108**: 660-696.

(28) Moridis, G. J. and Reagan, M. T. 2007. Strategies for Gas Production from Oceanic Class 3 Hydrate Accumulations. Paper Presented at the Offshore Technology Conference, Houston, Texas, USA, 30 April - 3 May. OTC-18865-MS.

(29) Moridis, G. J., Kowalsky, M. B., and Pruess, K. 2007. Depressurization-Induced Gas Production from Class 1 Hydrate Deposits. *SPE Reservoir Evaluation and Engineering* **10** (5): 458-481. SPE-97266-PA.

(30) Moridis, G. J. and Reagan, M. T. 2007. Gas Production from Oceanic Class 2 Hydrate Accumulations. Paper Presented at the Offshore Technology Conference, Houston, Texas, USA, 30 April–3 May. OTC-18866-MS.

(31) Moridis, G. J. and Reagan, M. T. 2011. Estimating the Upper Limit of Gas Production from Class 2 Hydrate Accumulations in the Permafrost, 1: Concepts, System Description and the Production Base Case. *Journal of Petroleum Science and Engineering* **76**: 194-201.

(32) Moridis, G. J. and Reagan, M. T. 2011. Estimating the Upper Limit of Gas Production from Class 2 Hydrate Accumulations in the Permafrost, 2: Alternative Well Designs and Sensitivity Analysis. *Journal of Petroleum Science and Engineering* **76**: 124-137.

(33) Moridis, G. J. and Sloan, E. D. 2007. Gas Production Potential of Disperse Low-Saturation Hydrate Accumulations in Oceanic Sediments. *Energy Conversion and Management* **48** (6): 1834-1849.

(34) Li, G., Moridis, G. J., Zhang, K., and Li, X.-S. 2010. Evaluation of Gas Production Potential from Marine Gas Hydrate Deposits in Shenhu Area of the South China Sea. *Energy & Fuels* **24**: 6018-6033.

(35) Moridis, G. J., Reagan M. T., Boyle, K. L., and Zhang, K. 2011c. Evaluation of the Gas Production Potential of Some Particularly Challenging Hydrate Deposits. *Transport in Porous Media* **90**: 269-299.

(36) Karypis, G. and Kumar, V. 1998. Multilevelk-way Partitioning Scheme for Irregular Graphs. *Journal of Parallel and Distributed Computing* **48** (1): 96-129.

(37) Karypis, G. and Kumar, V. 1999. Parallel Multilevel Series k-way Partitioning Scheme for Irregular Graphs. *SIAM Review* **41** (2): 278-300.

(38) Balay, S., Abhyankar, S., Adams, M. F., Brown, J., Brune, P., Buschelman, K., and Kaushik, D. 2014. PETSc User's Manual. Argonne National Laboratory, Lemont, Illinois, USA.

(39) Yoneda, J., Suzuki, K., Jin, Y., Otsuki, S., Collett, T., Boswell, R., Okinaka, N., 2022. Permeability measurement and prediction with nuclear magnetic resonance analysis of gas hydrate-bearing sediments recovered from Alaska North Slope 2018 Hydrate-01 stratigraphic test well. *Energy & Fuels* https://pubs.acs.org/doi/10.1021/acs.energyfuels.1c03810

(40) Rutqvist, J., G.J. Moridis, T. Grover, and T. Collett, 2009. Geomechanical response of permafrost-associated hydrate deposits to depressurization-induced gas production. *Journal of Petroleum Science and Engineering* **67**:1-12.

(41) Moridis, G.J., S. Silpngarmlert, M.T. Reagan, T.S. Collett, and K. Zhang, 2011. Gas Production from a Cold, Stratigraphically Bounded Hydrate Deposit at the Mount Elbert Site,

North Slope, Alaska. *Marine Petrol. Geol.* **28**: 517-534.

(42) vanGenuchten, M.Th., 1980. A Closed-Form Equation for Predicting the Hydraulic Conductivity of Unsaturated Soils. *Soil Sci.* **44**: 892 - 898.

(43) Moridis, G.J., A.F. Queiruga and M.T. Reagan, 2019. Simulation of Gas Production from Multilayered Hydrate Bearing Media with Fully Coupled Flow, Thermal, Chemical, and Geomechanical Processes Using TOUGH+Millstone: Part 1: Numerical Modeling of Hydrates. *Transport in Porous Media* **128** (2): 405-430.

(44) Moridis, G. J. 2016. User's Manual of the Meshmaker v1.5 Code: A Mesh Generator for Domain Discretization in Simulations of the TOUGH+ and TOUGH2 Families of Codes. Lawrence Berkeley National Laboratory, Berkeley, California, USA.

(45) Moridis, G.J. and N. Keen, MeshMaker V2.0S and V2.0P, 2015. New Grid Generators for Complex Heterogeneous Domains in TOUGH2/TOUGH+ Simulations, Proceedings of the 2015 TOUGH Symposium, Berkeley, California, September 28-30.

(46) Kowalsky, M.B. and G.J. Moridis, 2007. Comparison of kinetic and equilibrium reactions in simulating the behavior of gas hydrates. *Energy Conversion and Management* **48**: 1850.

(47) Gao, Q., Yin, Z., Zhao, J., Yang, D., Linga, P., 2021. Tuning the fluid production behaviour of hydrate-bearing sediments by multi-stage depressurization. *Chemical Engineering Journal* **406**: paper 127174.

Table 1 – Flow and thermal properties

Parameter	Value
Initial pressure P_0	Hydrostatic
Geothermal gradient dT/dz	0.037 ^{o}C/m
Initial S_H	Figure 4 (HU-B layer); Eq. 1 (Layers HU-B and HU-C)
Gas composition	100% CH_4
Intrinsic permeability k, all units	Figure 2
Porosity ϕ, all units	Figure 2
Grain density ρ_R (all formations)	2700 kg/m^3 (all media)
Specific heat	835 J/kg/K (Units B,C,D), 1000 J/kg/k elsewhere
Wet thermal conductivity ($k_{\Theta RW}$)	3.8 W/m/K (all formations)
Wet thermal conductivity ($k_{\Theta RD}$) (all formations)	(1-ϕ) $k_{\Theta RW}$ (all formations)
Composite thermal conductivity model (Moridis et al., 2014)	$k_{\Theta C} = k_{\Theta RD} + (S_A^{1/2}+S_H^{1/2})\,(k_{\Theta RW} - k_{\Theta RD}) + \phi\, S_I\, k_{\Theta I}$
Capillary pressure model (vanGenuchten, 1980)	$P_{cap} = -P_0 \left[\left(S^*\right)^{-1/\lambda} - 1 \right]^{1-\lambda}$ $S^* = \dfrac{\left(S_A - S_{irA}\right)}{\left(S_{mxA} - S_{irA}\right)}$
λ	0.45 (Units B,C,D); 0.15 (all other media)
P_0	10^4 Pa (Units B,C,D); 10^5 Pa (all other media)
Relative permeability model - EPM (Moridis et al., 2008a)	$k_{rA} = (S_A^*)^n$ $k_{rG} = (S_G^*)^m$ $S_A^* = (S_A - S_{irA})/(1 - S_{irA})$ $S_G^* = (S_G - S_{irG})/(1 - S_{irA})$
n; $m = n - 0.5*Max(0.0, n-2)$	Figure 4 (Units B,C,D) Analogs for interlayers and underburden
S_{irG}	0.01 (all units)
S_{irA}	Figure 2

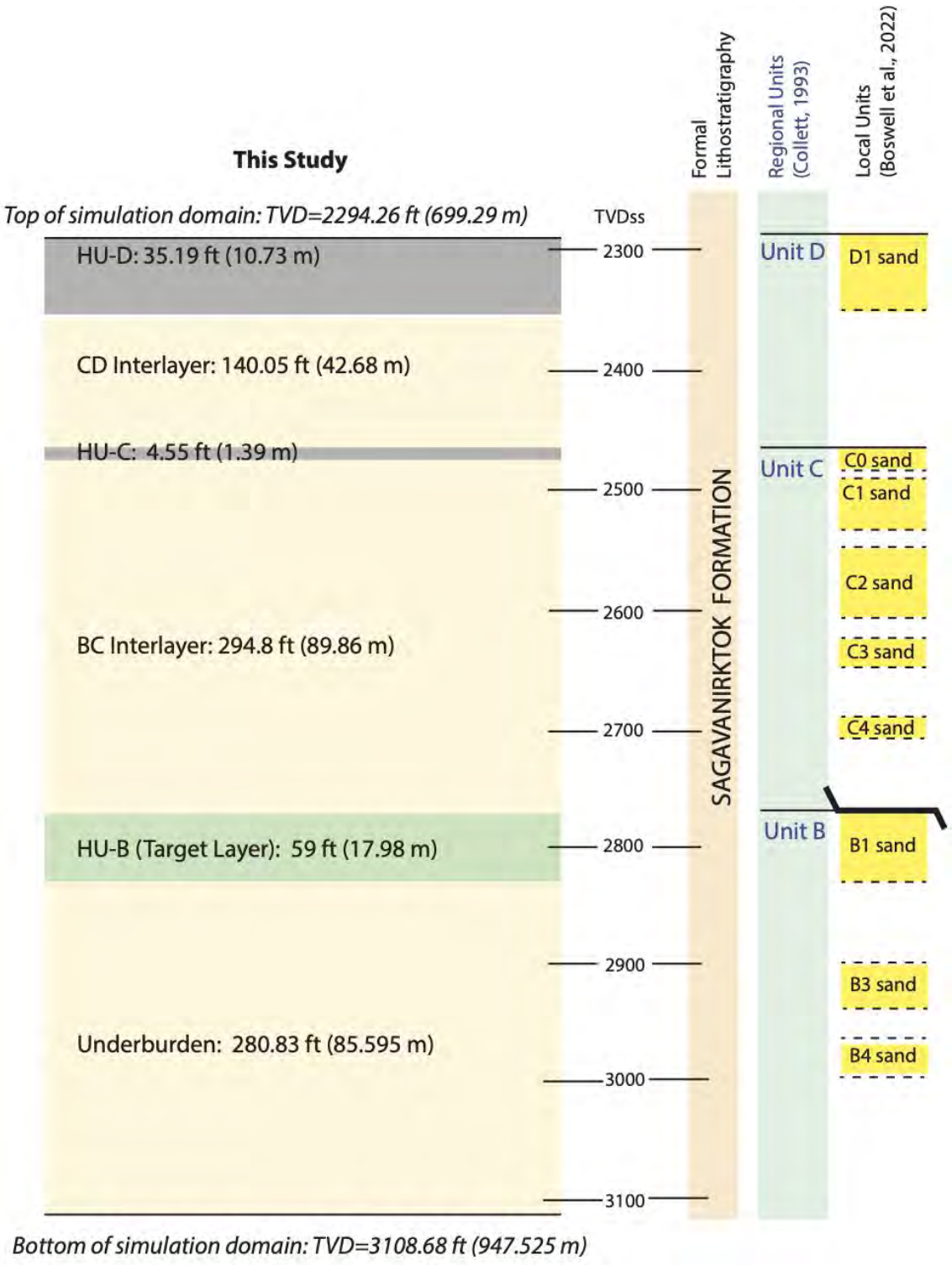

Fig. 1. Stratification and dimensions of the simulation domain (not to scale), and its relationship to the stratigraphy at the site of the planned field test of long-term production from hydrate deposits on the North Slope of Alaska. The terms HU-B, HU-C and HU-D denote the hydrate-bearing layers of the B1 Sand, C0 Sand and D1 Sand of Units B, C and D, respectively.

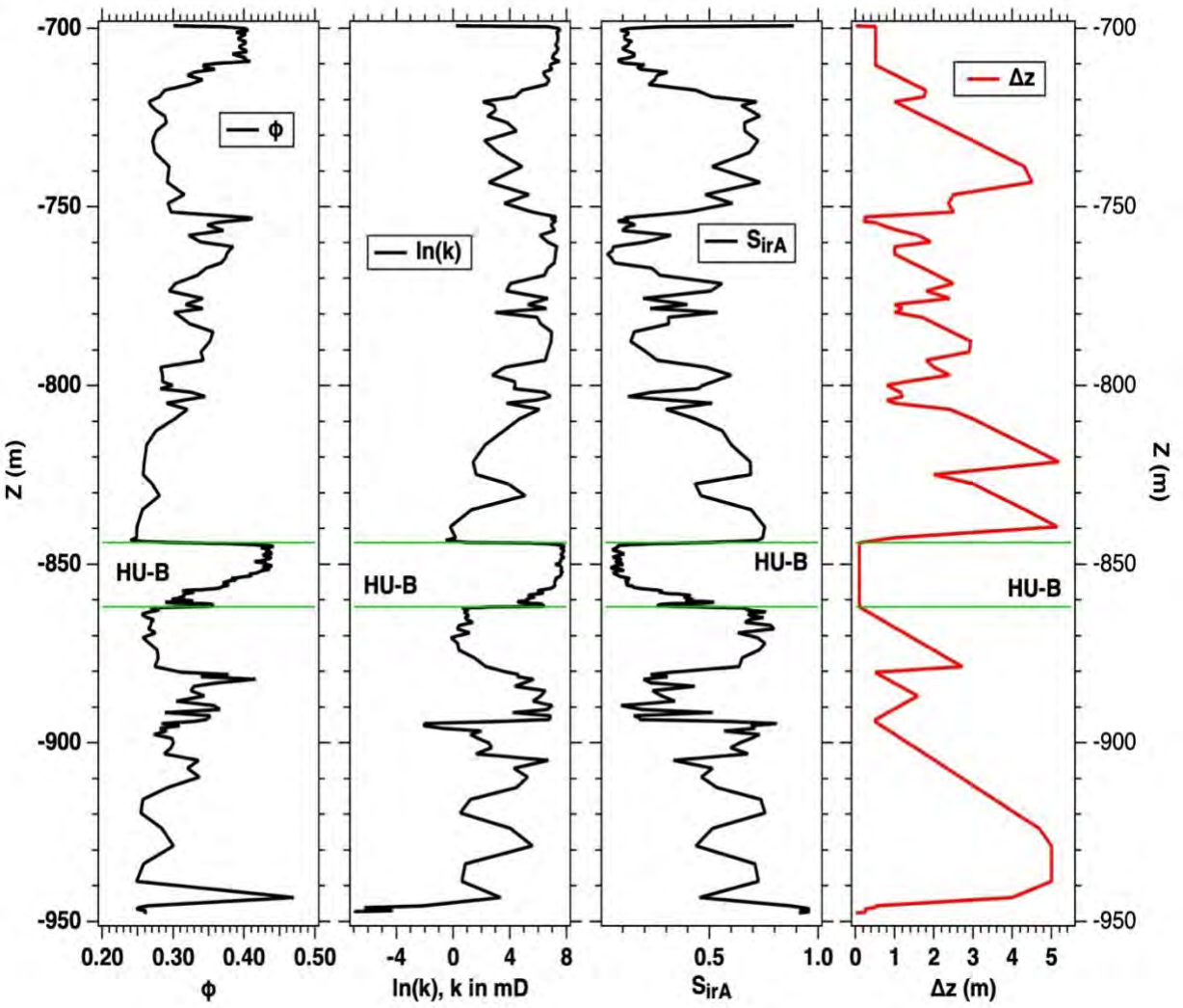

Fig. 2. Vertical variability in (a) the key flow properties ϕ, k and S_{irA} (1st, 2nd and 3rd panels, respectively, beginning from the left) and (b) in the discretization of Δz (last panel on the right) in the profile of the simulated domain. The term "HU-B" denotes the hydrate-bearing layer of the B1 sand in Unit B (see Figure 1).

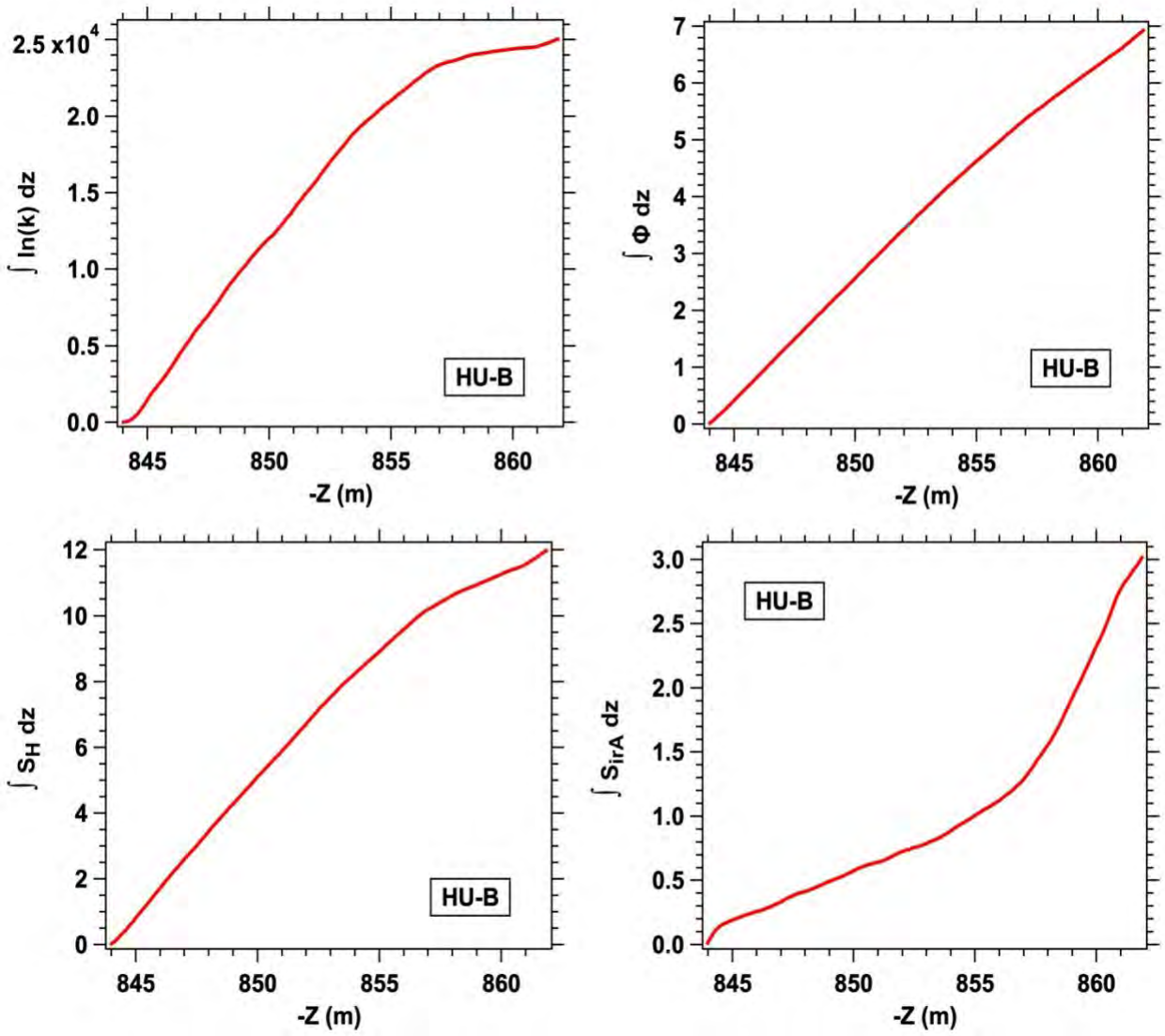

Fig. 3. Numerical integration of key properties and conditions, used for accurate assignment to the Δz subdivisions of the discretized domain in layer HU-B: the hydrate-bearing layer of the B1 sand in Unit B (see Figure 1).

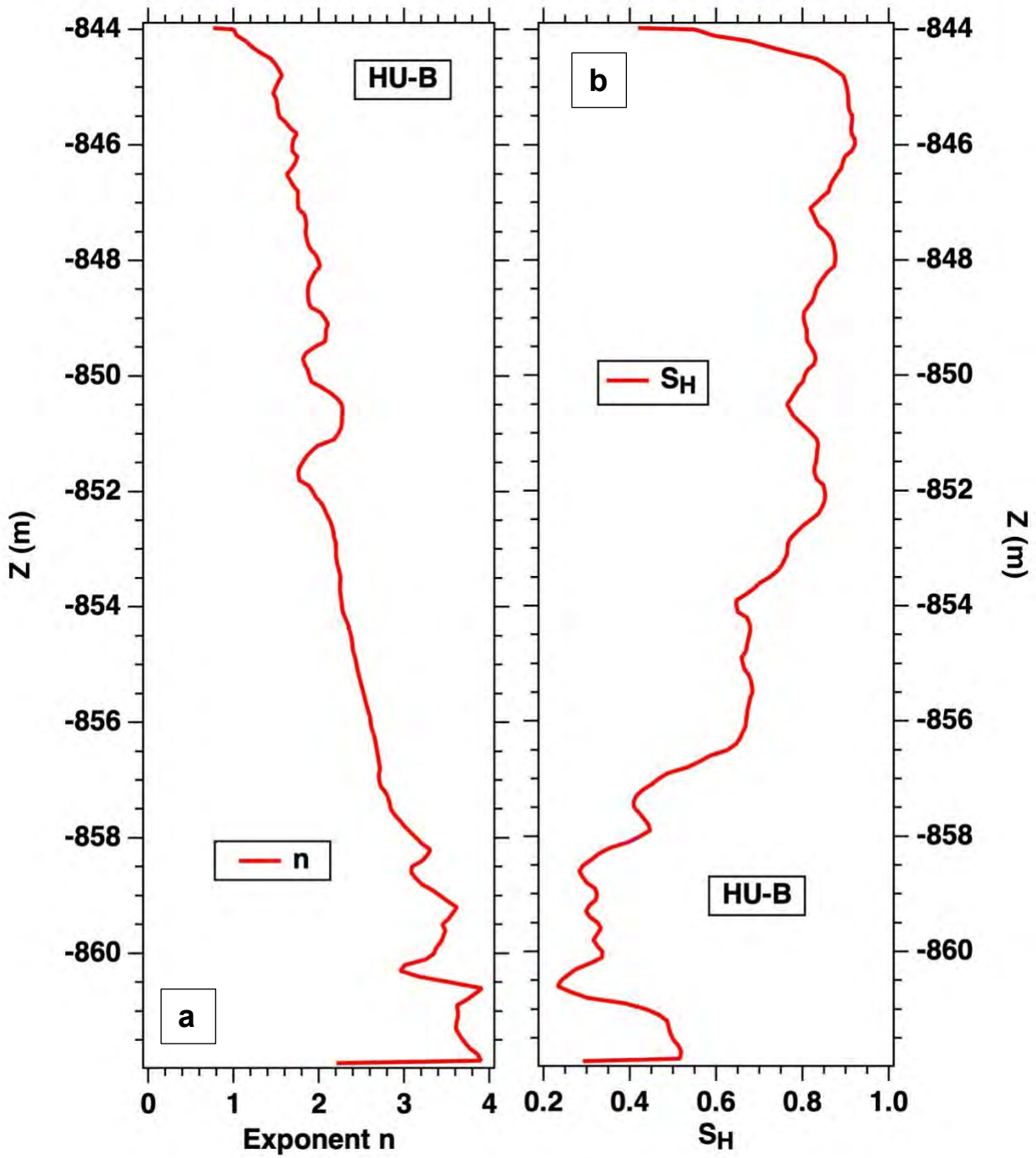

Fig. 4. Vertical variability in (a) the n-exponent of the relative permeability equations (see Table 1) and (b) in the initial hydrate saturation S_H in the profile of layer HU-B (the hydrate-bearing layer of the B1 sand in Unit B, see Figure 1) of the simulated domain.

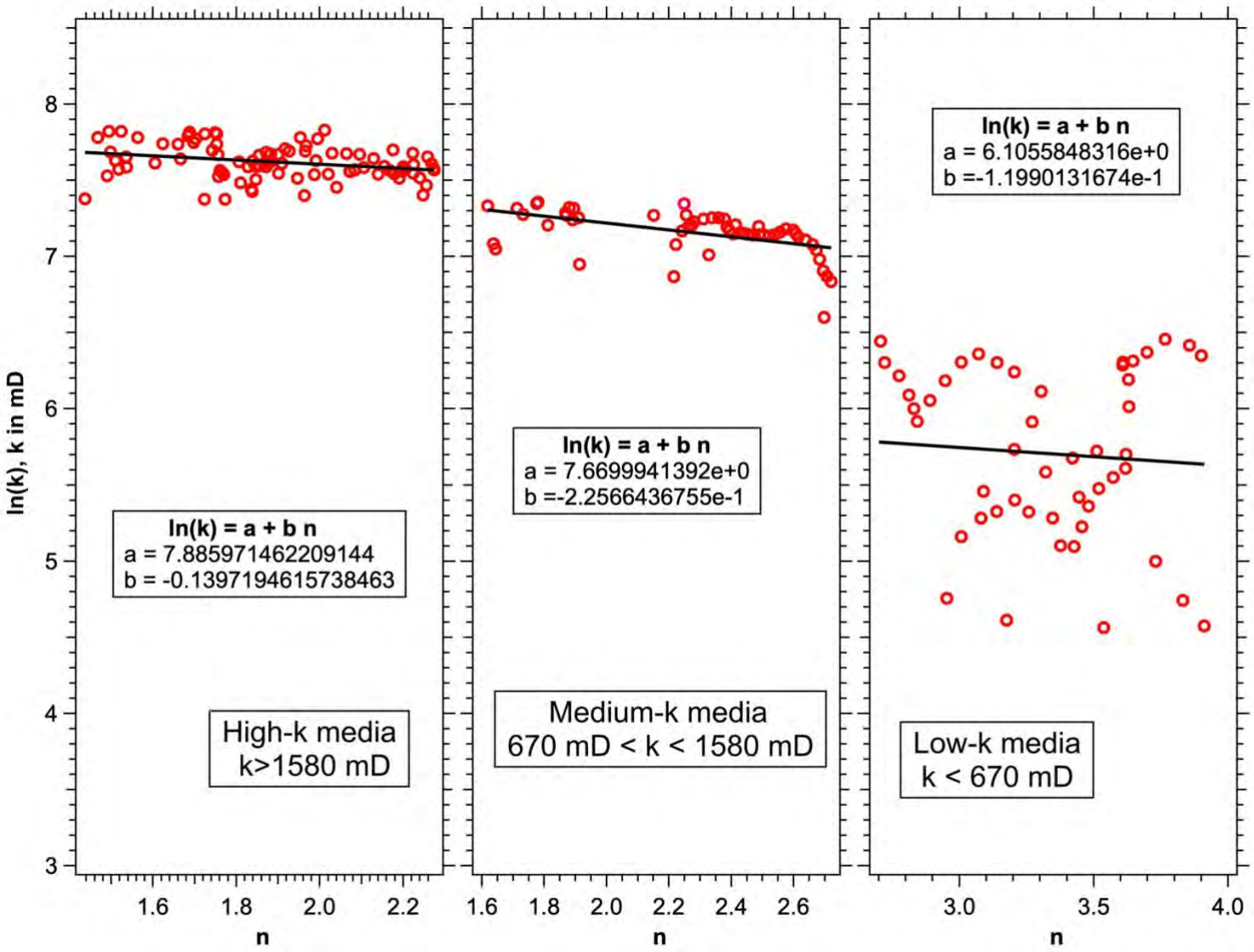

Fig. 5. Relationship for the determination of the *n* exponent in the hydrate-bearing layers from its relationship to ln(*k*).

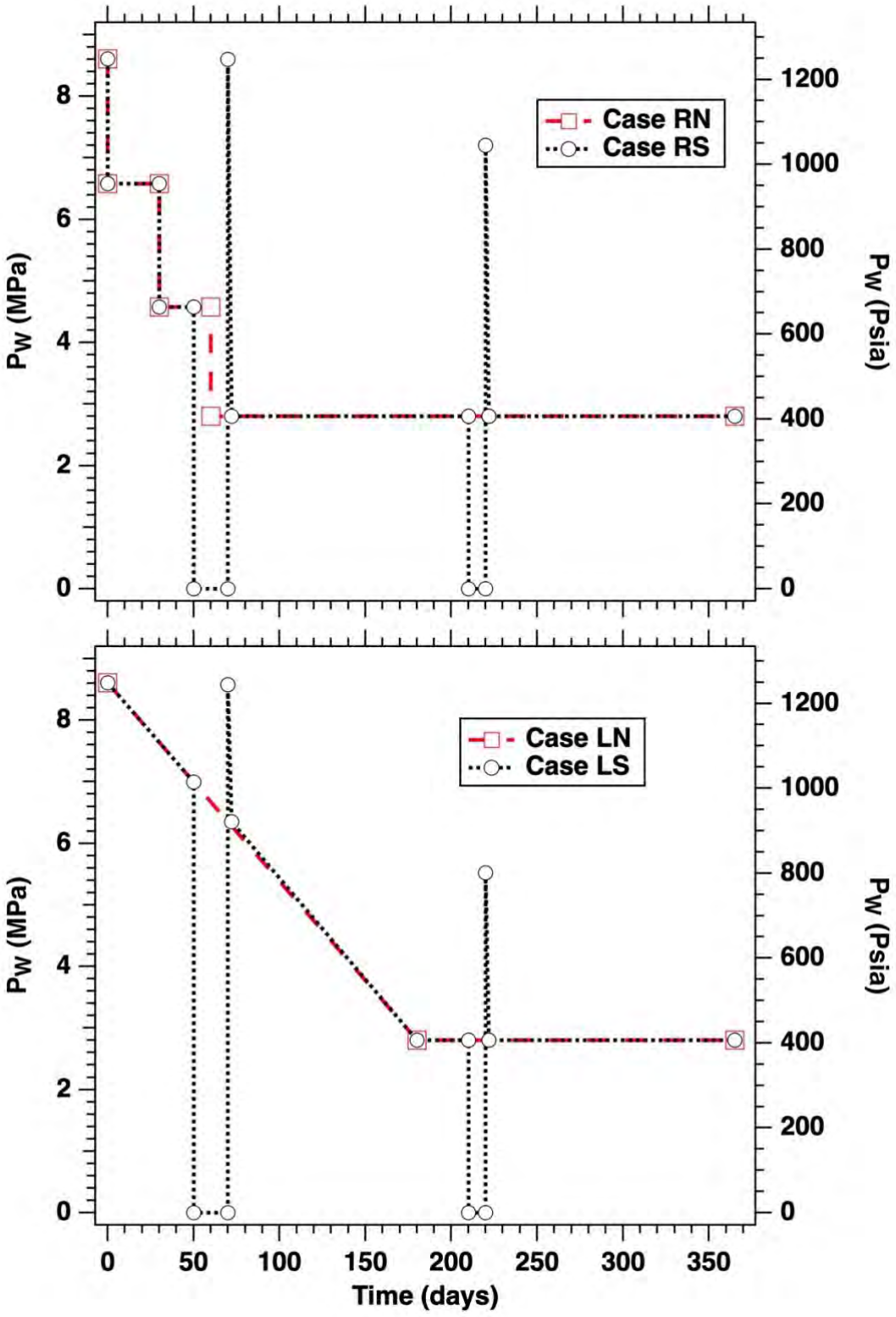

Fig. 6. P_W schedules and shut-ins in Cases RN, RS, LN and LS. Note that Pw = 2.8 MPa remains constant in all these cases for t > 220 days.

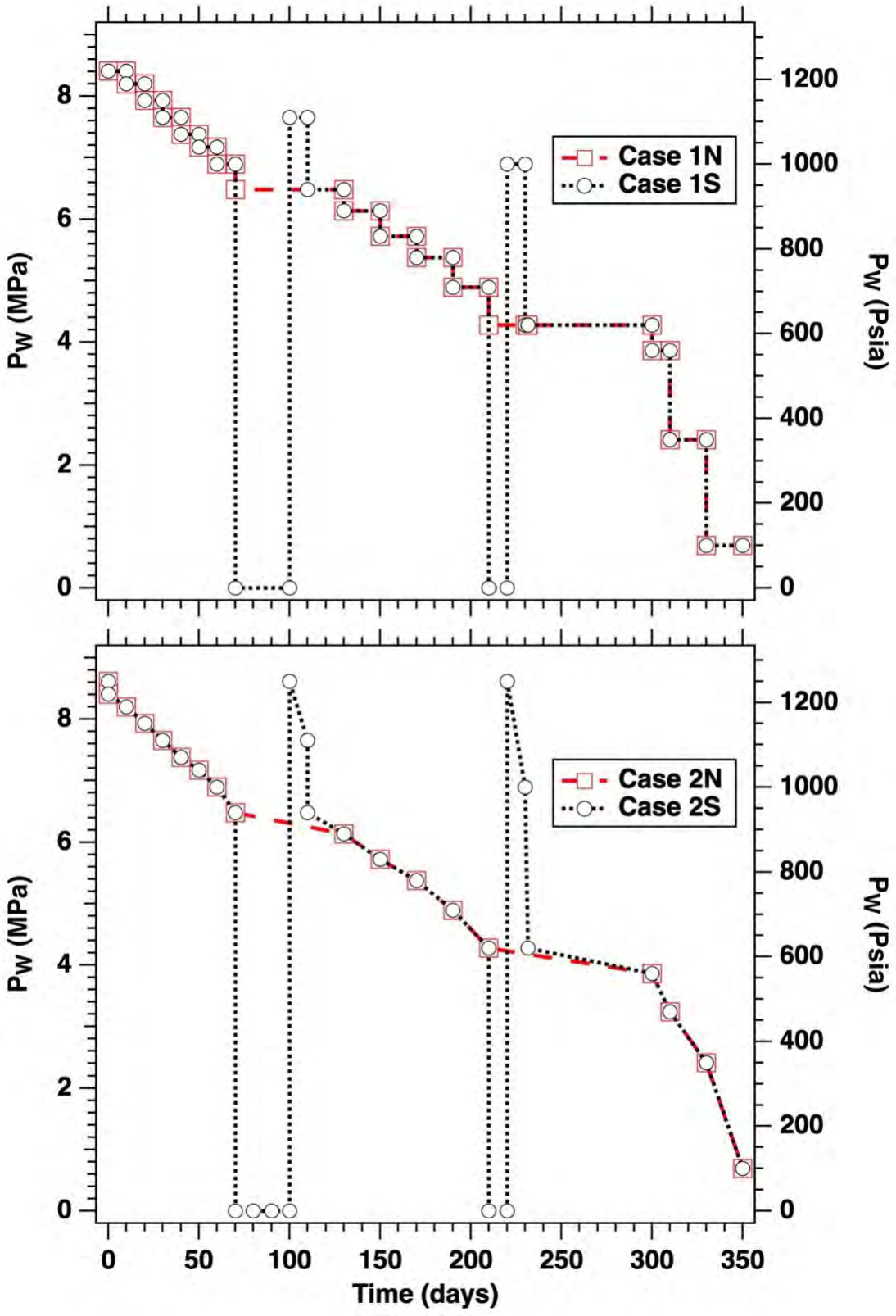

Fig. 7. *Pw* schedules and shut-ins in Cases 1N, 1S, 2N and 2S.

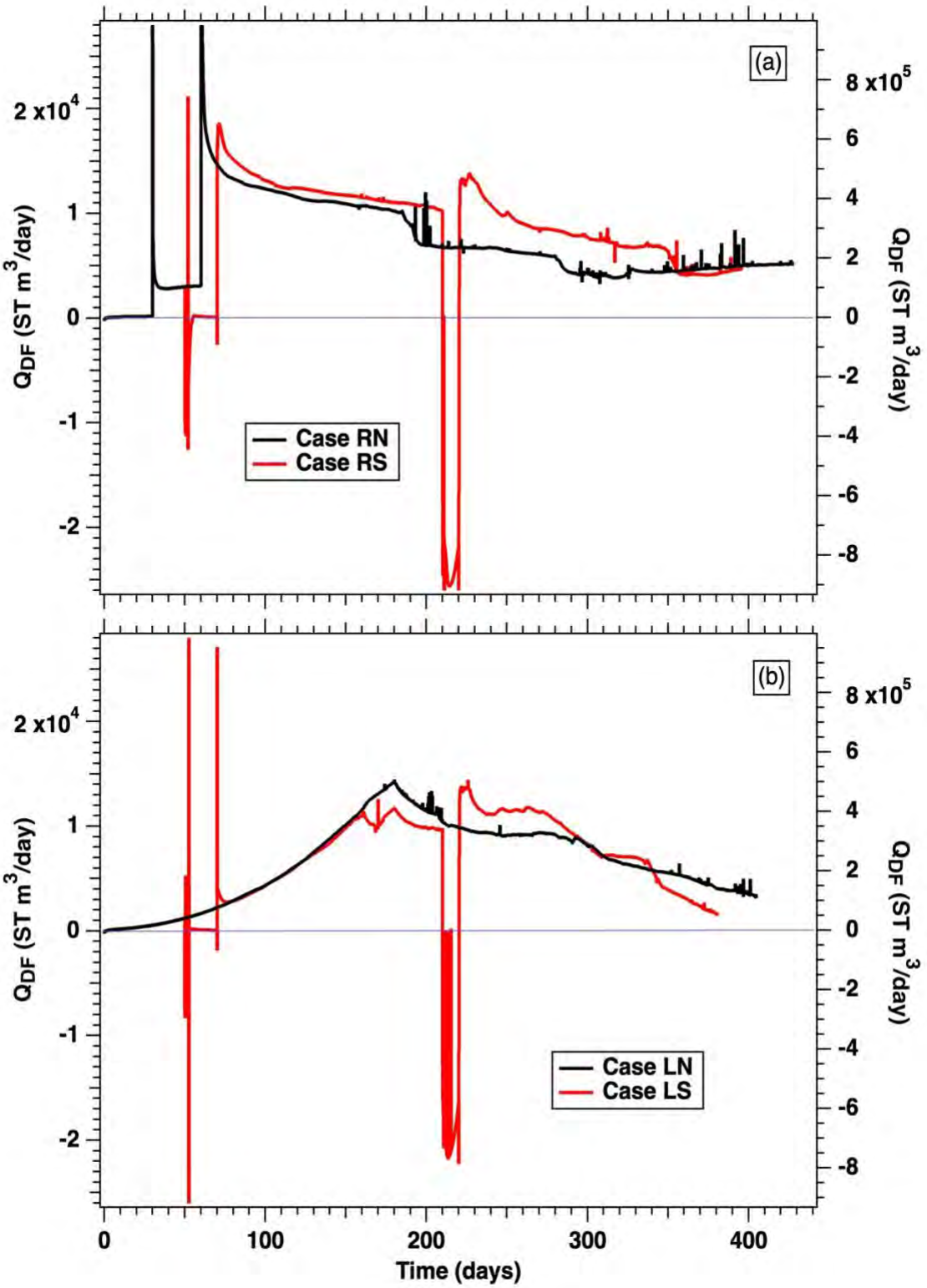

Fig. 8. Evolution of the rate of hydrate dissociation/formation Q_{DF} in (a) Cases RN and RS and (b) Cases LN and LS. The scales are the same in both figures for easy comparison.

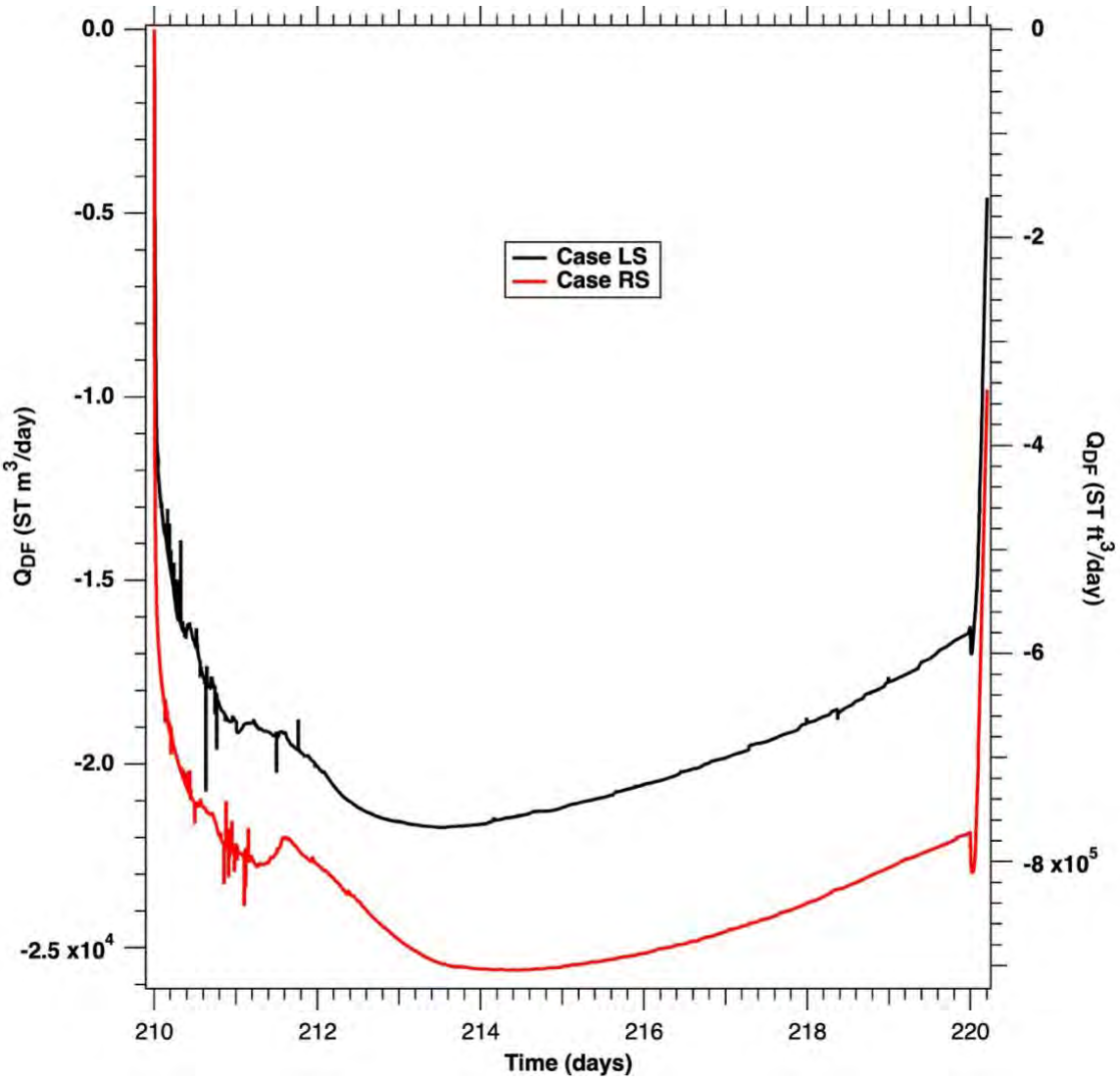

Fig. 9. Detail describing the rapid rate of hydrate reformation during the 2nd shut-in Cases RS and LS.

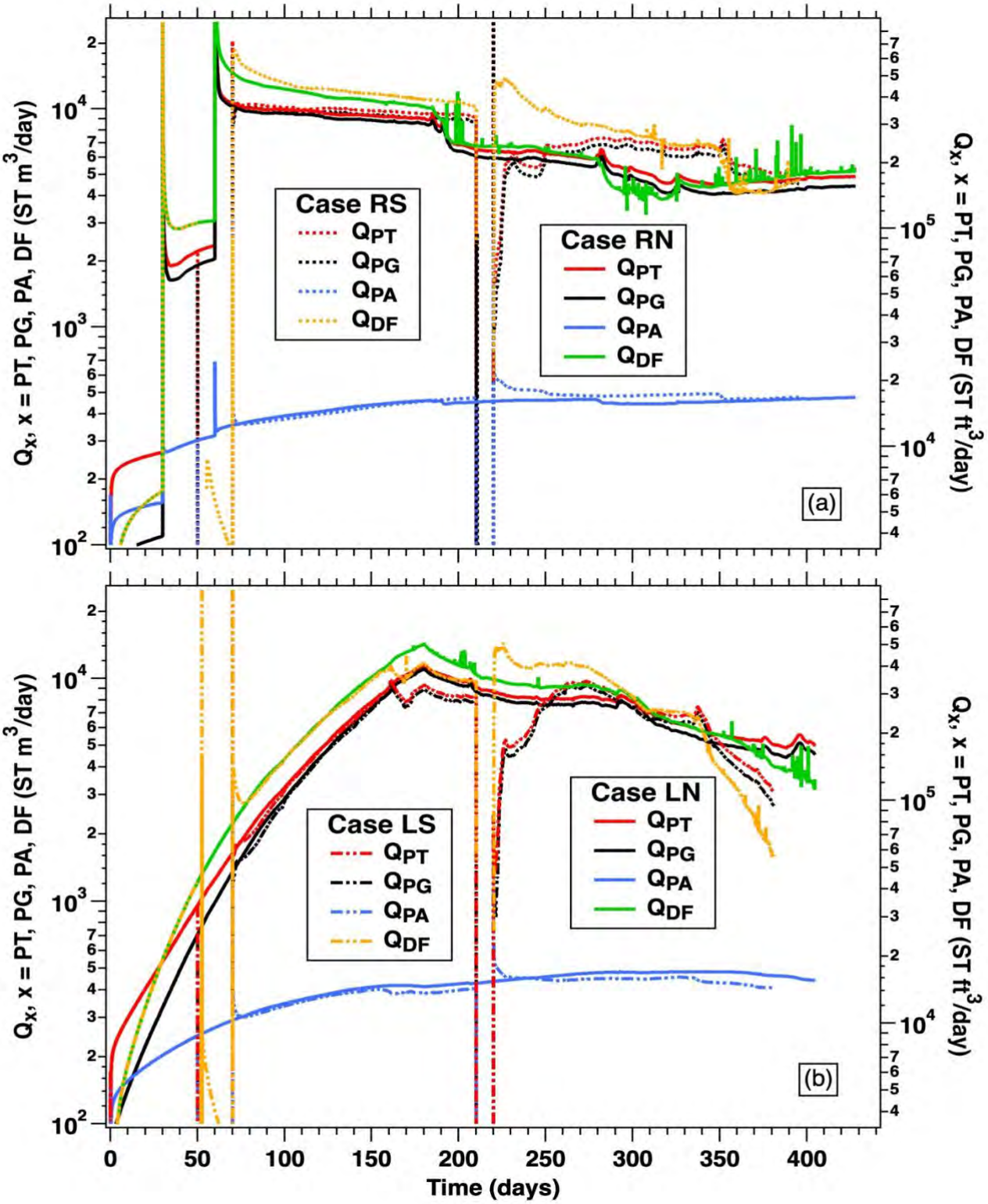

Fig. 10. Semi-log plot of the evolution of Q_{PT}, Q_{PG}, Q_{GA} and Q_{DF} in (a) Cases RN and RS and (b) Cases LN and LS during the entire duration of the production test. The scales are the same in both figures for easy comparison.

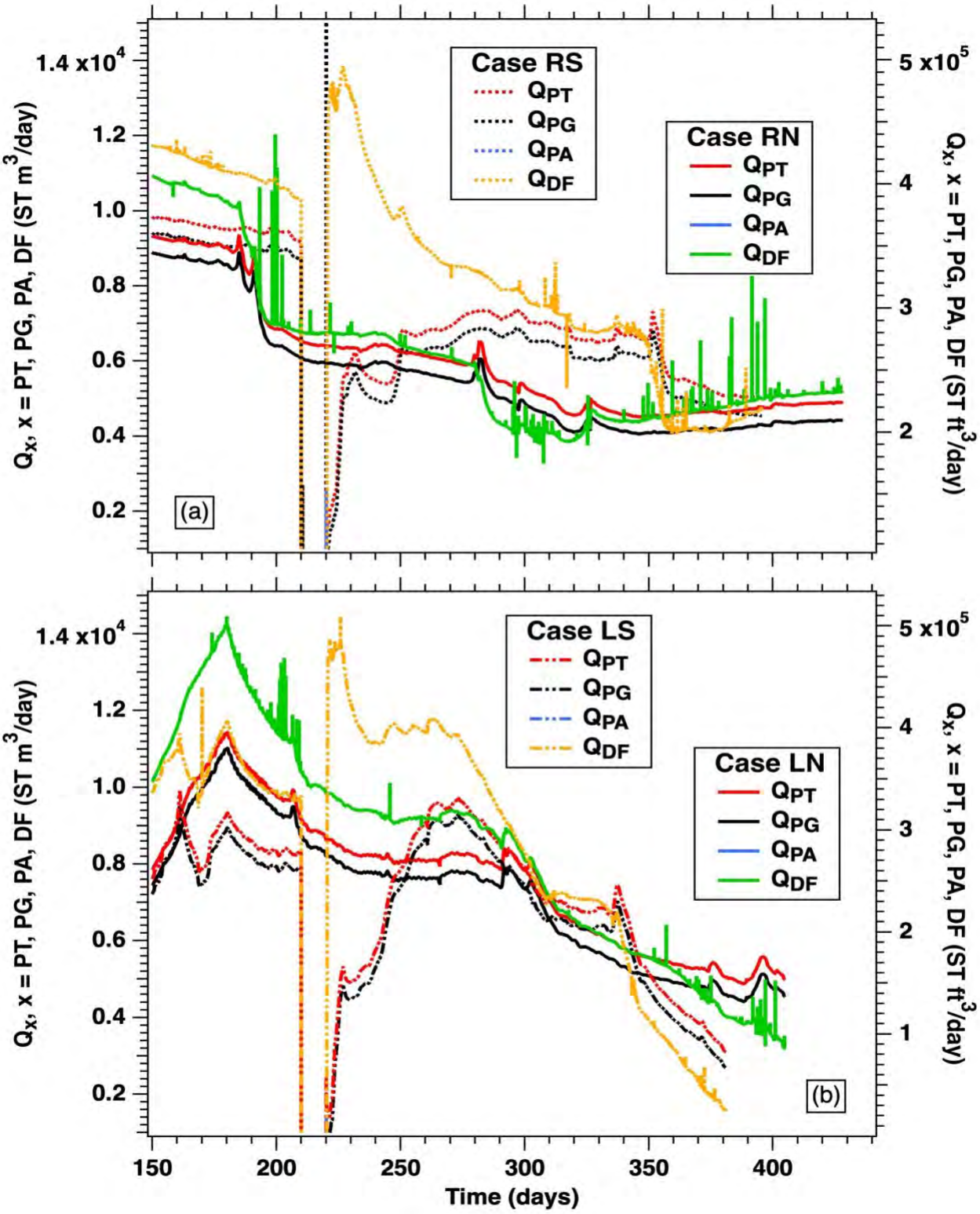

Fig. 11. Linear plot of the evolution of Q_{PT}, Q_{PG} and Q_{DF} in (a) Cases RN and RS and (b) Cases LN and LS for $t > 150$ days, clearly showing the rate differences between the cases with (S) and without (N) shut-ins. $Q_{PA} < 1000$ ST m^3/day in all cases and is not captured by the graph scale.

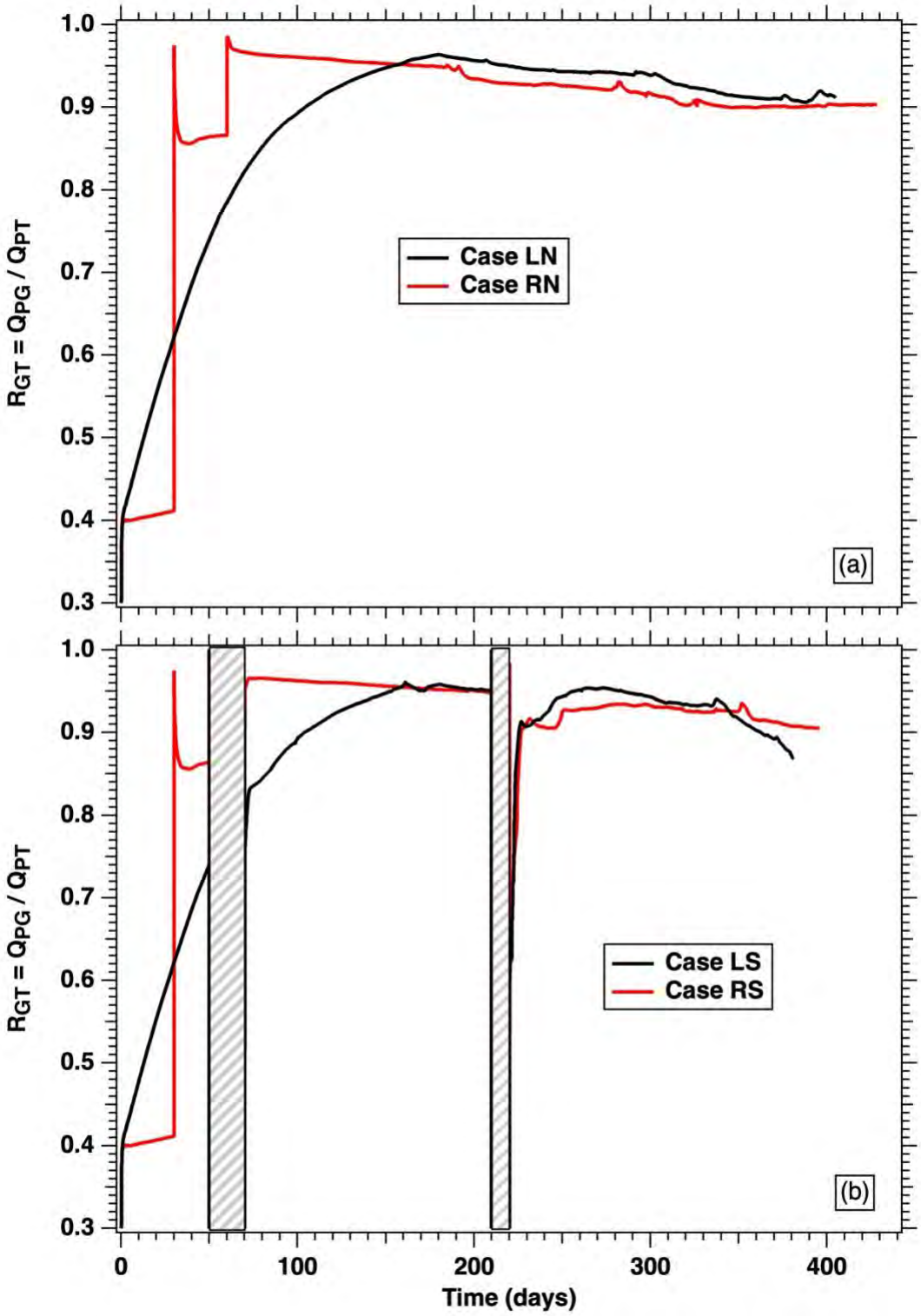

Fig. 12. Evolution of R_{GT} over time in (a) Cases RN and LN and (b) Cases RS and LS. Note that a R_{GT} >80% is attained from the early stages of production in all cases.

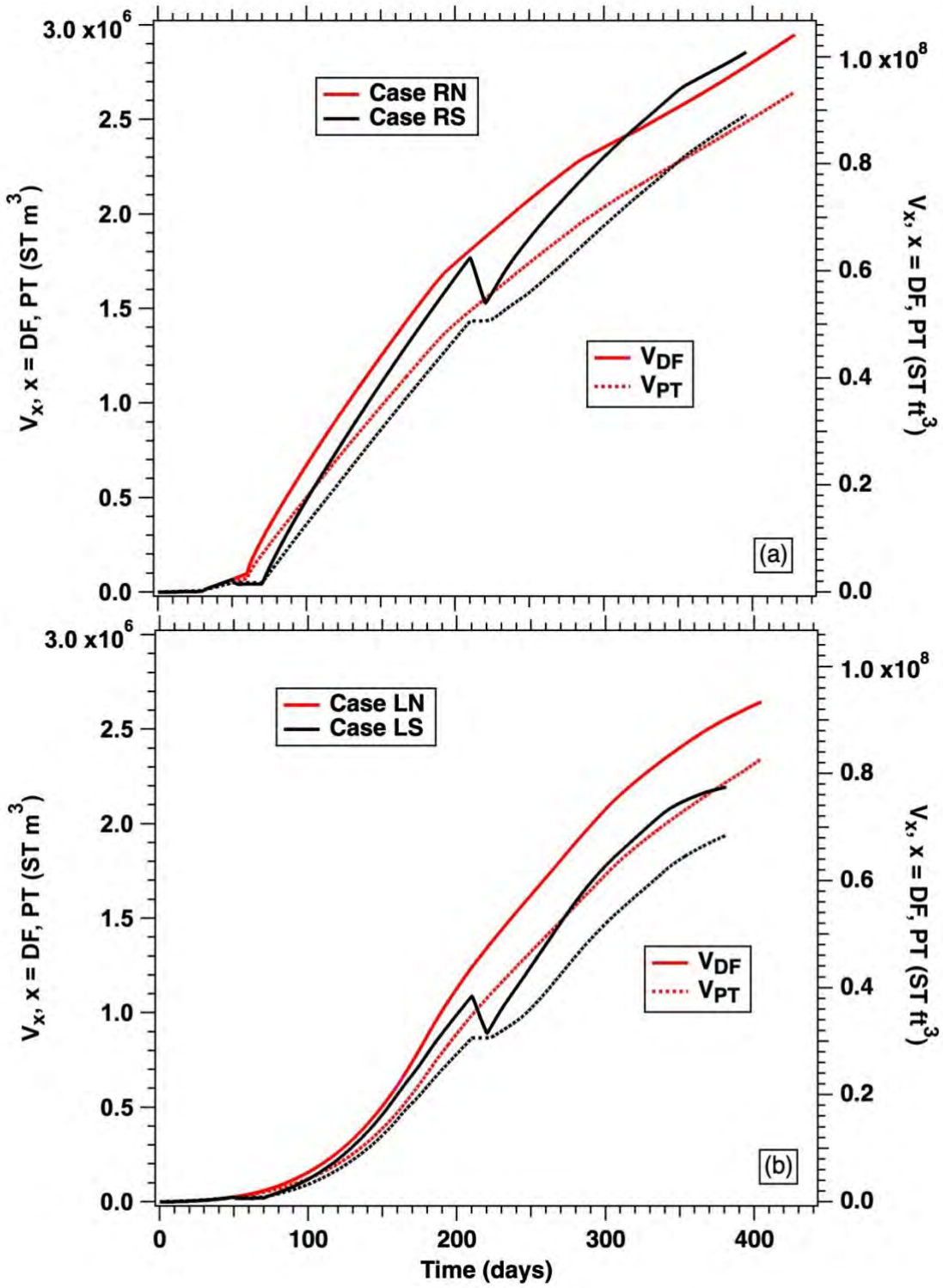

Fig. 13. Effect of shut-ins on V_{DF} and V_{PT} in (a) Cases RN and RS and (b) Cases LN and LS. While V_{DF} and V_{PT} in Case RS recover 110 days from the 2nd shut-in (after which time they exceeds those in Case RN), Case LS exhibits only a partial recovery that is associated with consistently lower V_{DF} and V_{PT} than those in Case LN.

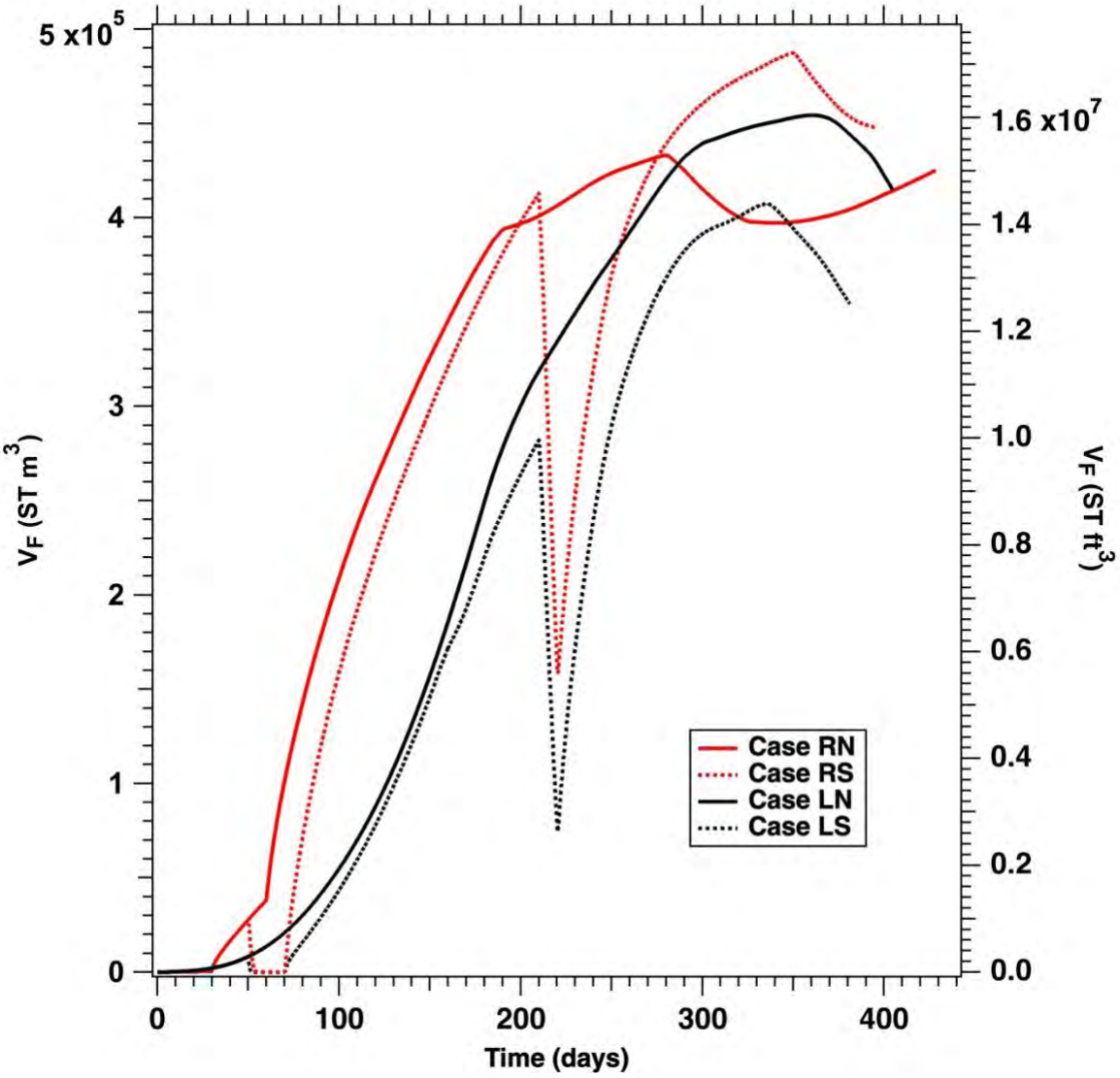

Fig. 14. Effect of shut-ins on the evolution of the volume of free gas V_F in the reservoir V_F in all cases. While V_F in Case RS recovers from the shut-ins after 55 days from the 2nd shut-in (and its V_F exceeds that in Case RN at later times), Case LS exhibits only a partial recovery that does not reach the V_F for Case LN.

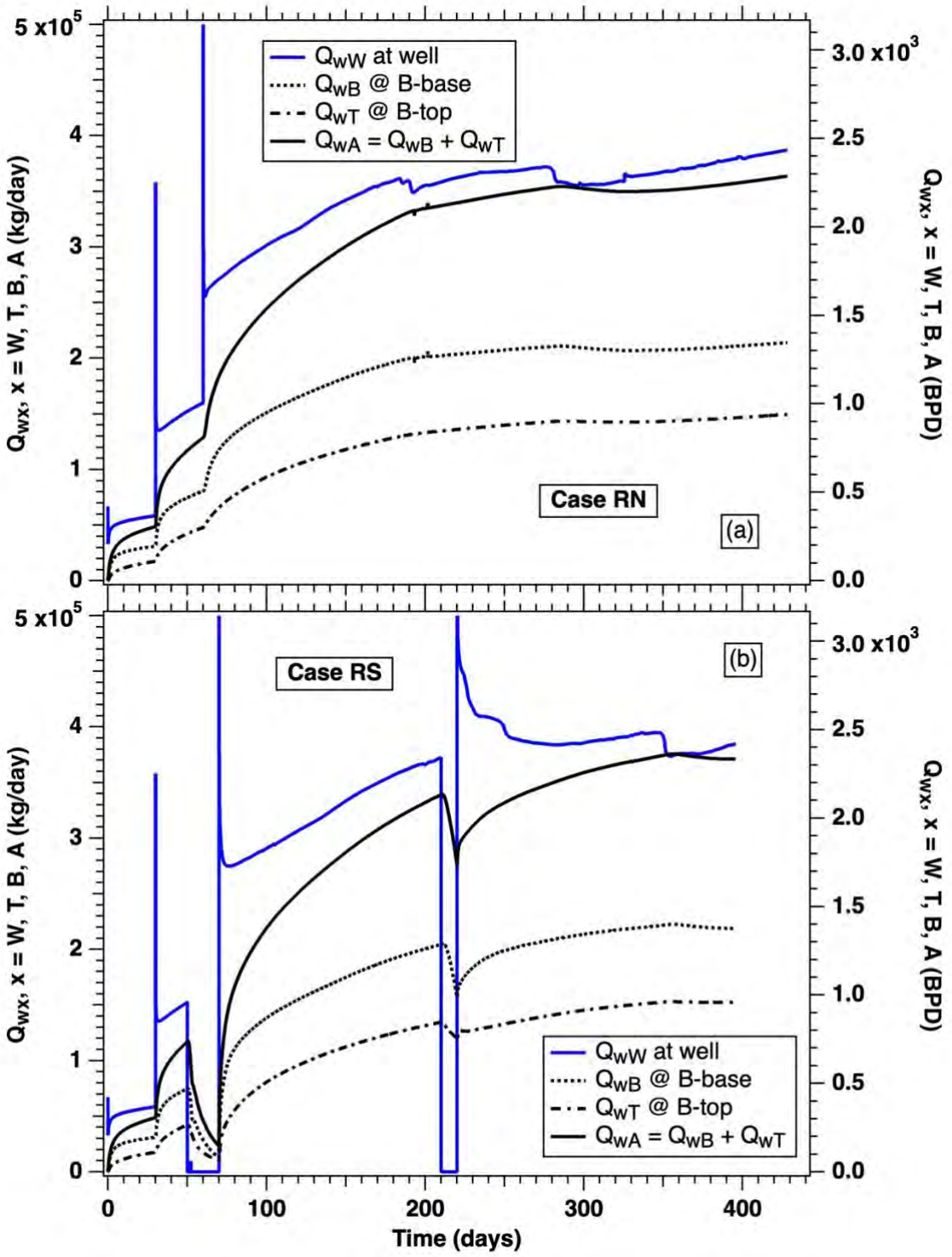

Fig. 15. Evolution of the rate of water production rate at the well Q_{wW} and of its replenishment by water inflows Q_{wT} and Q_{wB} through the top and bottom boundaries, respectively, in (a) Case RN and (b) Case RS. Note the proximity of Q_{wA} to Q_{wW} as time advances.

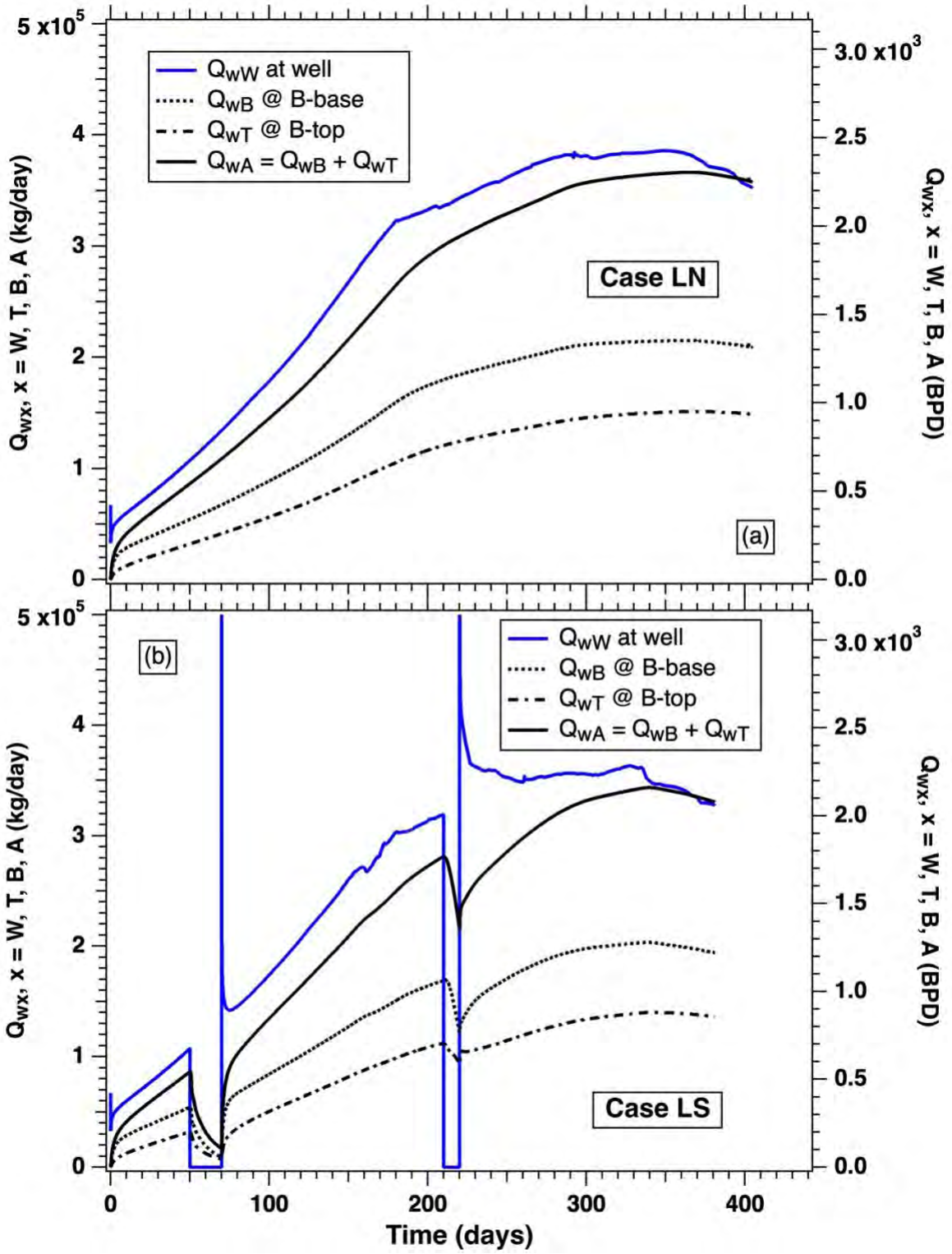

Fig. 16. Evolution of the rate of water production rate at the well Q_{wW} and of its replenishment by water inflows Q_{wT} and Q_{wB} through the top and bottom boundaries, respectively, in (a) Case LN and (b) Case LS. Note the proximity of Q_{wA} to Q_{wW} as time advances.

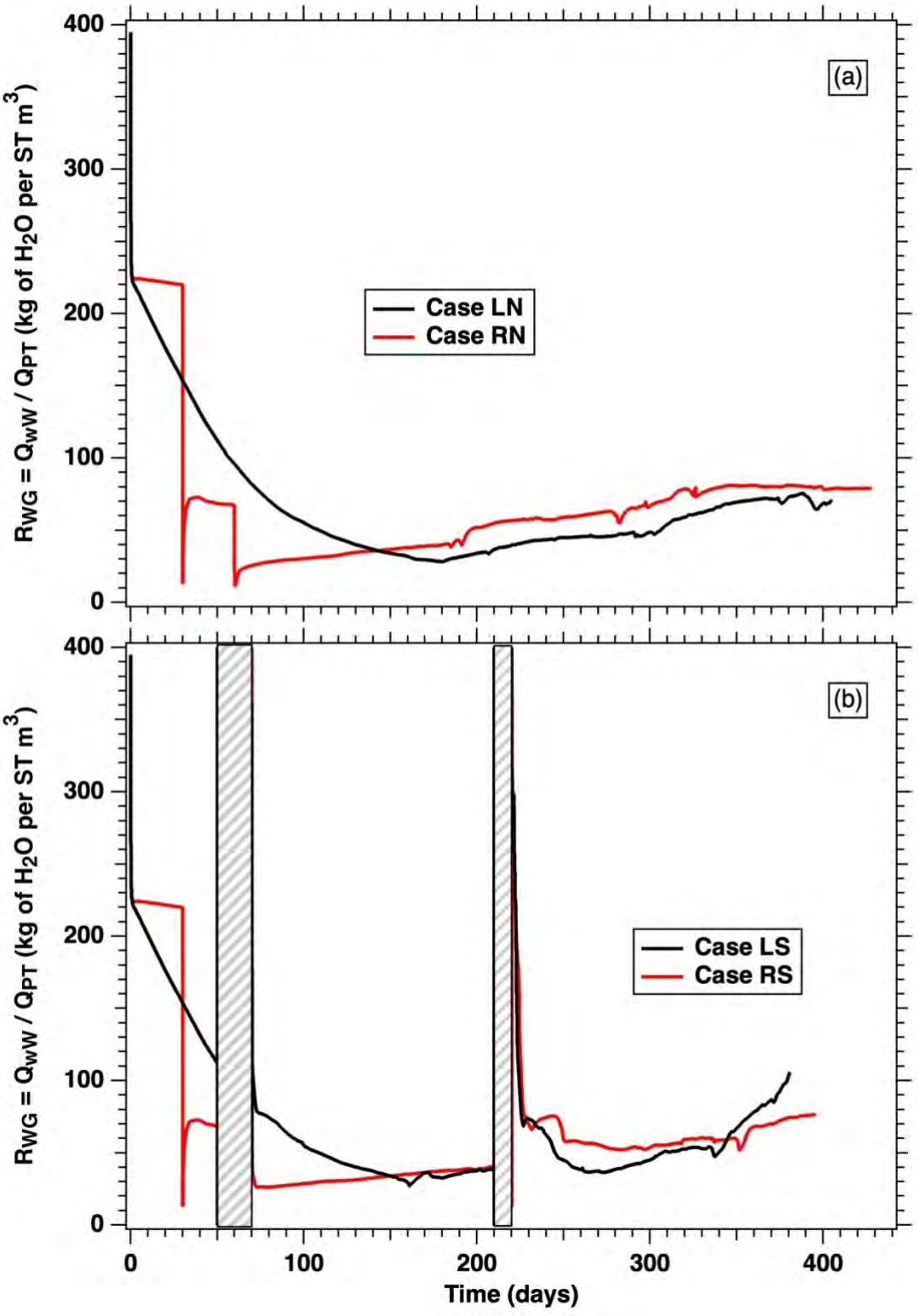

Fig. 17. Evolution of the water-to-gas ratio R_{WG} in (a) Cases RN and LN and (b) Cases RS and LS. Note the upward trend after a relatively early minimum is attained.

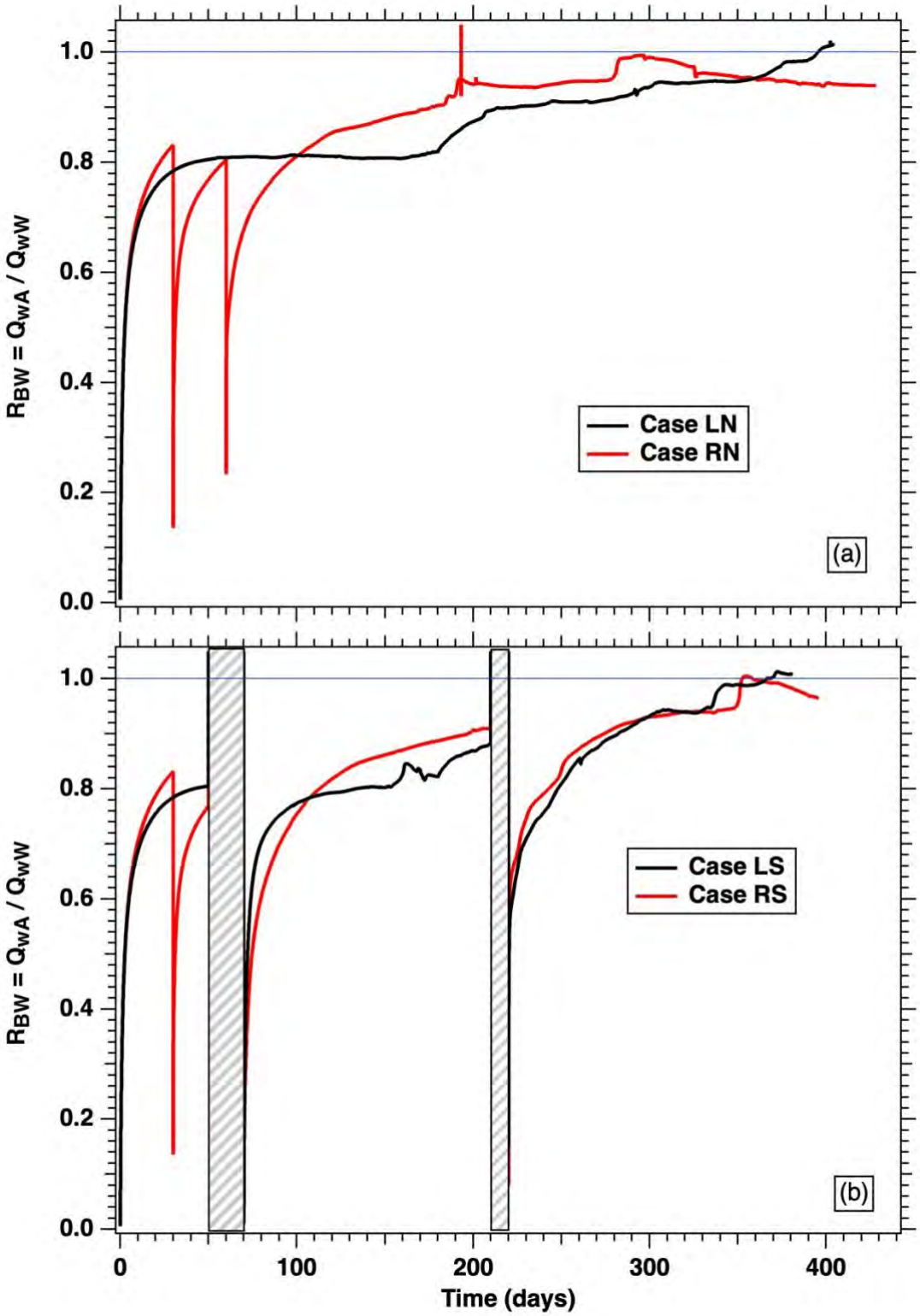

Fig. 18. Evolution of the water replenishment ratio R_{BW} in (a) Cases RN and LN and (b) Cases RS and LS. Note that after a short time from the onset of production, R_{BW} reaches and exceeds consistently the 80% level.

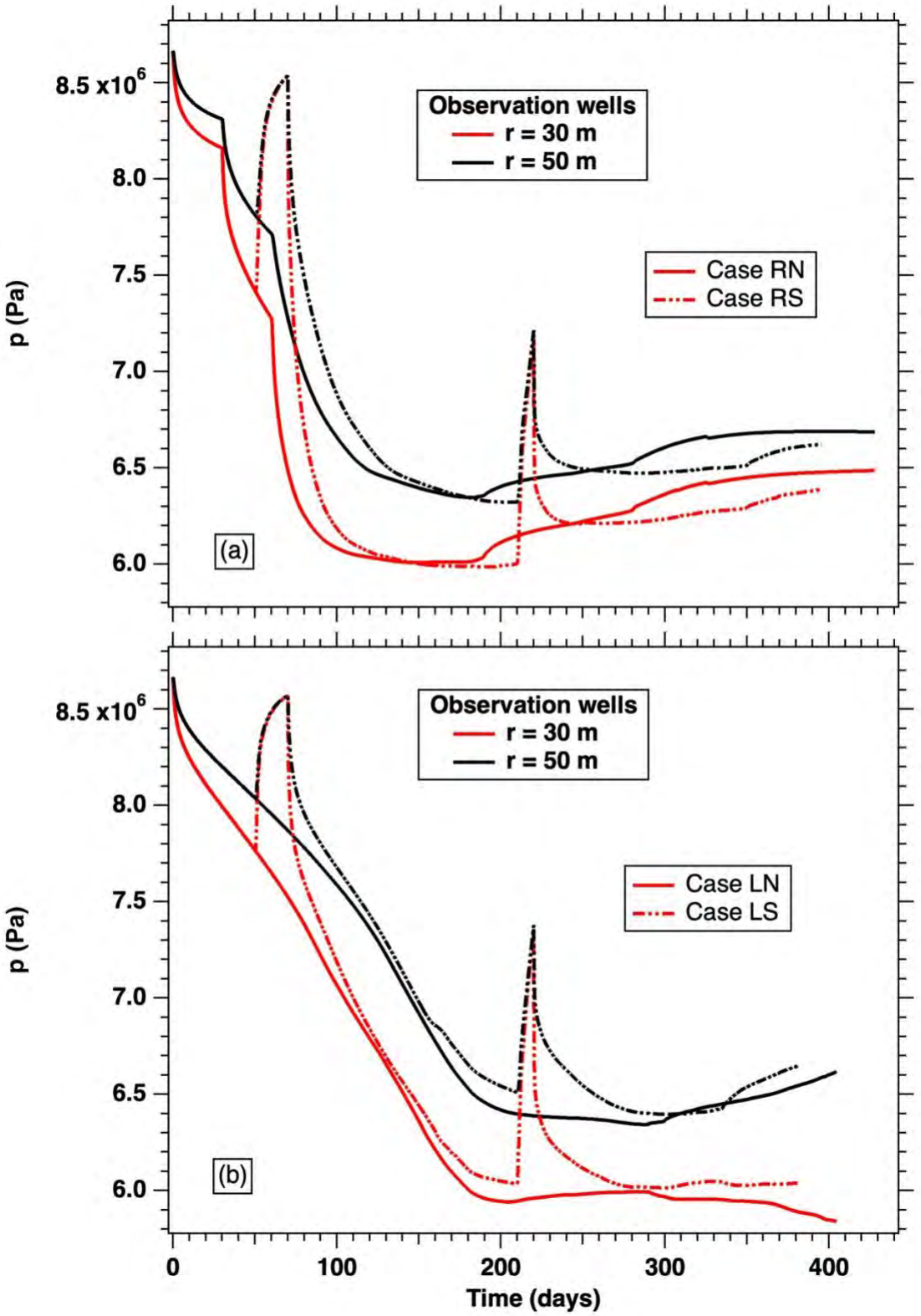

Fig. 19. Evolution of the pressure p at the observation wells during the production test in (a) Cases RN and RS and (b) Cases LN and LS

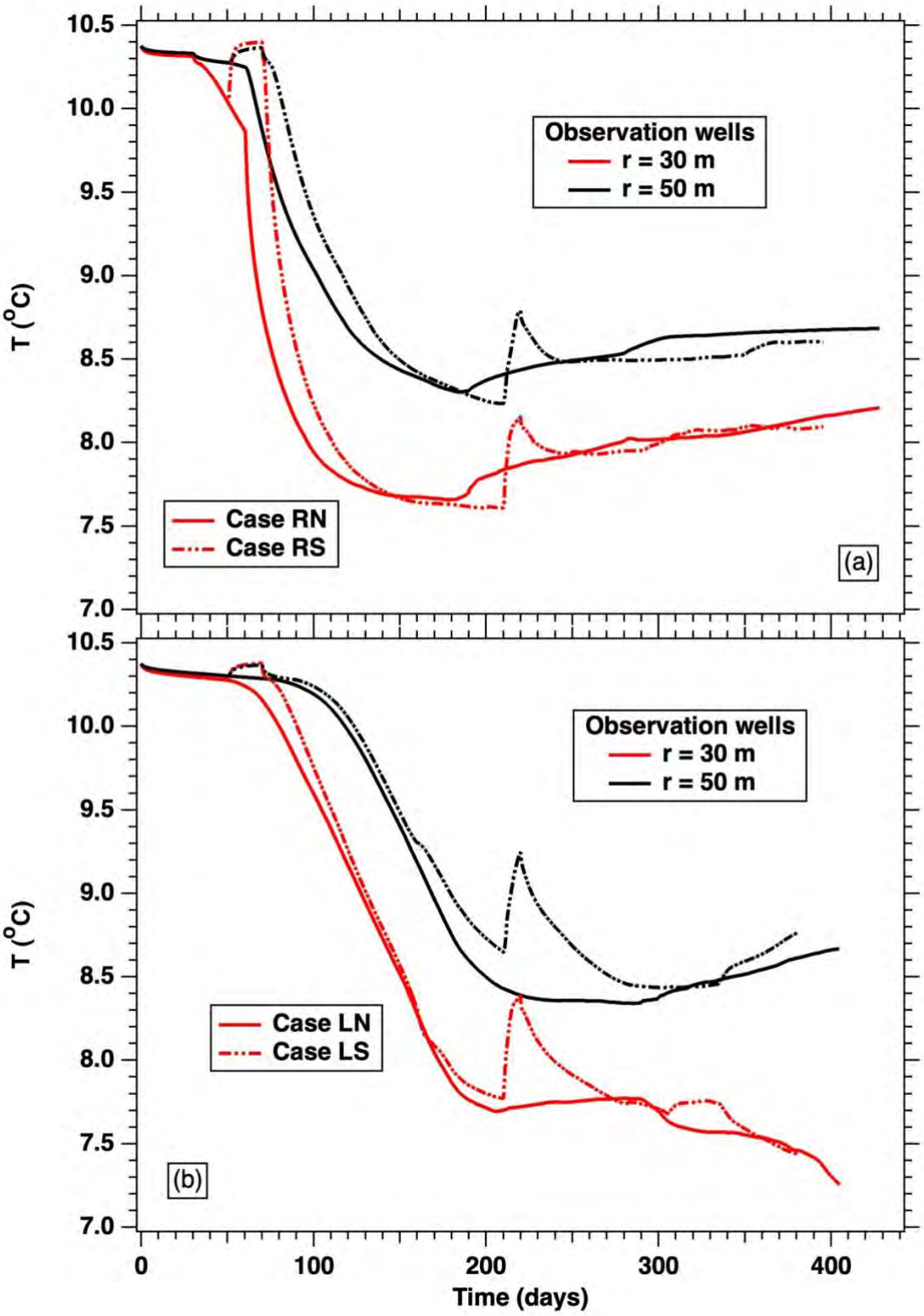

Fig. 20. Evolution of the temperature T at the observation wells during the production test in (a) Cases RN and RS and (b) Cases LN and LS.

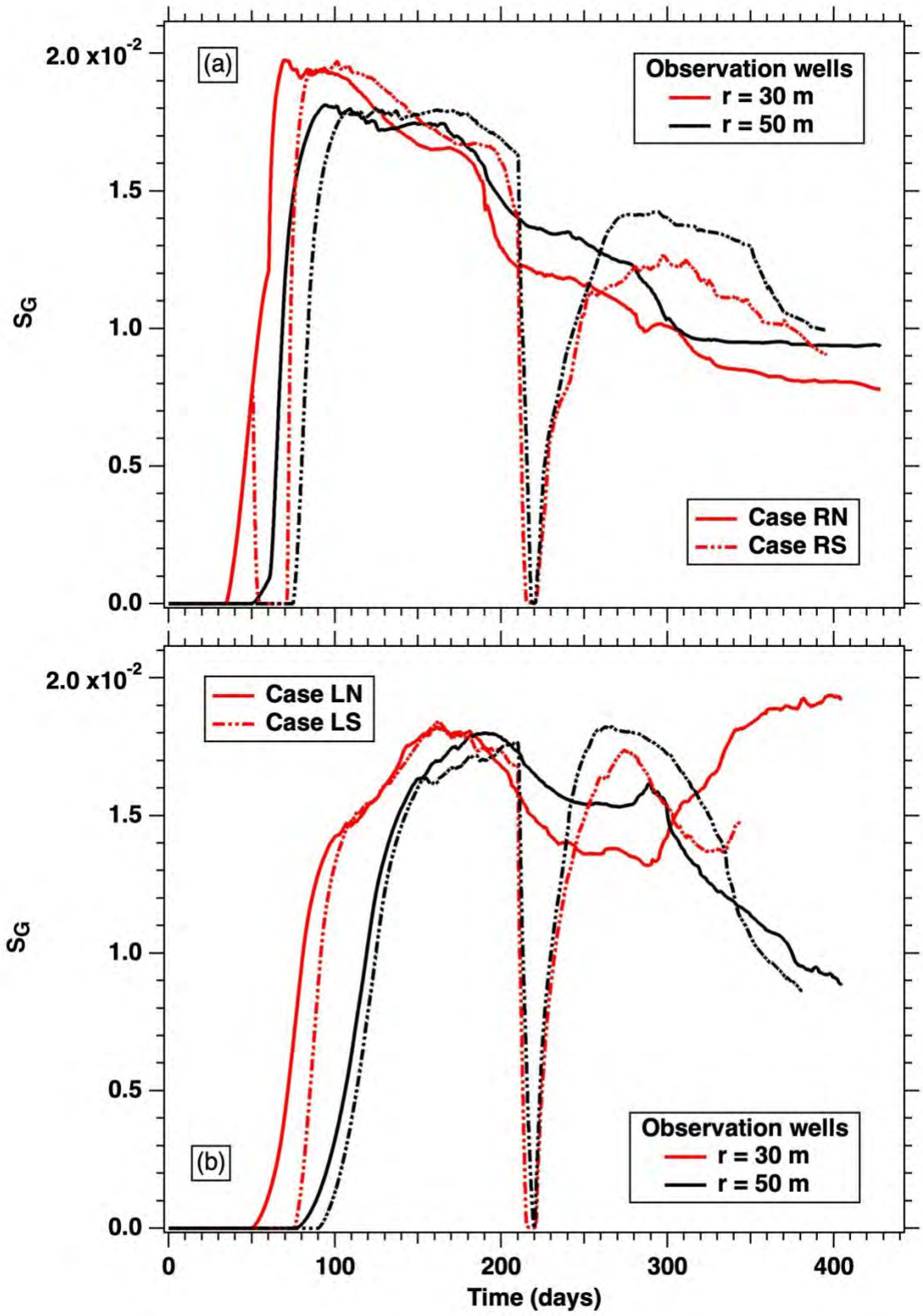

Fig. 21. Evolution of the pore-volume averaged gas hydrate saturation S_G at the observation wells during the production test in (a) Cases RN and RS and (b) Cases LN and LS.

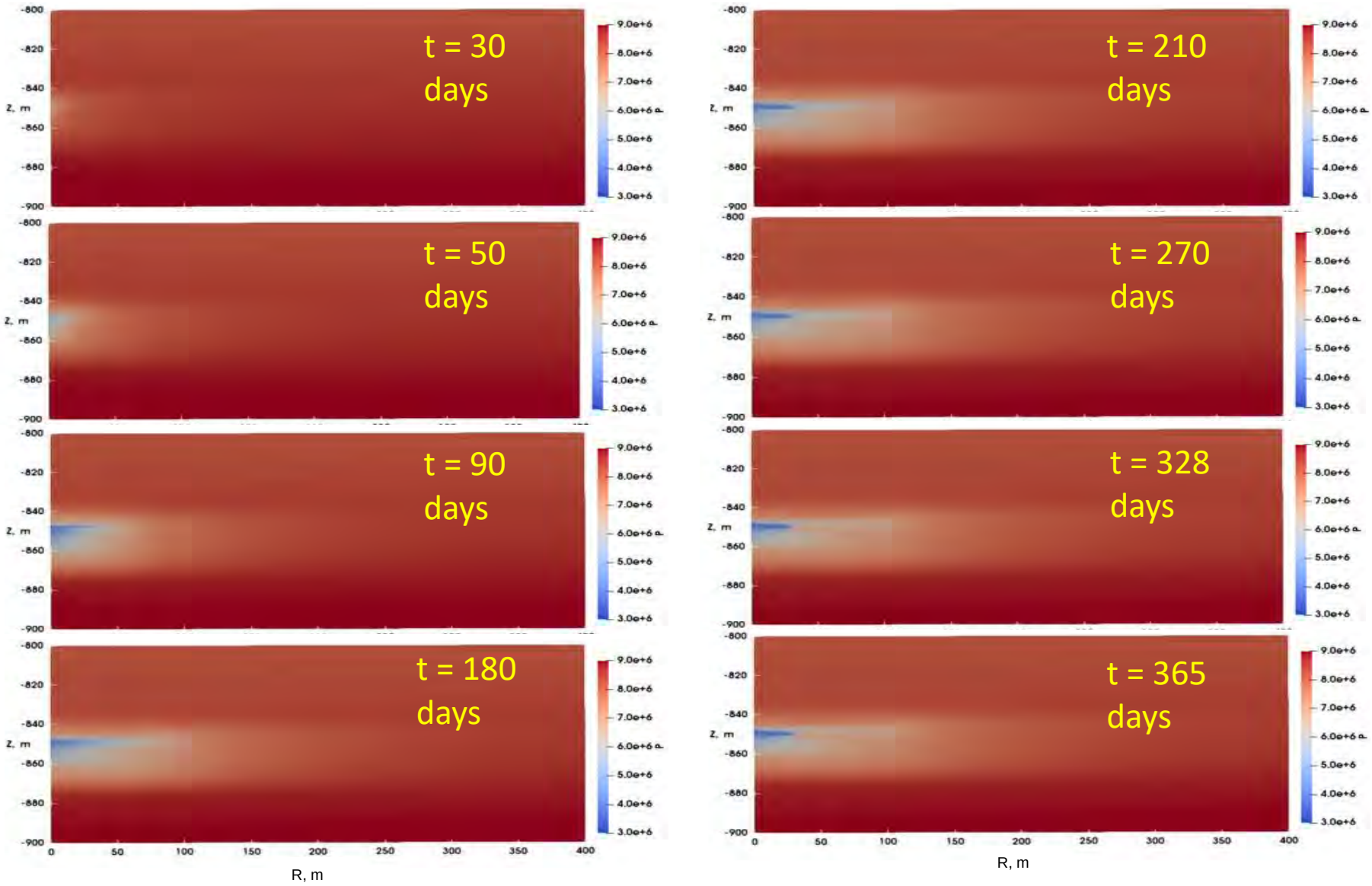

Figure 22: Case RN: Evolution of the *P*-spatial distribution in Unit B over time

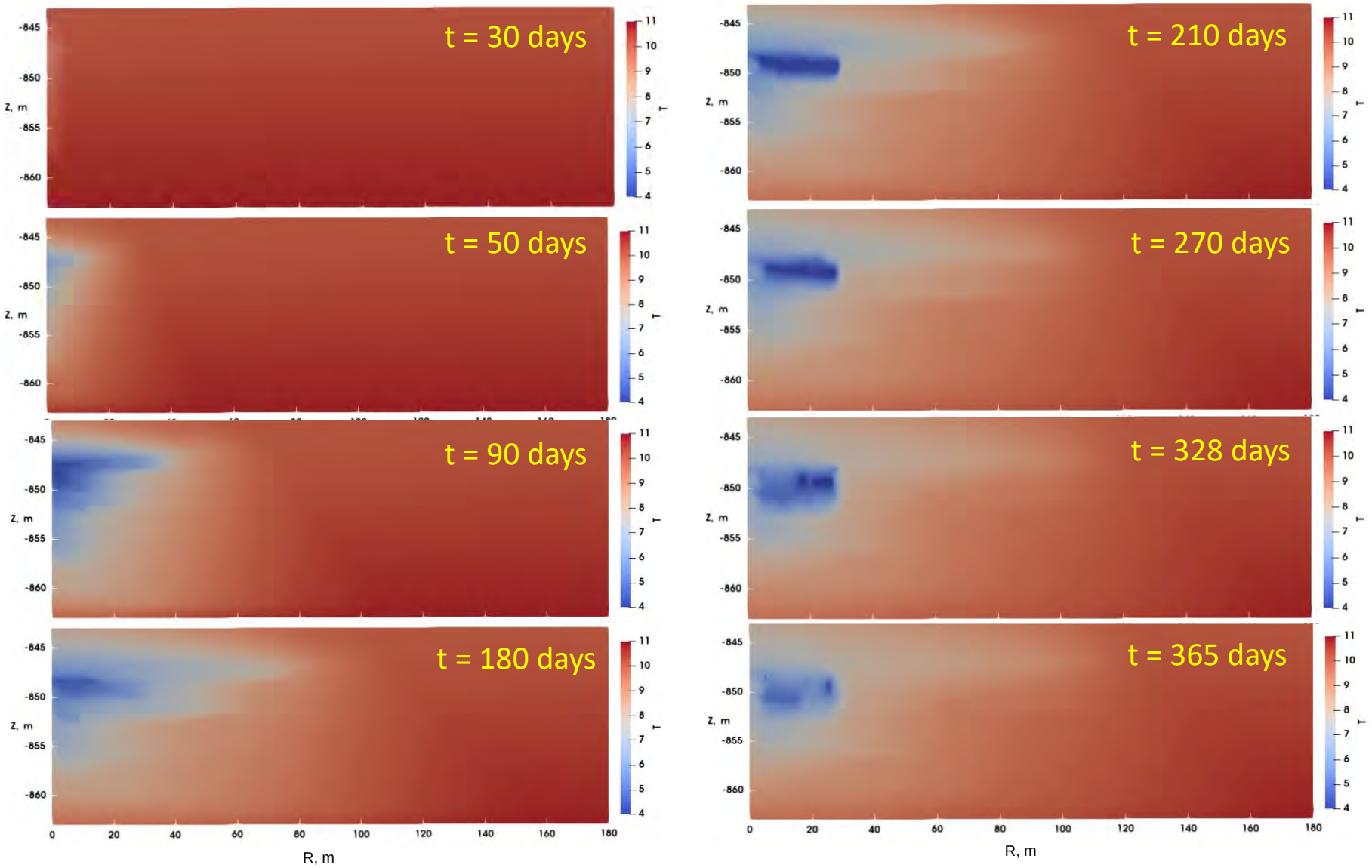

Figure 23: Case RN: Evolution of the *T*-spatial distribution in Unit B over time

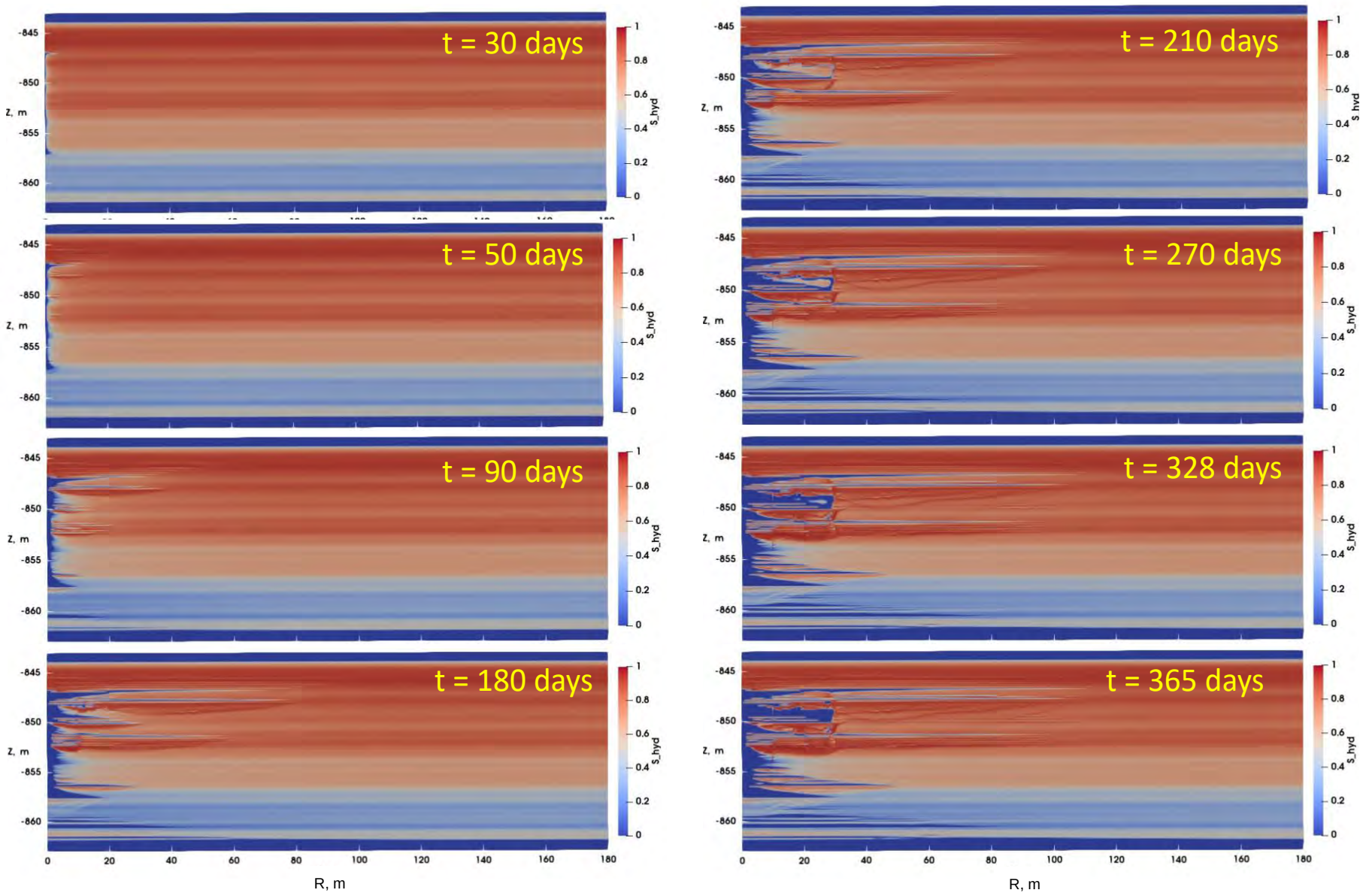

Figure 24: Case RN: Evolution of the S_H-spatial distribution in Unit B over time

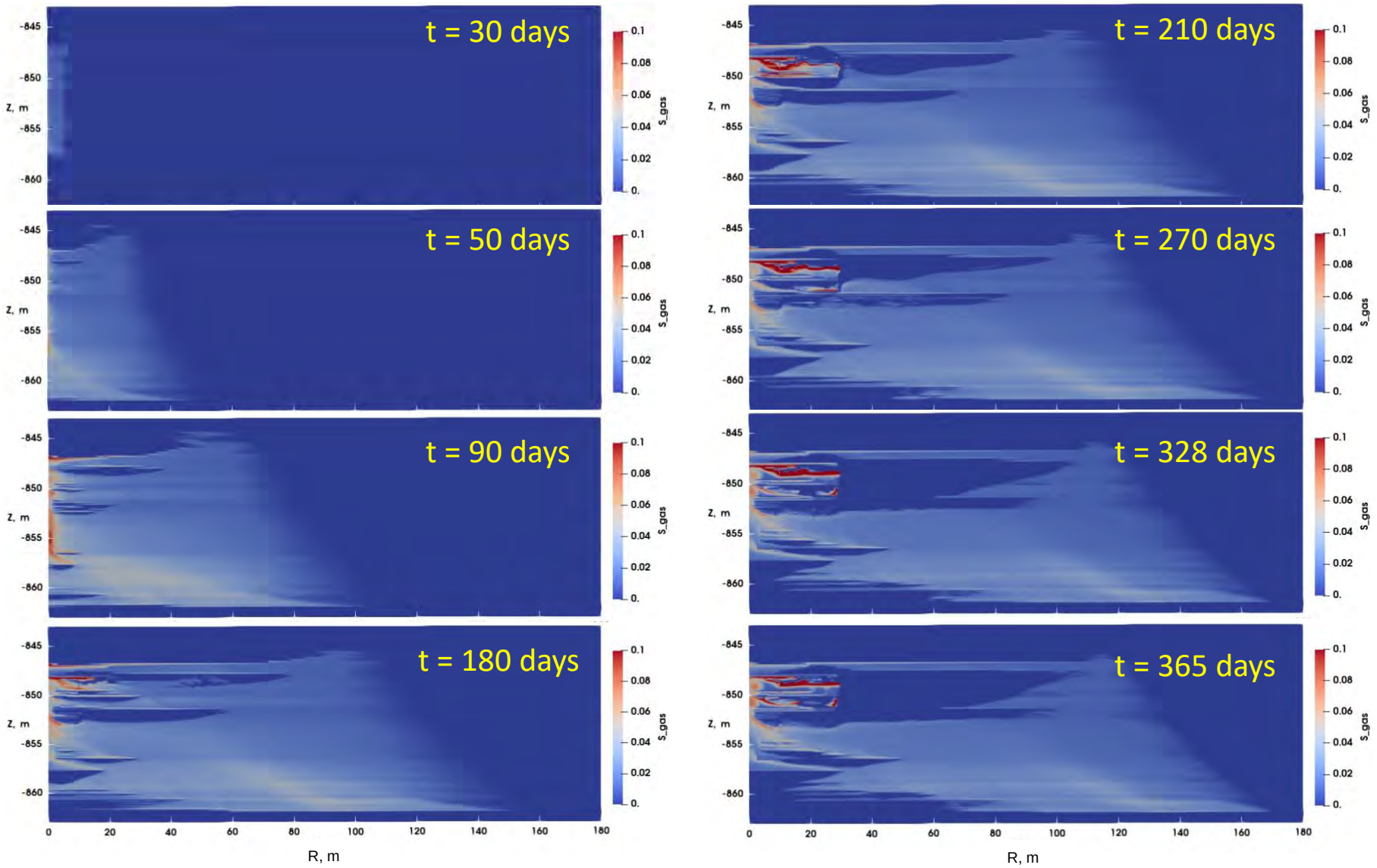

Figure 25: Case RN: Evolution of the S_G-spatial distribution in Unit B over time

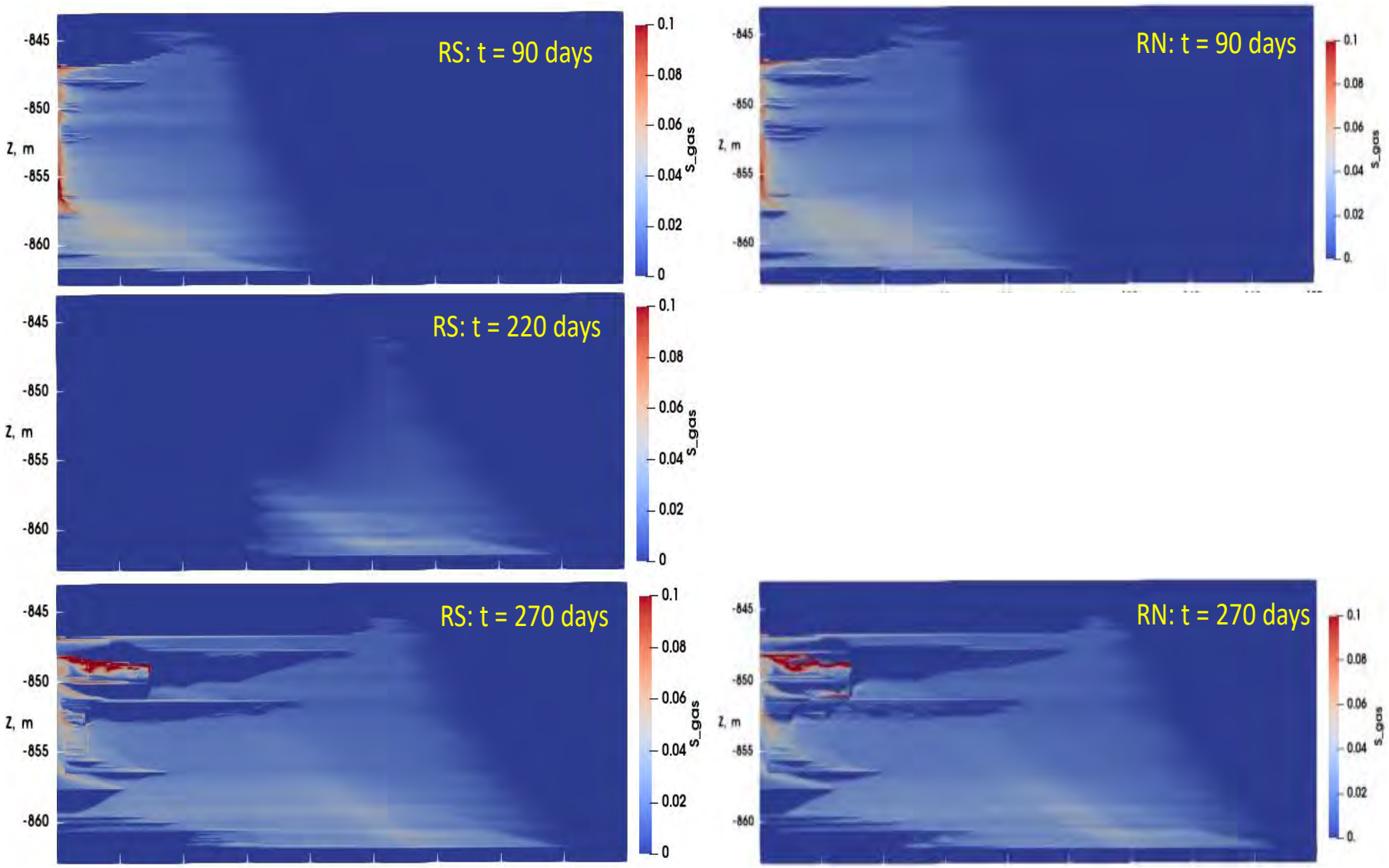

Figure 26: Comparison of the evolution of the S_G-spatial distributions in Unit B over time in Cases RS (left) and RN (right). Note (a) the more extensive RS footprints of S_G at the same times after the two shut-ins, and the partial disappearance of gas at t = 220 days.

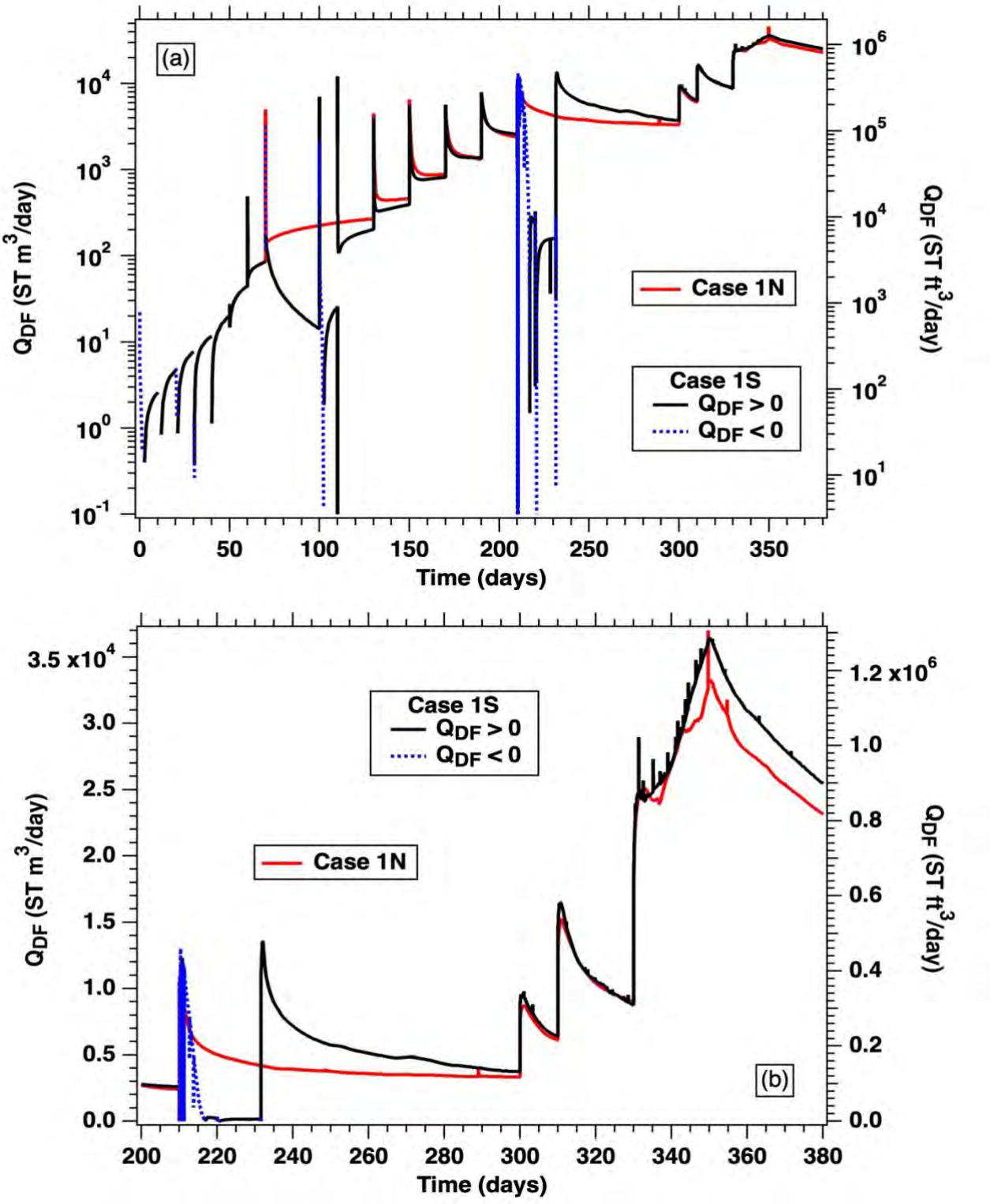

Fig. 27. Evolution of the rate of hydrate dissociation/formation Q_{DF} in Cases 1N and 1S: (a) Semi-log plot covering the duration of the production test and (b) linear plot for detailed Q_{DF} description for $t > 200$ days.

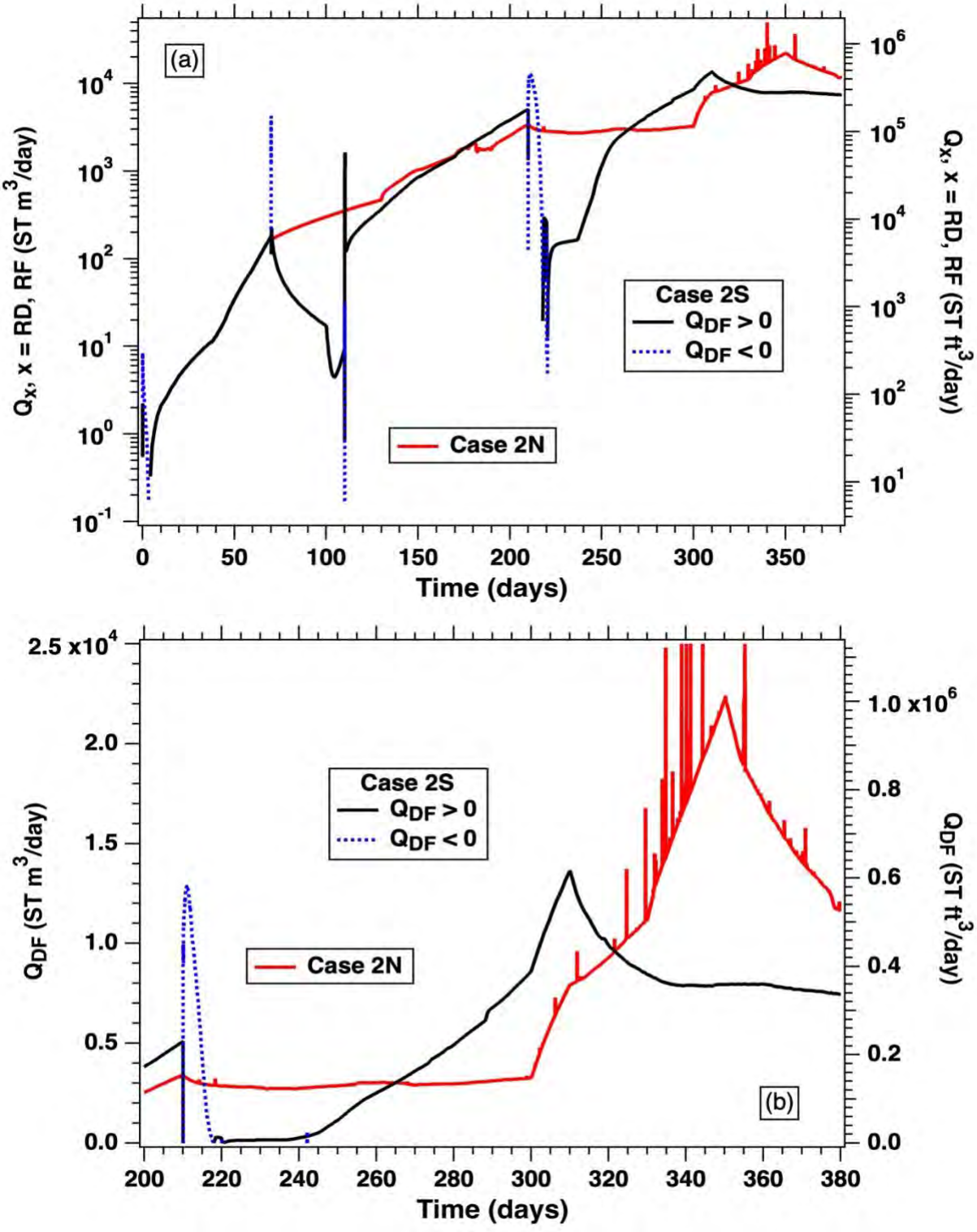

Fig. 28. Evolution of the rate of hydrate dissociation/formation Q_{DF} in Cases 2N and 2S: (a) Semi-log plot covering the duration of the production test and (b) linear plot for detailed Q_{DF} description for $t > 200$ days. The Q_{DF} scales are the same as in Fig. Y-1.

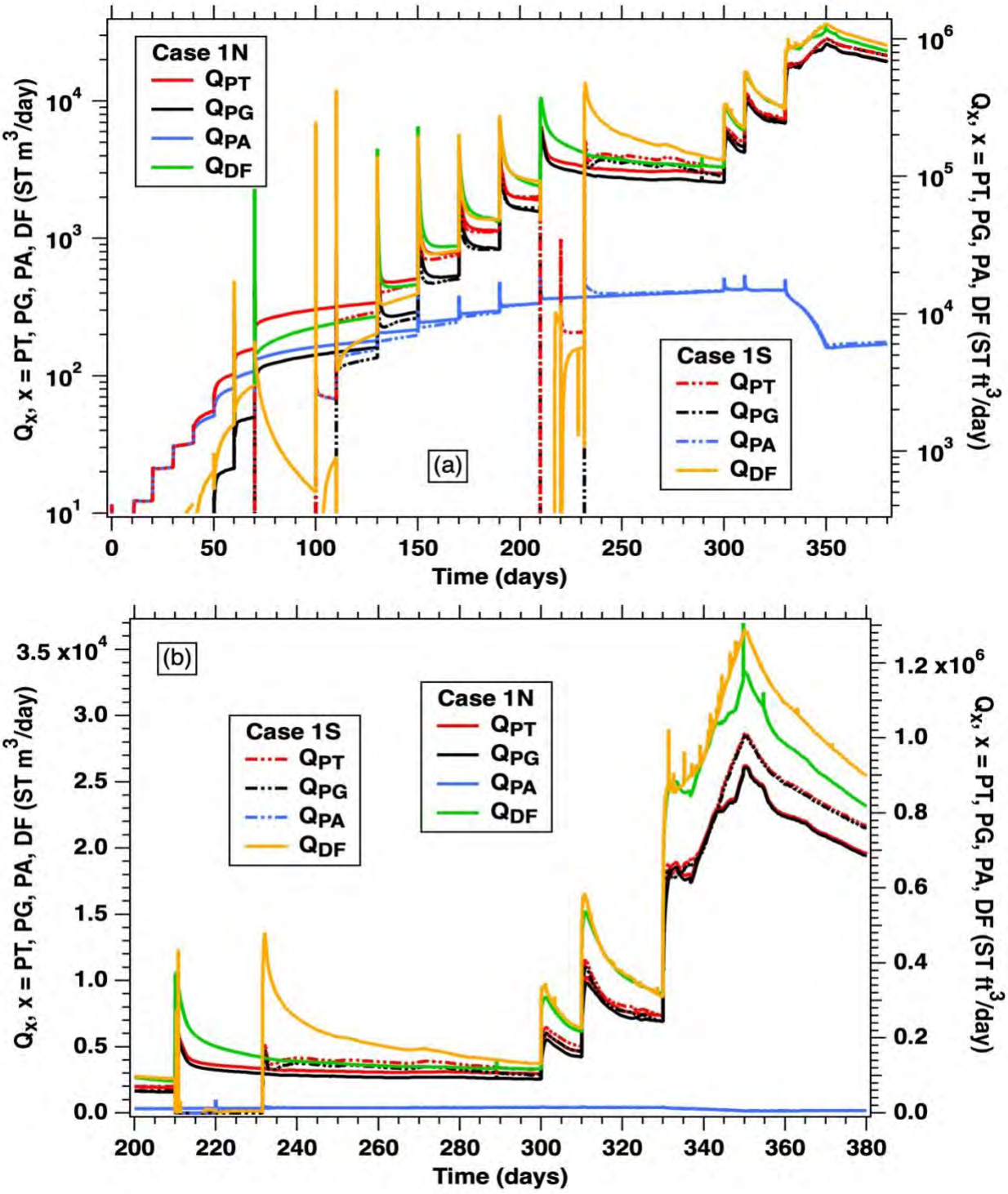

Fig. 29. Plots of the evolution of Q_{PT}, Q_{PG}, Q_{PA} and Q_{DF} in Cases 1N and 1S: (a) Semi-log plot covering the duration of the production test and (b) linear plot for detailed Q_{PT}, Q_{PG} and Q_{PA} description for $t > 200$ days.

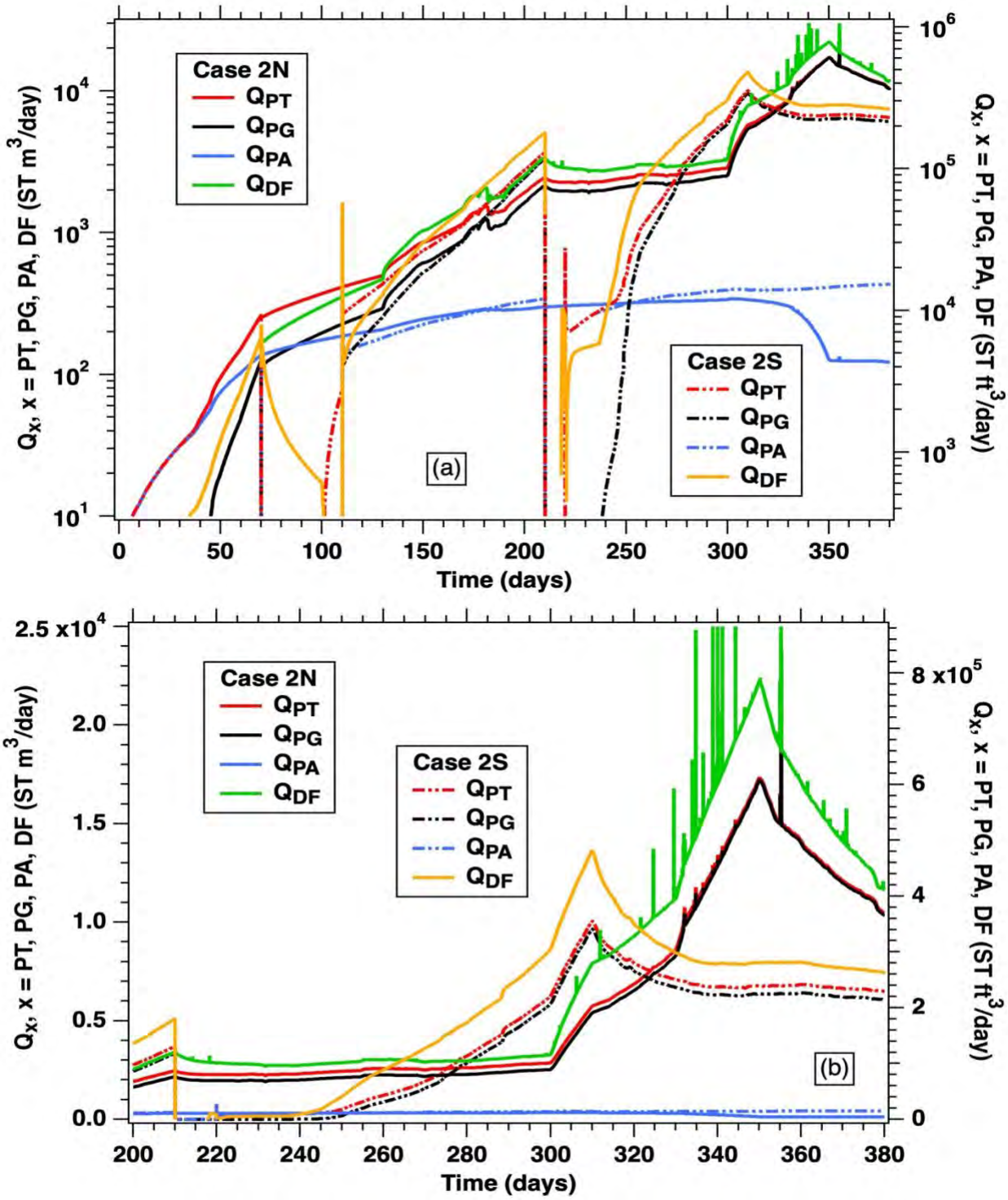

Fig. 30. Plots of the evolution of Q_{PT}, Q_{PG}, Q_{PA} and Q_{DF} in Cases 2N and 2S: (a) Semi-log plot covering the duration of the production test and (b) linear plot for detailed Q_{PT}, Q_{PG} and Q_{PA} description for $t > 200$ days.

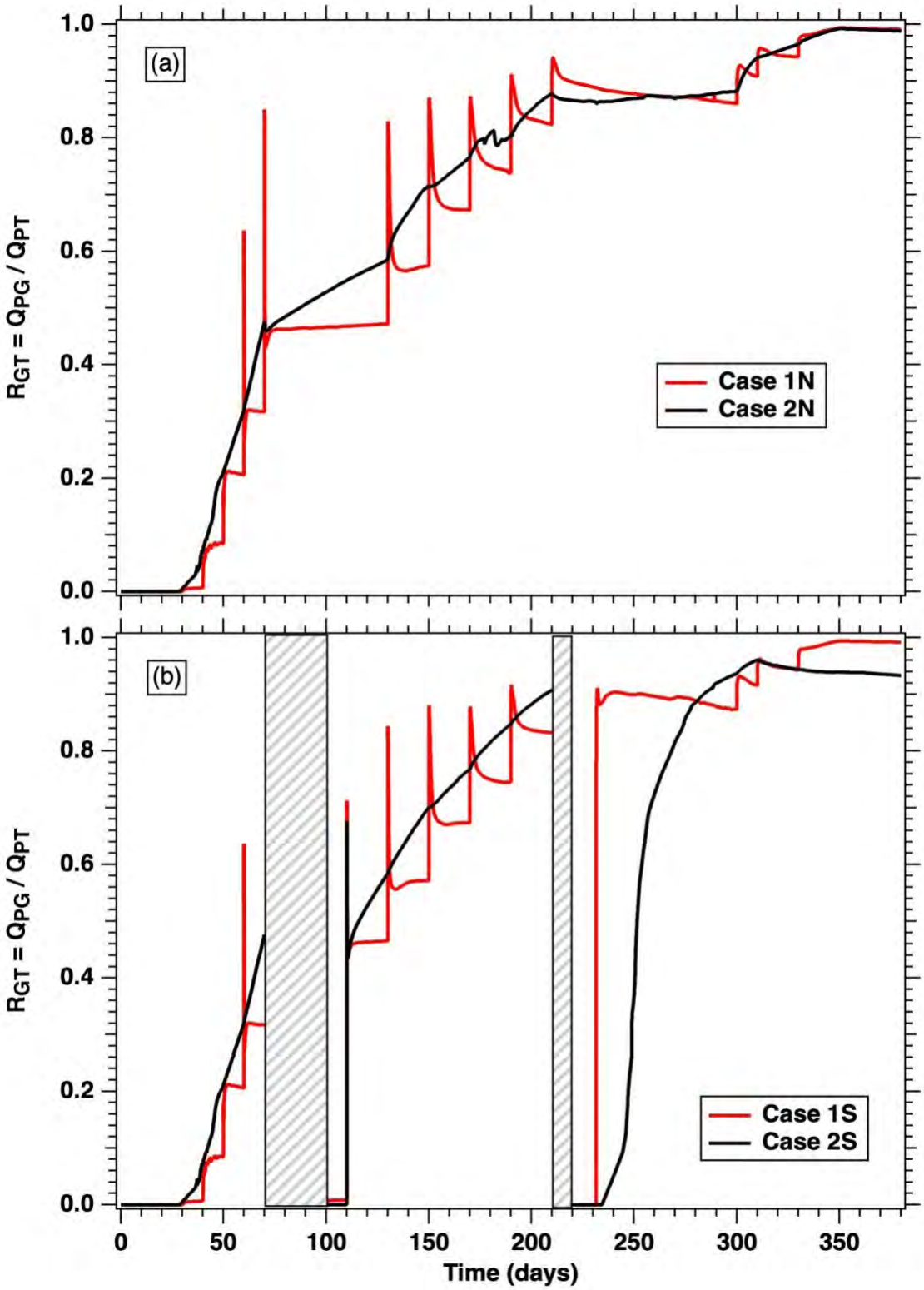

Fig. 31. Evolution of R_{GT} over time in (a) Cases 1N and 2N and (b) Cases 1S and 2S. Note that a R_{GT} >80% is attained late in the production process in all cases.

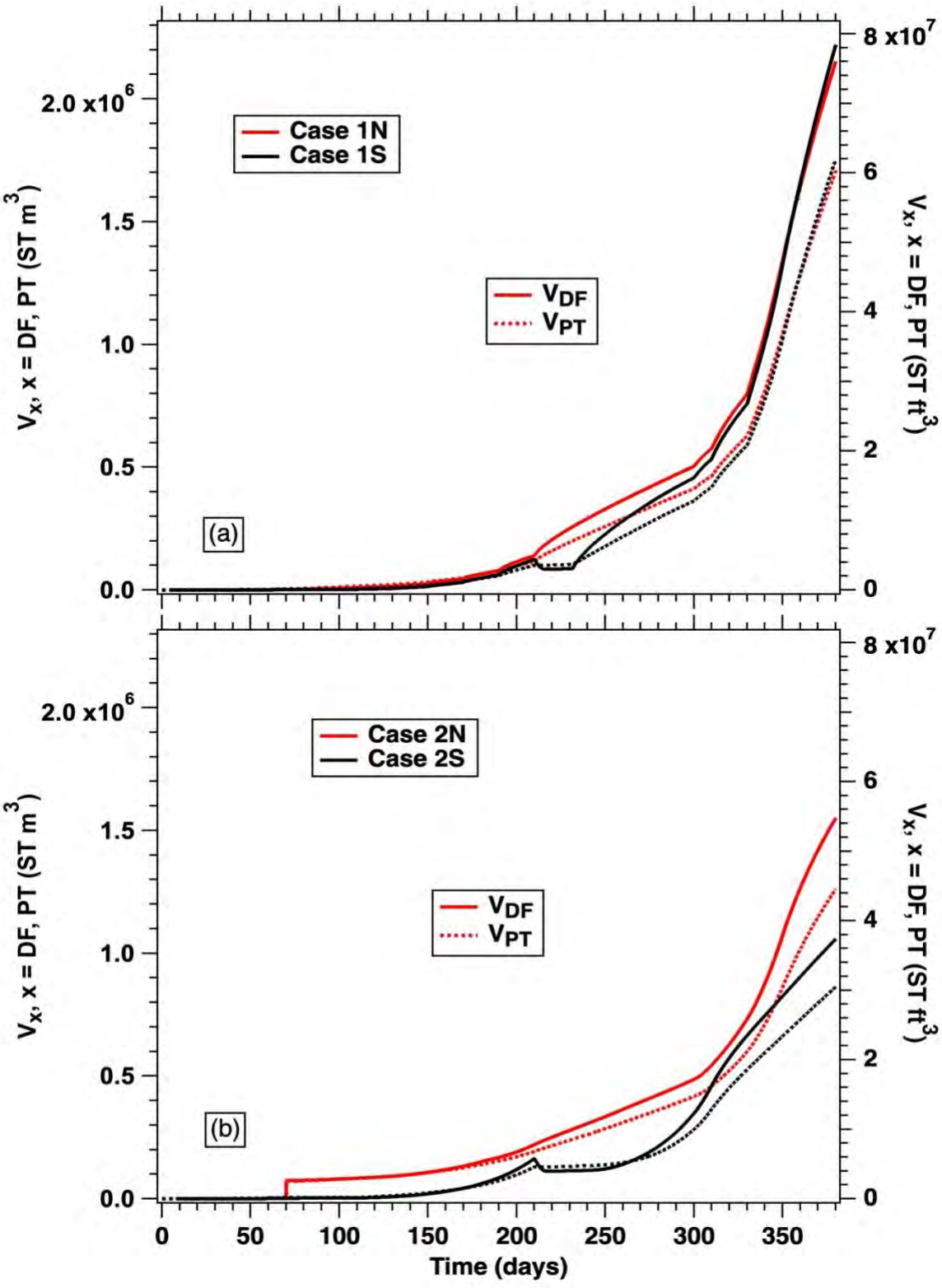

Fig. 32. Effect of shut-ins on V_{DF} and V_{PT} in (a) Cases 1N and 1S and (b) Cases 2N and 2S. The V_{DF} and V_{PT} in both Cases 1S and 2S appear to fully recover late in the production process.

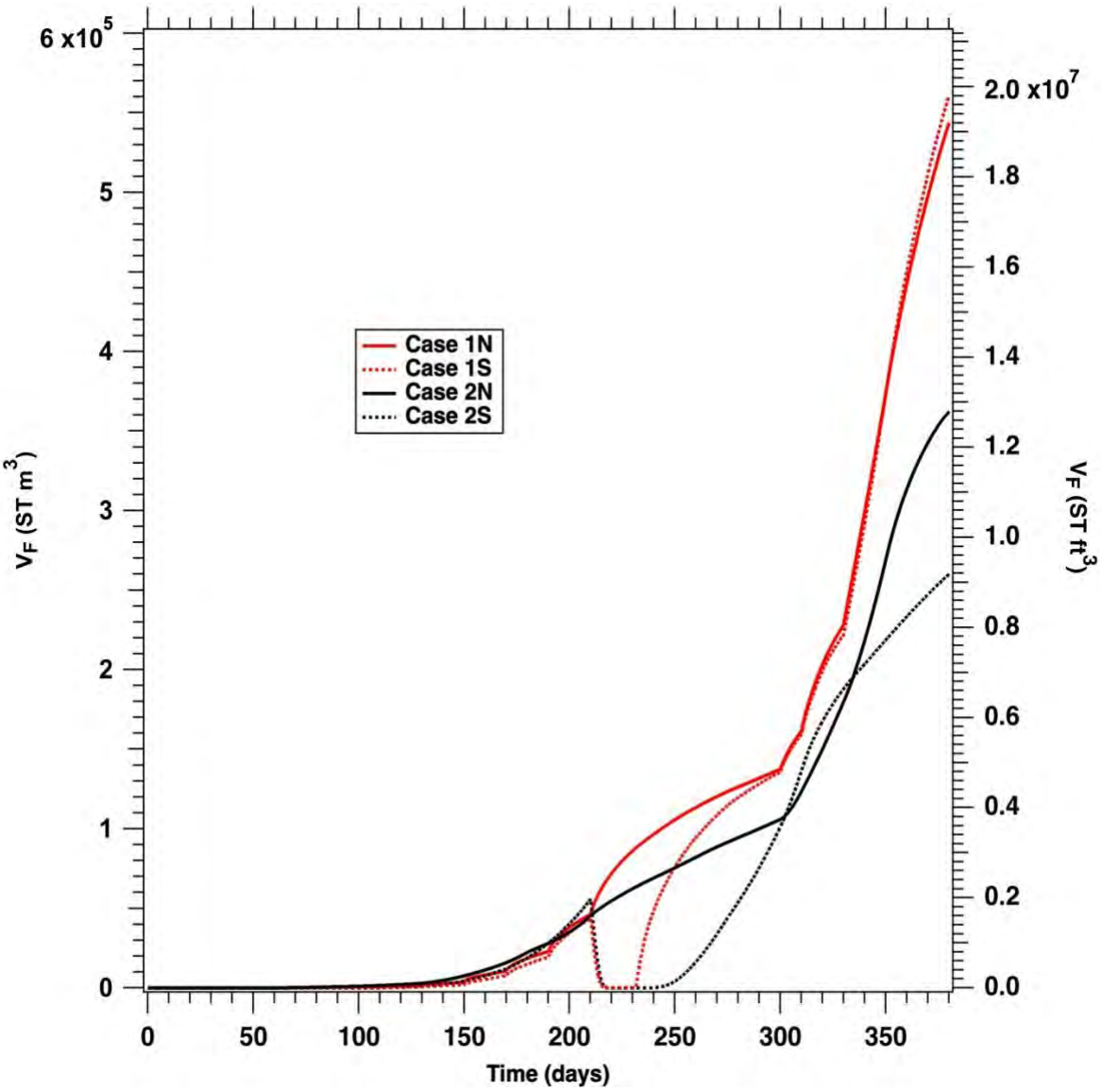

Fig. 33. Effect of shut-ins on the evolution of the volume of free gas V_F in the reservoir V_F in all cases. V_F appear to fully recover in all cases late in the production process.

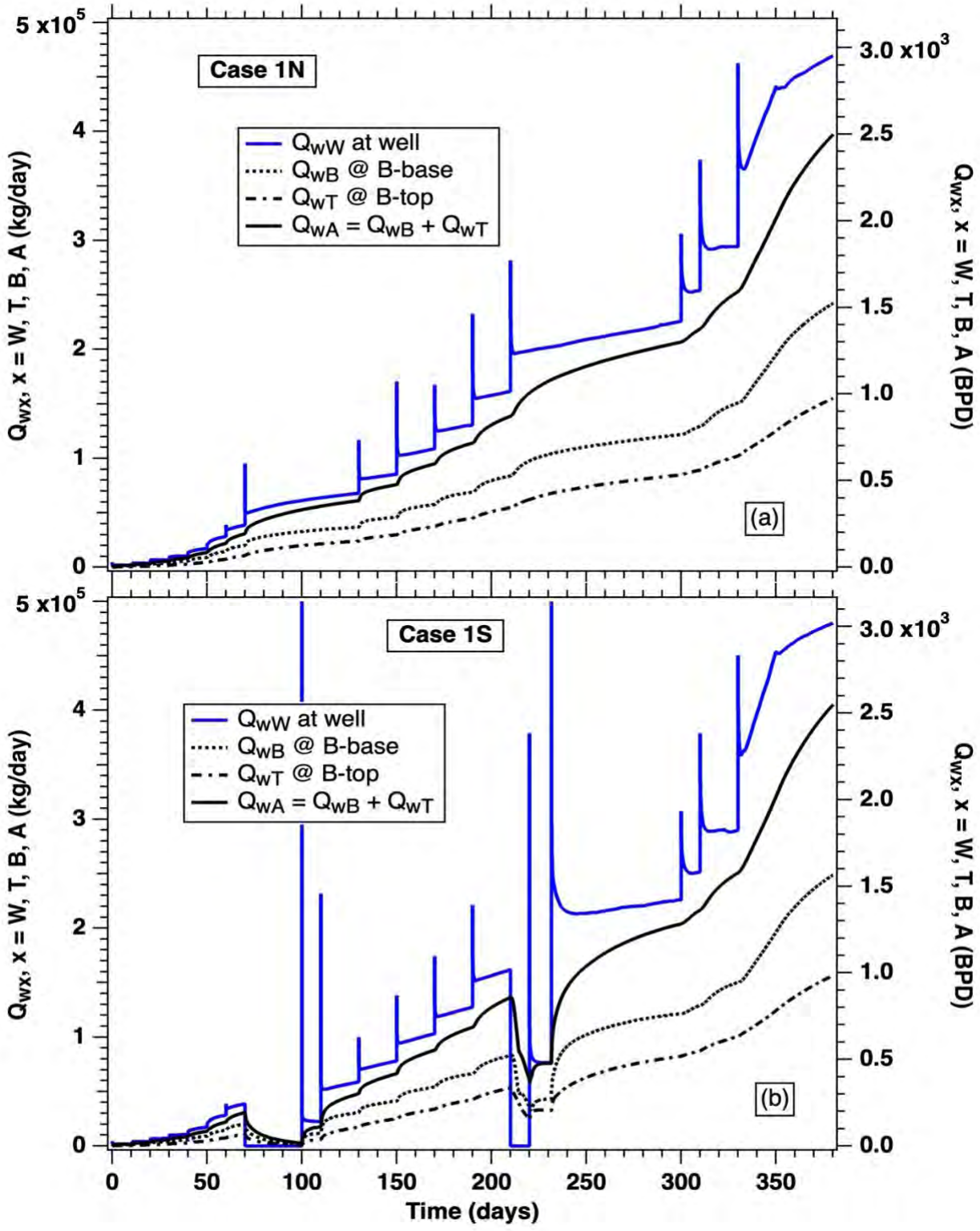

Fig. 34. Evolution of the rate of water production rate at the well Q_{wW} and of its replenishment by water inflows Q_{wT} and Q_{wB} through the top and bottom boundaries, respectively, in (a) Case 1N and (b) Case 1S. Note the proximity of Q_{wA} to Q_{wW} as time advances.

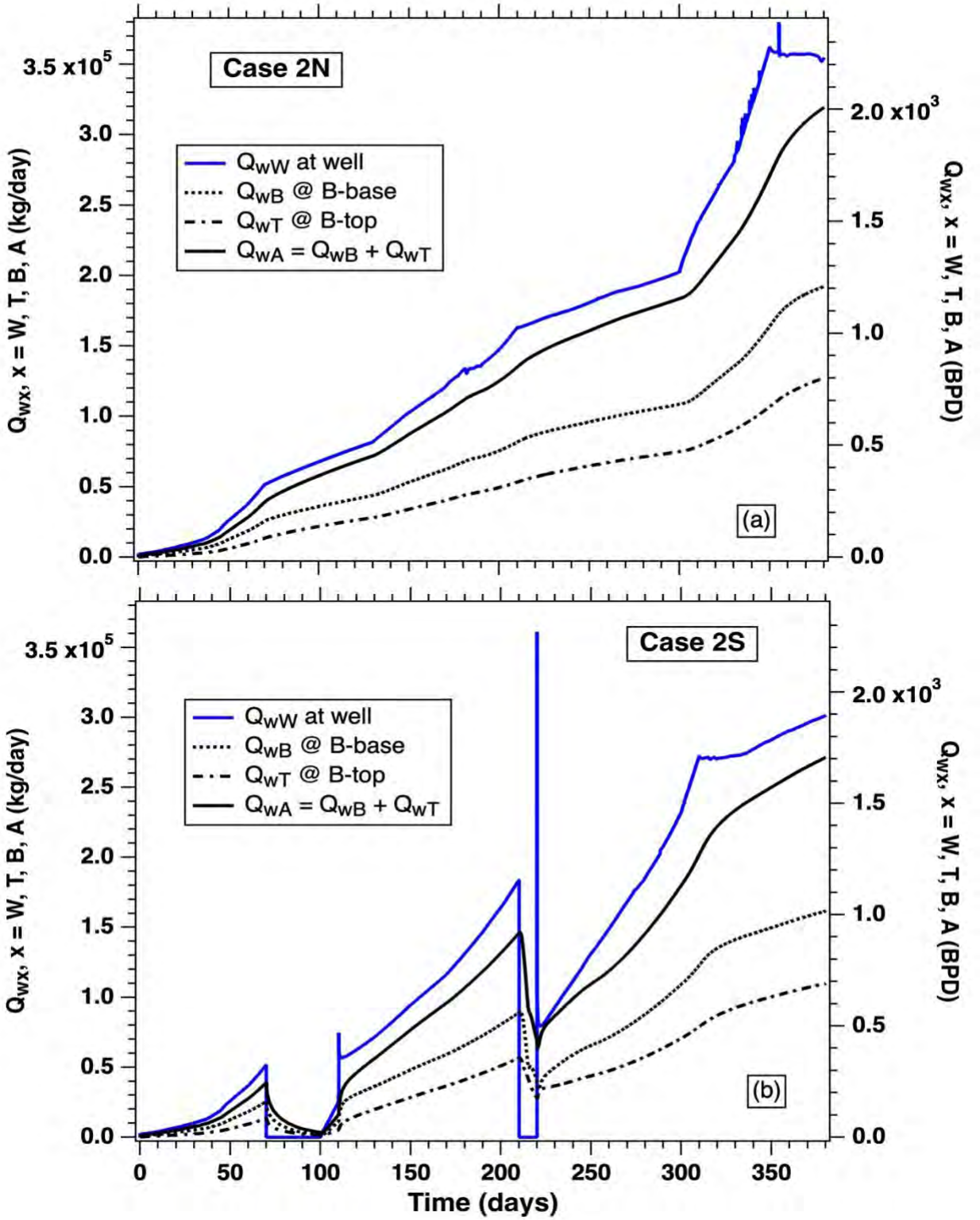

Fig. 35. Evolution of the rate of water production rate at the well Q_{wW} and of its replenishment by water inflows Q_{wT} and Q_{wB} through the top and bottom boundaries, respectively, in (a) Case 2N and (b) Case 2S. Note the proximity of Q_{wA} to Q_{wW} as time advances.

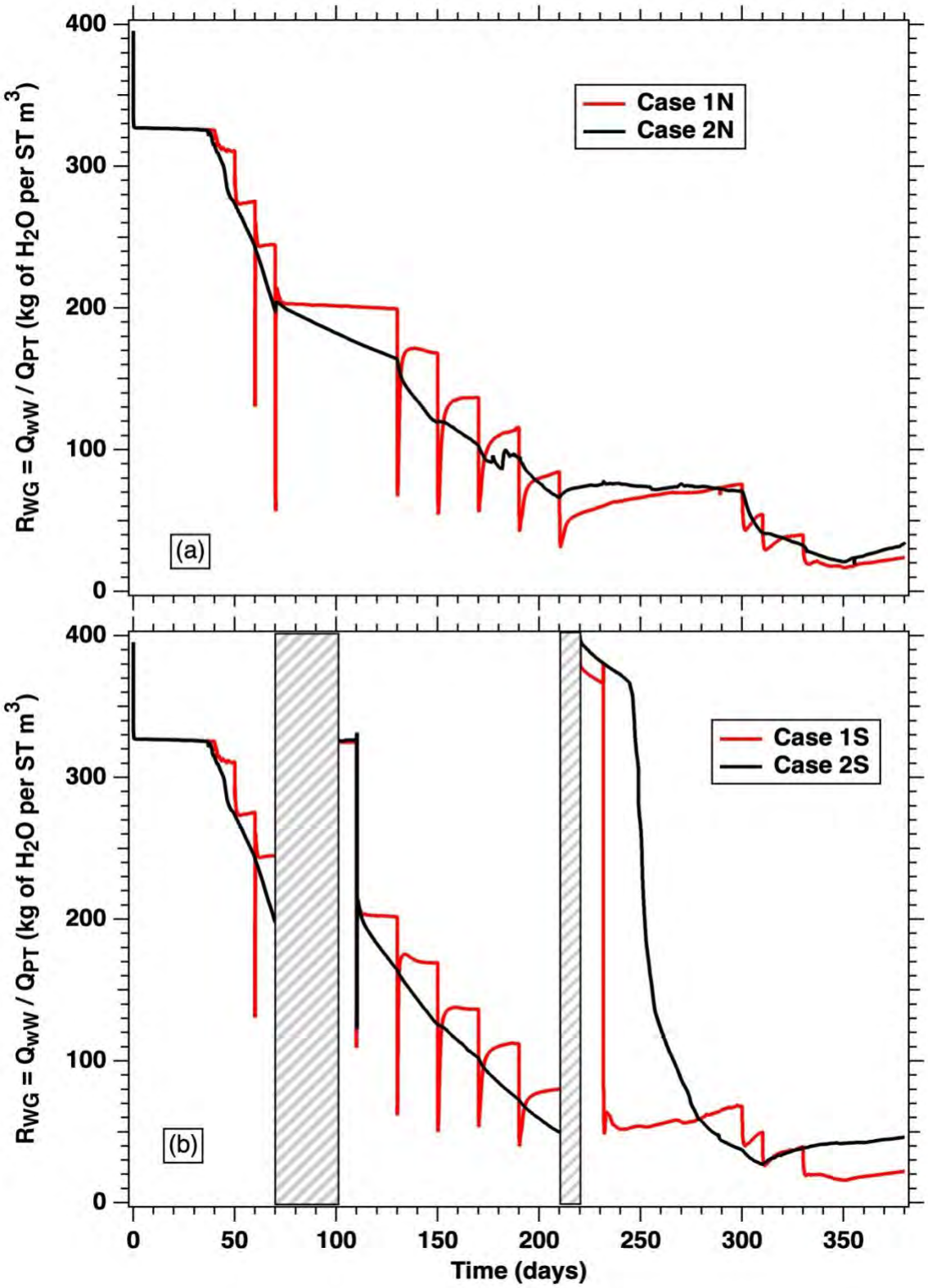

Fig. 36. Evolution of the water-to-gas ratio R_{WG} in (a) Cases 1N and 2N and (b) Cases 1S and 2S. Note the continuous downward trend as time advances.

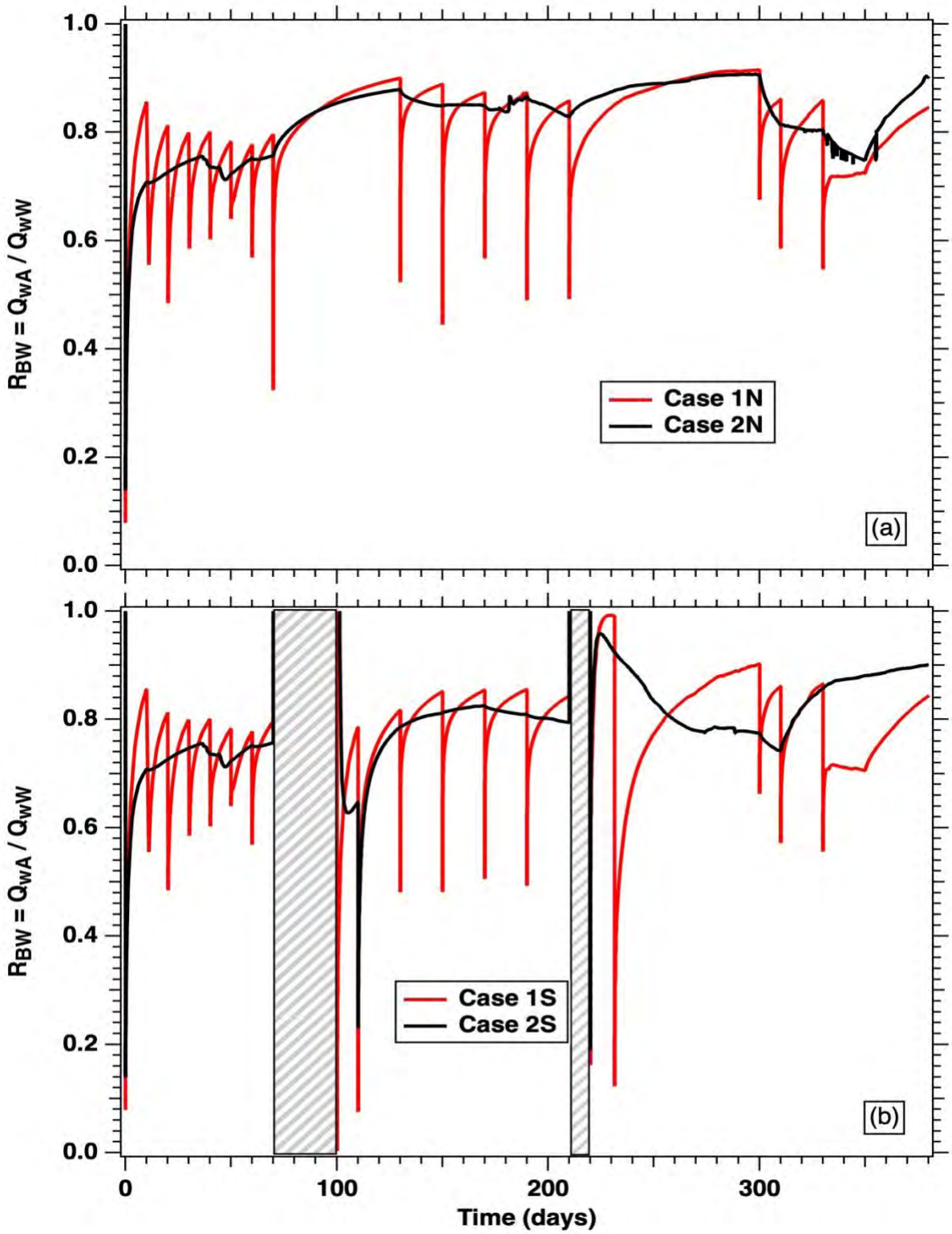

Fig. 37. Evolution of the water replenishment ratio R_{BW} in (a) Cases 1N and 2N and (b) Cases 1S and 2S. Note that after a short time from the onset of production, R_{BW} reaches and often exceeds, the 80% level.

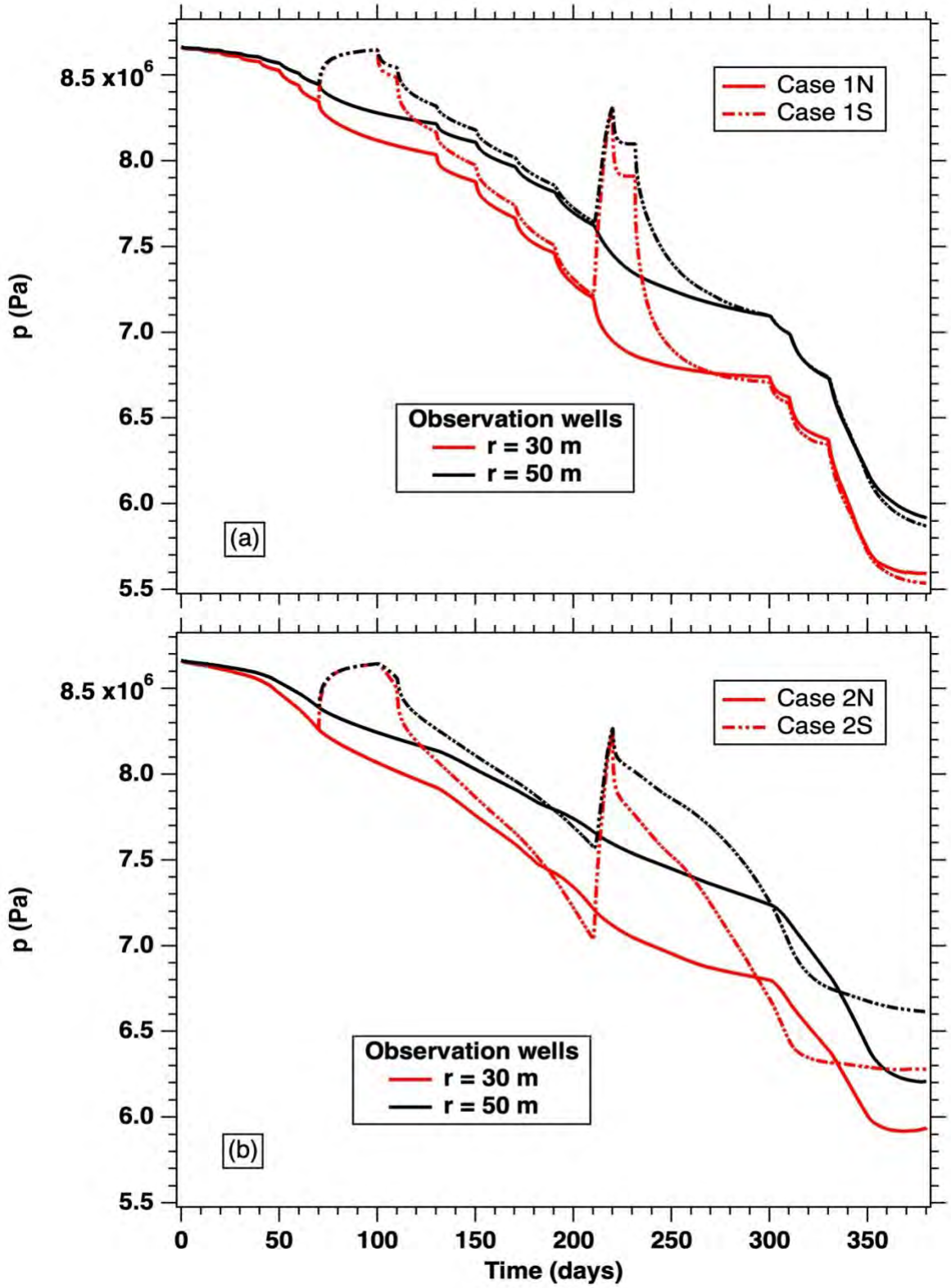

Fig. 38. Evolution of the pressure *P* at the observation wells during the production test in (a) Cases 1N and 1S and (b) Cases 2N and 2S.

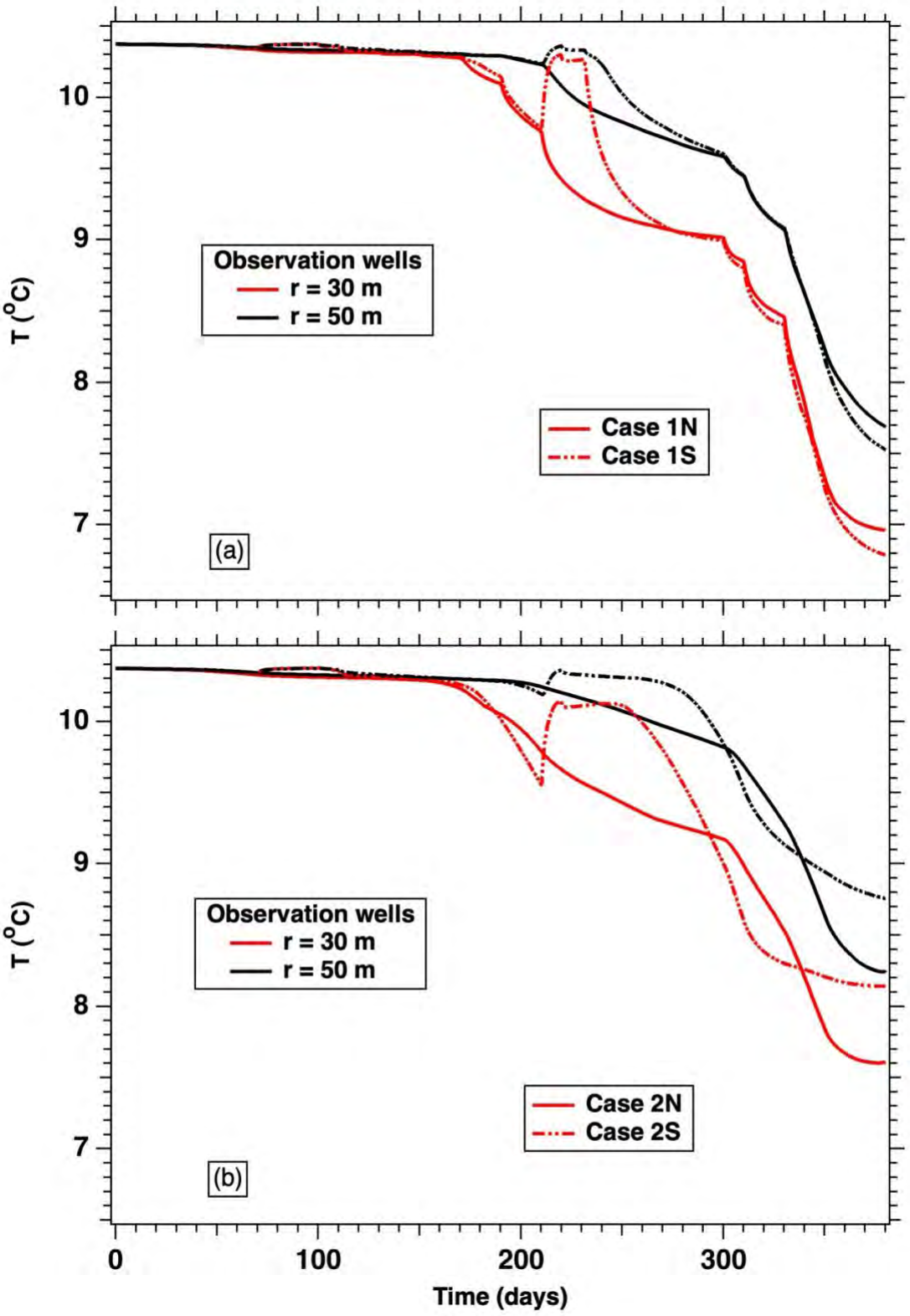

Fig. 39. Evolution of the temperature *T* at the observation wells during the production test in (a) Cases 1N and 1S and (b) Cases 2N and 2S.

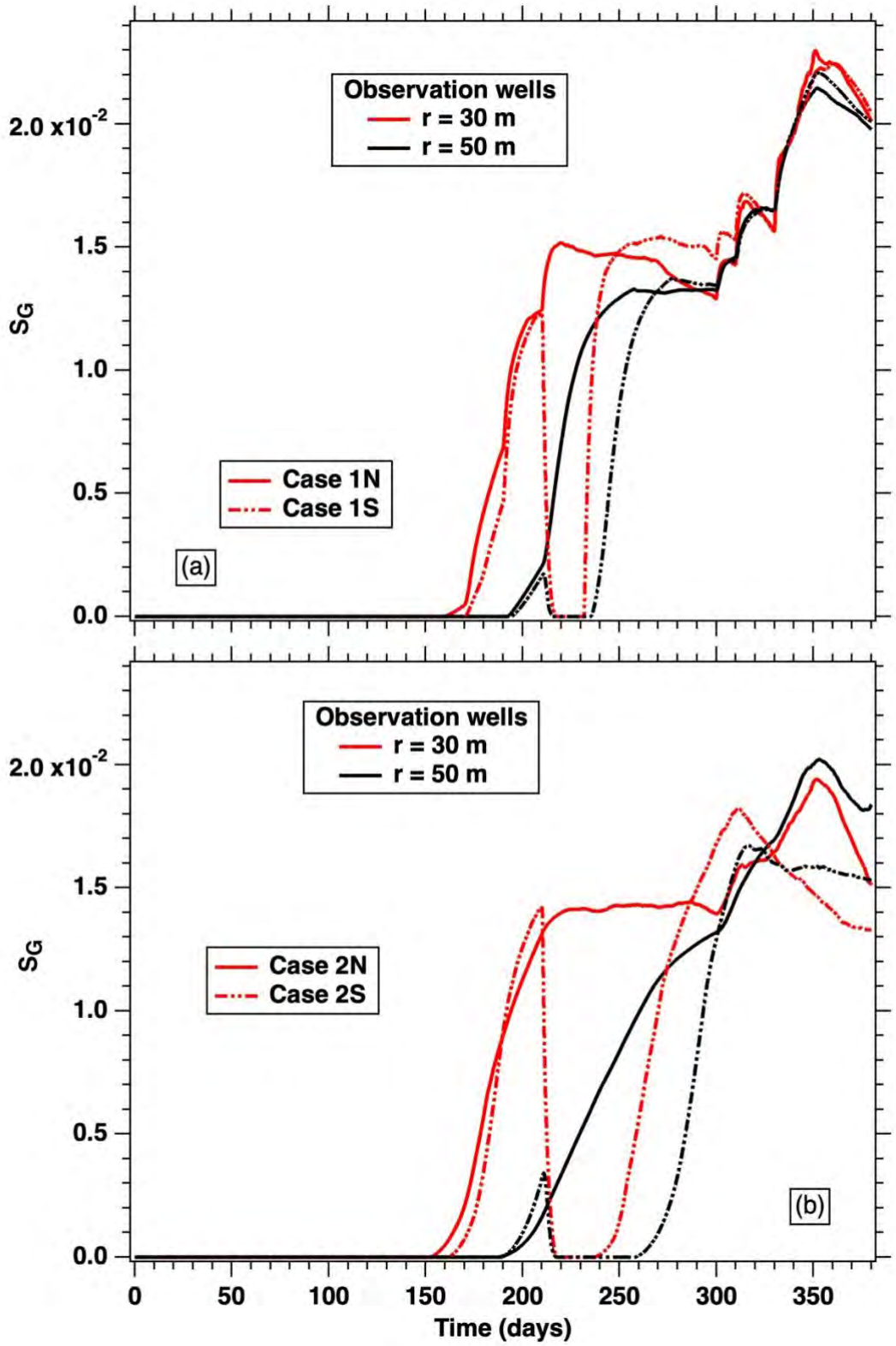

Fig. 40. Evolution of the pore-volume averaged gas hydrate saturation S_G at the observation wells during the production test in (a) Cases 1N and 1S and (b) Cases 2N and 2S. Note the delayed appearance of gas.